



Calhoun: The NPS Institutional Archive

DSpace Repository

Theses and Dissertations | 1. Thesis and Dissertation Collection, all items

1968-09

Large angle scattering of lithium ions by helium atoms.

Bush, Thomas Oliver

Monterey, California. U.S. Naval Postgraduate School

http://hdl.handle.net/10945/12538

This publication is a work of the U.S. Government as defined in Title 17, United States Code, Section 101. Copyright protection is not available for this work in the United States.

Downloaded from NPS Archive: Calhoun



http://www.nps.edu/library

Calhoun is the Naval Postgraduate School's public access digital repository for research materials and institutional publications created by the NPS community. Calhoun is named for Professor of Mathematics Guy K. Calhoun, NPS's first appointed -- and published -- scholarly author.

Dudley Knox Library / Naval Postgraduate School
411 Dyer Road / 1 University Circle
Monterey, California USA 93943

NPS ARCHIVE
1968
BUSH, T.

LARGE ANGLE SCATTERING OF LITHIUM IONS BY HELIUM ATOMS

by

Thomas Oliver Bush

LIBRARY
NAVAL POSTGRADUATE SCHOOL
MONTEREY, CALIF. 93940

UNITED STATES
NAVAL POSTGRADUATE SCHOOL

THESIS

LARGE ANGLE SCATTERING OF

LITHIUM IONS BY HELIUM ATOMS

by

Thomas Oliver Bush

September 1968

[redacted]

This document has been approved for public release and sale; its distribution is unlimited.

[redacted]

LARGE ANGLE SCATTERING OF LITHIUM IONS BY HELIUM ATOMS

by

Thomas Oliver Bush
Lieutenant, United States Navy
B.S., University of Oklahoma, 1960

Submitted in partial fulfillment of the
requirements for the degree of

DOCTOR OF PHILOSOPHY

from the

NAVAL POSTGRADUATE SCHOOL
September 1968

68
SH, T.

ABSTRACT

An experiment using the focusing properties of a nonuniform axially symmetric magnetic field to study large angle ($\theta > 32^{o}$) scattering of ions from atoms and molecules is described. The scattering cell is placed on the magnetic field axis and all ions in the momentum interval $|\Delta p|$ at $|p|$ scattered into a conical shell $\Delta\theta$ at θ are counted by a detector placed further down the axis. The solid angle is increased by a factor of several hundred over conventional scattering techniques of comparable angular resolution. The magnetic vector potential and the trajectory equation for a charged particle in the field are derived. The computer program which solves the trajectory equation is given along with a detailed description of the apparatus. Our measurements of the absolute differential scattering cross sections for Li^{+} on He from 36^{o} to 41.7^{o} at 200 eV and 300 eV and for He^{+} on He from 40^{o} to 54^{o} at 300 eV and 400 eV demonstrate the feasibility of the technique. Using the measured cross sections for Li^{+} on He and the computational method of Firsov we have calculated the interatomic potential function for nuclear separations of 0.15Å to 1.1Å.

LIBRARY
NAVAL POSTGRADUATE SCHOOL
MONTEREY, CALIF. 93940

TABLE OF CONTENTS

		Page
List of Tables		5
List of Illustrations		7
Acknowledgements		10
I.	Introduction	11
II.	Kinematics of Charged Particles in a Nonuniform Axially Symmetric Magnetic Field	15
	1. Motion of a Charged Particle in a Uniform Field	15
	2. Analogue Measurement of Orbits	20
	3. Magnetic Vector Potential	24
	4. Orbit Equation in Nonuniform Field	28
	5. Angular and Energy Resolution	31
	6. Solid Angle	36
III.	Experimental Apparatus	39
	1. Vacuum System	39
	2. Ion Sources	41
	Lithium Ion Source	41
	Electron Impact Ion Source	44
	3. Mass Analyser	47
	4. Focusing Magnet and Field Measurements	48
	5. Scattering Cell	52
	6. Scattered Ion Detector	59
	7. System Alignment	65
IV.	Experimental Results	67
	1. Preliminary Tests	67
	2. He^+ on He Data	71
	3. Li^+ on He Data	74
	4. Experimental Error	81
V.	Calculation of the Interatomic Potential for the Li^+-He System	83
	1. Introduction	83
	2. Theory	83
	3. Procedure	86
	4. Results	89
VI.	Conclusions	91
Appendices		
I.	The Effect of Target Size and Ion Beam Energy Spread on the Solid Angle	94
II.	Calculation of the Intercept Spread	100
III.	Calculation of the Target Thickness	106
IV.	Listing of Computer Programs	112
V.	Ion Beam Optics	132
VI.	Electron Impact Ion Source	140

LIST OF TABLES

Table Number	Title	Page
I	Focusing Magnet Data	50
II	Solid Angle Corrections for ^{6}Li on N_2 at 100 eV	98

LIST OF ILLUSTRATIONS

Number	Title	Page
1.	Schematic of Experimental Apparatus	13
2.	Orbit of a Charged Particle in a Uniform Magnetic Field	17
3.	Schematic of Wire Orbit Method	23
4.	Comparison of Wire Orbit and Computer Trajectories for H_2^+	25
5.	Numerically Computed Ion Trajectories for $^6Li^+$ on Ne at 100 eV	32
6.	Angular Spread Allowed by the Detector Apertures	33
7.	Solid Angle vs Scattering Angle for Elastic Scattering of $^6Li^+$ on Ne at 100 eV Incident Ion Energy	38
8.	Experimental Apparatus	40
9.	Schematic of Lithium Ion Source	42
10.	Lithium Ion Source Emitter Detail	43
11.	Lithium Ion Source Emission Curve	45
12.	Electron Impact Ion Source	46
13.	Schematic of Mass Spectrometer	49
14.	Arrangement for Measuring the Magnetic Field	51
15.	Axial Magnetic Field Strength vs Distance	53
16.	Axial Magnetic Field Strength Measured at Various r and Ø values	54
17.	Scattering Cell	55
18.	Schematic of Scattering Cell and Beam Collector	56
19.	Operational Schematic of the Bendix Model 306 Magnetic Electron Multiplier	60
20.	Log_{10} Gain vs Axial Magnetic Field Strength	63
21.	Detector Current vs Target Pressure for $^6Li^+$ on He at 40.42°	69

22.	Detector Current vs Ion Current for $^{6}Li^{+}$ on He at 40.96°	69
23.	Detector Current vs Target Length for $^{6}Li^{+}$ on He at 39.1°	70
24.	$d\sigma(\theta)_{lab}$ vs θ_{lab} for He^{+} on He, E_{lab}= 300 eV	72
25.	$d\sigma(\theta)_{lab}$ vs θ_{lab} for He^{+} on He, E_{lab}= 400 eV	73
26.	$d\sigma(\theta)_{lab}$ vs θ_{lab} for $^{6}Li^{+}$ on He, E_{lab}= 200 eV	75
27.	$d\sigma(\theta)_{lab}$ vs θ_{lab} for $^{6}Li^{+}$ on He, E_{lab}= 300 eV	76
28.	$d\sigma(\theta)_{cm}$ vs θ_{cm} for $^{6}Li^{+}$ on He, E_{cm}= 80.0 eV	78
29.	$d\sigma(\theta)_{cm}$ vs θ_{cm} for $^{6}Li^{+}$ on He, E_{cm}= 120.0 eV	79
30.	Elastic Differential Scattering Cross Section for $^{6}Li^{+}$ on He	80
31.	$\sigma(\theta)\sin\theta$ vs θ for $^{6}Li^{+}$ on He, E_{cm}= 80.0 eV	87
32.	$\theta(b)$ vs b for $^{6}Li^{+}$ on He, E_{cm}= 80.0 eV	88
33.	Interatomic Potential for Li^{+}-He as a Function of Internuclear Separation	90
A2-1	Detector Aperture Geometry	101
A2-2	Intercept Spread vs Intercept Angle	105
A3-1	Target Thickness Correction vs Scattering Angle (Lab)	110
A3-2	Target Thickness vs Scattering Angle for an 0.4 cm Cell Opening	111
A5-1	Beam Potential vs Beam Current	136
A5-2	Einzel Lens Equipotential Lines	137
A5-3	Einzel Lens Focal Length Relation	139
A6-1	Schematic of Electron Impact Source	141
A6-2	Electron Impact Ion Source Wiring Diagram	143
A6-3	Electron Impact Source Characteristics	145

A6-4 Ion Output vs Source Pressure for H_2 Source Gas 146

A6-5 Ion Output vs Source Pressure for N_2 Source Gas 147

ACKNOWLEDGEMENTS

The author is deeply indebted to his thesis advisor, Professor Otto Heinz, for the nudging along toward completion he constantly supplied. I am also grateful for the advice and help of Dr. Charles J. Cook of the Stanford Research Institute, Palo Alto, California, who along with Professor Heinz originated this particular approach to measuring cross sections. I especially want to thank Mr. Thomas Maris of the Naval Postgraduate School Physics Department technical staff who constructed most of the actual apparatus. I also gratefully acknowledge the assistance of Dr. W. Aberth of SRI for his help on some of the experimental problems encountered, of Dr. Raymond P. Marchi for his help with the potential calculation, and of Captain N.R.A. Smyth, CF, for writing and fighting the computer program.

Finally, I am grateful for my wife, Mary Jo, whose patience made it easier and whose love made it worthwhile.

CHAPTER I

INTRODUCTION

In recent years the techniques for measuring differential scattering cross sections for various atomic and molecular processes have been improved to the point where very precise measurements can be made in an almost routine manner. In the conventional approach a target of N_t particles is confined within a surrounding vacuum. A well collimated beam of nearly monoenergetic ions of current I_i is projected into the target. A detector, subtending a solid angle $d\Omega(\theta) = \text{Sin}\ \theta\ d\theta\ d\phi$ at the interaction region, is placed at an angle θ to the incident ion beam and the number of particles entering the detector, N_s, is measured. The scattered particles are usually detected as a current where $I_s = N_s d\Omega(\theta)$. From these measured quantities, the differential scattering cross section in the laboratory coordinate system can be calculated as

$$d\sigma(\theta) = I_s/I_i N_t d\Omega(\theta).$$

However, in order to obtain reasonably good angular resolution, the solid angle includes only about 1^o of the available 360^o of azimuthal angle ϕ into which ions scatter. This restriction results in fairly small solid angles of about 10^{-4} steradians, which sets a lower limit of around 10^{-20} cm^2 on observable laboratory differential scattering cross sections. By modifying the techniques of thin magnetic lens β-ray spectroscopy, we have constructed an experimental apparatus which collects essentially all ions scattered into a 360^o cone $d\theta$ wide at θ. The solid angle in this apparatus is about 300 times larger than that of other methods,

allowing us to observe differential scattering at laboratory angles greater than 32 degrees and cross sections substantially smaller than any previously measured.

The apparatus, shown schematically in Figure 1, was developed to make use of the focusing properties of an axially symmetric nonuniform magnetic field. The scattering cell exit slit is open 290° of the aximuthal angle, allowing ions of a given $\vec{p}$ and θ but scattered at most any azimuthal angle to be focused at the detector by the magnetic field. Both the magnet current and the distance between the scattering cell and detector are variable. Various combinations of the magnet current and the detector distance make a wide range of reactions observable with the apparatus. The details of the apparatus are discussed in Chapter III.

The differential equation for the trajectory of a charged particle in a nonuniform axially symmetric magnetic field and the magnetic vector potential for this field are developed in Chapter II. The trajectory equation is numerically integrated to give the values of the magnetic field and detector position necessary to observe charged particles scattered at various angles and energies. The solid angle is calculated from the computed trajectories and is a function of the angle of scatter, the energy of the scattered ion, the magnetic field, and the detector distance. This calculation is discussed in detail in Chapter II.

The elastic differential scattering cross sections for He^+ on He at 300 eV from 40° to 52°, and for He^+ on He at 400 eV from 42° to 53° were measured using this method and the results are in

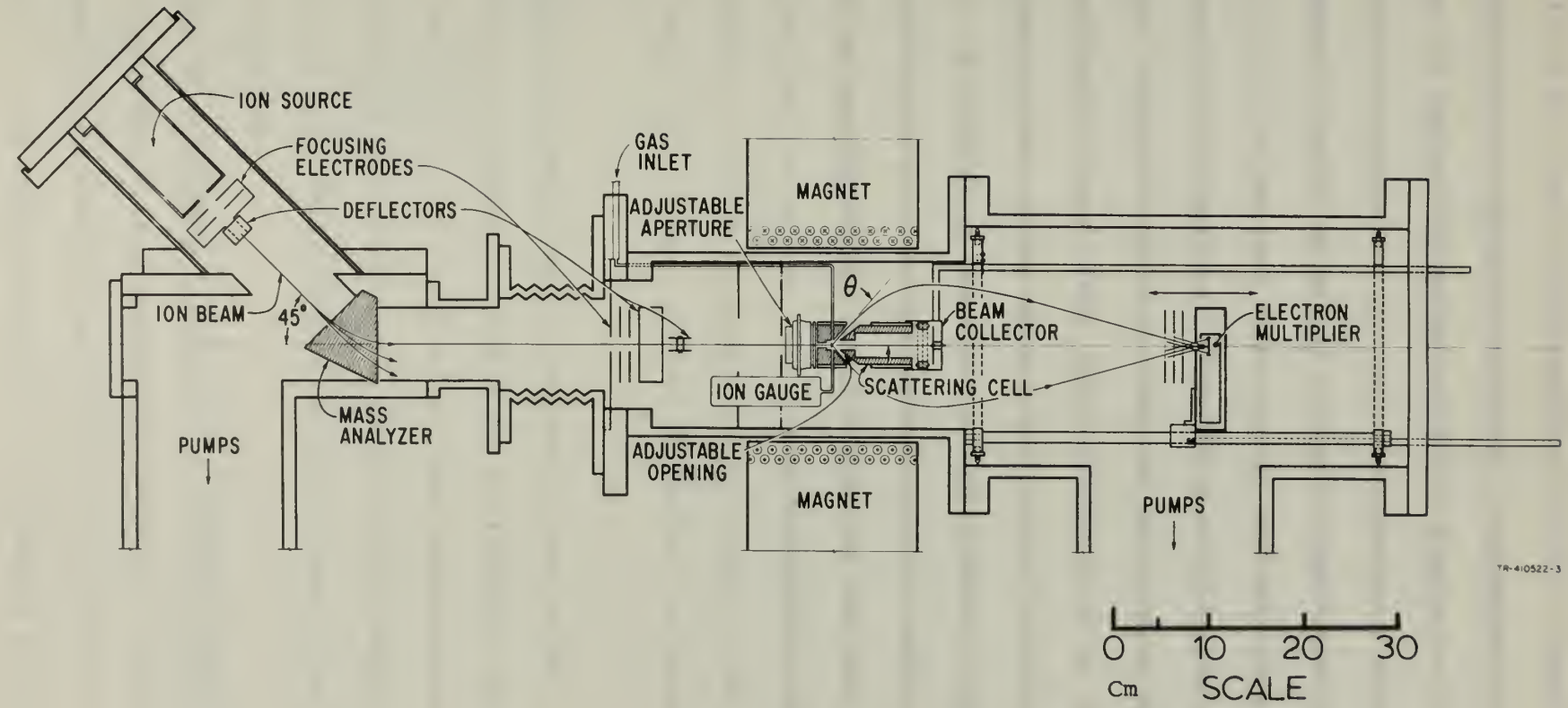


Figure 1. Schematic of Experimental Apparatus

essential agreement with measurements of Lorents and Aberth[1] who used a standard technique. The elastic differential scattering cross sections measured for $^{6}Li^{+}$ on He at 200 eV and 300 eV from 34^{o} to 41.7^{o} also compared favorably to extrapolated values of cross sections measured at smaller angles by other investigators[2]. These experimental results are given in Chapter IV.

Finally, the elastic differential scattering cross section for $^{6}Li^{+}$ on He measured by our method, along with data taken at smaller angles by other workers, was used to calculate the ion-atom potential function for this system using a method developed by Firsov[3]. This calculation is discussed in Chapter V.

Based on these results we conclude that the feasibility of the technique has been established and its usefulness in obtaining new data has been demonstrated.

CHAPTER II

KINEMATICS OF CHARGED PARTICLES IN A NONUNIFORM AXIALLY SYMMETRIC MAGNETIC FIELD

In this chapter the equation of motion of a charged particle in a uniform magnetic field is solved to show the explicit relation among the following three variables: the vector momentum of the ion, $\vec{p}$, the magnetic field, $\vec{B}$, and Z_o, the distance from the origin at which a detector must be placed to observe the ion. The expression for the solid angle is obtained in closed form and its dependence on the various parameters is shown.

The orbit equation for the axially symmetric nonuniform magnetic field is then derived along with the expression for the magnetic vector potential, which is part of the orbit equation. Expressions for the angular and energy resolution are found and these results are used to find the solid angle. The dependence of the solid angle on the various parameters is shown and discussed.

Finally, an experimental method of simulating a particle trajectory in a magnetic field using a flexible, current carrying wire is described. The results of these measurements were used for preliminary design considerations and are compared to the orbits which were obtained by numerical integration of the trajectory equation.

1. MOTION OF A CHARGED PARTICLE IN A UNIFORM MAGNETIC FIELD

A longitudinal type homogeneous magnetic field spectrometer has commonly been used in the analysis of β spectra in nuclear physics[4,5]. The theory of motion of a charged particle in a

uniform magnetic field was originally published by Busch[6] in 1926, upon which the technique was based.

The trajectory of a charged particle in a uniform field is a helix, where the particle, after one complete revolution of period T, will focus again on the axis from which it originated. As seen in Figure 2, the distance Z_o, at which the ion returns to the Z axis, depends on the momentum, $\vec{p}$, the angle, θ, and the magnetic field, $\vec{B}$. The relationship between these quantities can be derived as follows:

Let $\vec{p}$ = vector momentum of an ion at the origin of the coordinate system at t = 0

and q = charge of ion.

The magnetic field is described by

$$\vec{B} = B_r \hat{r} + B_\phi \hat{\phi} + B_z \hat{z}$$

where $B_r = B_\phi = 0$, B_z = constant.

The boundary conditions seen from Figure 2 are;

at t = 0: r = 0, z = 0, $p_z = p \cos \theta$, $p_r = p \sin \theta$,

and at t = T: r = 0, $z = Z_o$.

In order to get the relation $Z_o = f(p,\theta,B)$ we must integrate the force equation, $\vec{F} = q \vec{v} \times \vec{B}$, and apply the boundary conditions at t = 0, and t = T. Thus

$$\vec{F} = q \vec{v} \times \vec{B},$$

and in component form

$$F_r = m \left[\frac{d^2 r}{dt^2} - r \left(\frac{d\phi}{dt} \right)^2 \right] = q \, v_\phi B_z = q \, r \left(\frac{d\phi}{dt} \right) B_z \quad (1)$$

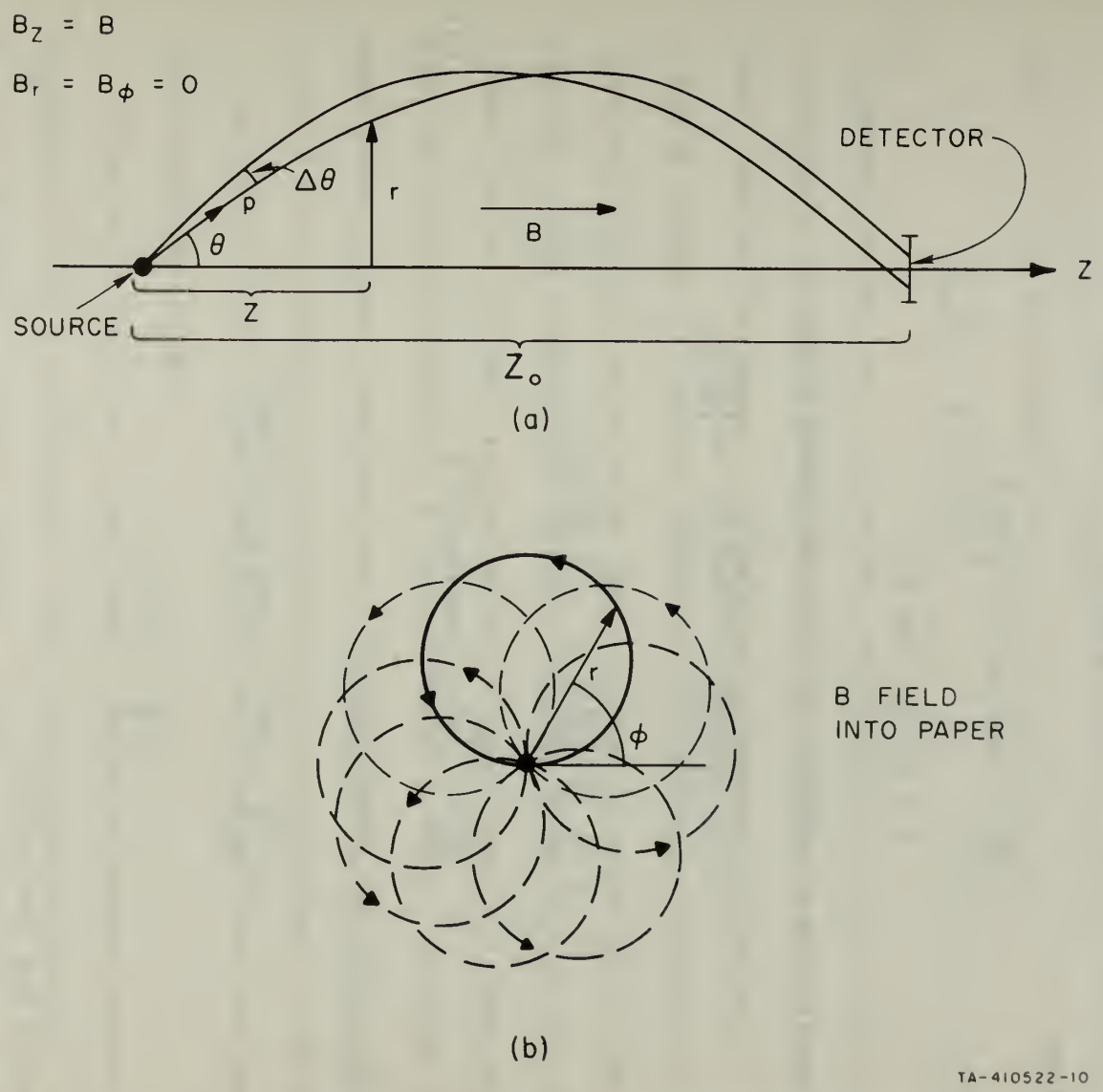


Figure 2. Orbit of a Charged Particle in a Uniform Magnetic Field

$$F_{\phi} = m\left[2\left(\frac{dr}{dt}\right)\left(\frac{d\phi}{dt}\right) + r\left(\frac{d^2\phi}{dt^2}\right)\right] = -q\, v_r B_z = -q\left(\frac{dr}{dt}\right) B_z \qquad (2)$$

$$F_z = m\,\frac{d^2z}{dt^2} = 0. \qquad (3)$$

Integrating (3) and applying the boundary conditions at t = 0 gives

$$m\,\frac{dz}{dt} = \text{constant} = p\cos\theta$$

$$z = \left[(p/m)\cos\theta\right] t. \qquad (4)$$

From (2), upon multiplying by r and integrating

$$m\left[2r\left(\frac{dr}{dt}\right)\left(\frac{d\phi}{dt}\right) + r^2\left(\frac{d^2\phi}{dt^2}\right)\right] = -qr\left(\frac{dr}{dt}\right) B_z$$

$$m\,\frac{d}{dt}\left[r^2\left(\frac{d\phi}{dt}\right)\right] = \frac{-qB_z}{2}\,\frac{d}{dt}\left(r^2\right)$$

$$\frac{d\phi}{dt} = \frac{-qB_z}{2m} = \text{constant} = k. \qquad (5)$$

Now using (5) in (1) gives

$$m\,\frac{d^2r}{dt^2} - mrk^2 = -qrk\, B_z = 2rmk^2$$

$$\frac{d^2r}{dt^2} + rk^2 = 0$$

which has the solution

$$r = C_1 e^{ikt} + C_2 e^{-ikt}.$$

From the initial conditions at t = 0

$$C_1 = -C_2 = p\sin\theta/2ikm$$

giving

$$r = \frac{p \sin \theta}{km} \sin kt. \qquad (6)$$

Now eliminating t from equations (4) and (6) gives

$$r = \frac{p \sin \theta}{km} \sin \left(\frac{km}{p \cos \theta} z\right)$$

and at $t = T$, this reduces to

$$Z_o B_z = 2\pi \frac{p \cos \theta}{q} . \qquad (7)$$

Therefore, a detector at Z_o with a field B_z will "see" a particle of charge q scattered with momentum $\vec{p}$ at an angle θ with the z axis. Notice that there are two ways to observe different p cos θ values: (1) hold B_z constant and change Z_o by moving the detector, (2) fix the detector at a particular value of Z_o and vary B_z. Thus a knowledge of equation (7) allows one to position a detector to collect all ions within a given momentum interval $|\Delta p|$ at $|p|$ scattered into a conical shell $\Delta\theta$ at θ. In order to make observations, then, one would simply choose the values of p cos θ to be observed, solve the equation for various values of Z_o and B_z that will allow them to be seen, and set the detector and field accordingly.

The solid angle in a spectrometer having azimuthal symmetry depends on θ and p as follows: recall that $d\Omega = 2\pi \sin \theta \, d\theta$ where we have integrated over $d\phi$. An expression for $d\theta$ can be obtained by differentiating equation (7) as follows:

$$Z_o = \left(\frac{2\pi}{qB_z}\right) p \cos \theta$$

and since B_z = constant, then

$$dZ_o = \frac{qB_z}{2\pi} \left(\cos \theta \, dp - p \sin \theta \, d\theta\right)$$

and $$d\theta = \frac{dp}{p \tan \theta} - \frac{qB_z \, dZ_o}{2\pi p \sin \theta} .$$

However,

$$p = (2mE)^{\frac{1}{2}} \text{ or } dp = \left(\frac{m}{2E}\right)^{\frac{1}{2}} dE$$

giving

$$d\theta = \frac{dE}{2E \tan \theta} - \frac{qB_z \, dZ_o}{2\pi (2mE)^{\frac{1}{2}} \sin \theta} .$$

Using this the solid angle is expressed as

$$d\Omega = \left(\frac{\pi \cos \theta}{E}\right) dE - \left(\frac{q^2 B_z^2}{2mE}\right)^{\frac{1}{2}} dZ_o . \qquad (8)$$

Therefore, as seen from equation (8) the solid angle depends on the angle of scatter, θ, the trajectory intercept spread, dZ_o, allowed by the detector, and the energy of the scattered ion, E.

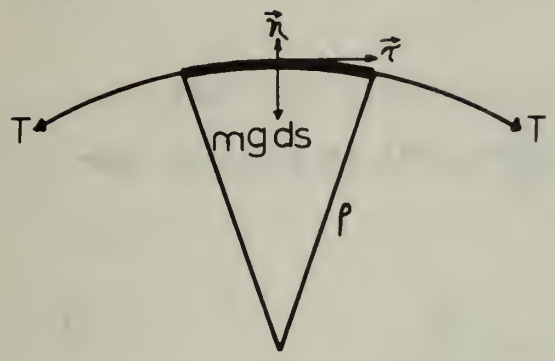
As an example, consider the elastic collision He^+ on He where $\theta = 30^o$, E = 300 eV, dE = 5 eV, B_z = 200 gauss, and dZ_o = - 3mm. Then $d\Omega = 0.058$ steradians, a value typical of solid angles for the nonuniform magnetic field apparatus actually used.

2. ANALOGUE MEASUREMENT OF ORBITS

Prior to obtaining any numerical solutions for the orbit equation, the technique of simulating the orbit of a charged particle in a magnetic field using a current carrying flexible wire was employed to obtain preliminary design information on the various experimental parameters.

The experiment, carried out by Kelly[7], is based on the fact that a current carrying wire consists of charged particles moving with some velocity along the wire, causing the wire to experience a $\vec{v} \times \vec{B}$ force in a magnetic field, the same type of force charged particles encounter.

Consider a small length, ds, of flexible wire carrying a current, i, and under a tension, T, in a magnetic field, B.



p = particle momentum
q = particle charge
ρ = radius of curvature
m = mass/length
i = current
T = tension
$\vec{\tau}$ = unit vector along tangent
$\vec{\eta}$ = unit vector along normal

Then since the system is in equilibrium the sum of the forces is zero, giving

$$ids(\vec{\tau} \times \vec{B}) - T \frac{ds}{\rho} \vec{\eta} - \vec{mg}\, ds = 0$$

from which the curvature of the wire is shown to be

$$\frac{\vec{\eta}}{\rho} = \frac{i}{T} (\vec{\tau} \times \vec{B}) - \frac{\vec{mg}}{T} . \qquad (1)$$

To get the path of a charged particle in a magnetic field, recall that

$$\frac{\vec{dp}}{dt} = q(\vec{v} \times \vec{B})$$

but $\vec{\tau} = \frac{\vec{p}}{p} = \frac{\vec{v}}{v}$ and $ds = vdt$, for constant velocity, v.

Therefore $v \frac{\vec{dp}}{ds} = vp \frac{\vec{d\tau}}{ds} = qv(\vec{\tau} \times \vec{B})$,

however $\frac{\vec{d\tau}}{ds} = \frac{\vec{\eta}}{\rho}$

and the curvature of path of a charged particle is

$$\frac{\vec{\eta}}{\rho} = \frac{q}{p} (\vec{\tau} \times \vec{B}). \qquad (2)$$

Therefore the wire and particle paths will coincide when

$$\frac{i}{T}(\vec{\tau} \times \vec{B}) - \frac{\vec{mg}}{T} = \frac{q}{p}(\vec{\tau} \times \vec{B}). \qquad (3)$$

Now for our case the magnetic force is usually 100 times the gravitational force, hence the gravitational term can be neglected and equation (3) reduces to

$$\frac{T}{i} = \frac{p}{q} . \qquad (4)$$

Thus when equation (4) is satisfied it allows the simulation of charged particle trajectories by a current carrying wire under tension.

The experimental arrangement used to make the wire orbit measurements is shown in Figure 3. An uninsulated wire consisting of 14 strands of number 44 copper wire weighing 0.24 grams/meter was used. Currents of up to 4.5 amps could be passed through the wire, however at the higher currents the wire oxidized and became less flexible. The tension in the wire was normally 1000 dynes and was measured by a modified ammeter movement which was calibrated against a set of weights. This method was chosen over the usual pulley arrangement since the frictional effects in the pulley could not be sufficiently reduced. The departure angle, θ, was measured to an accuracy of $\pm$ 30 minutes of arc by reading the longitudal position of a copper sleeve at the instant it made electrical contact with the wire. The measured departure angle was then corrected to account for the curvature of the wire between the teflon ball and the copper sleeve.

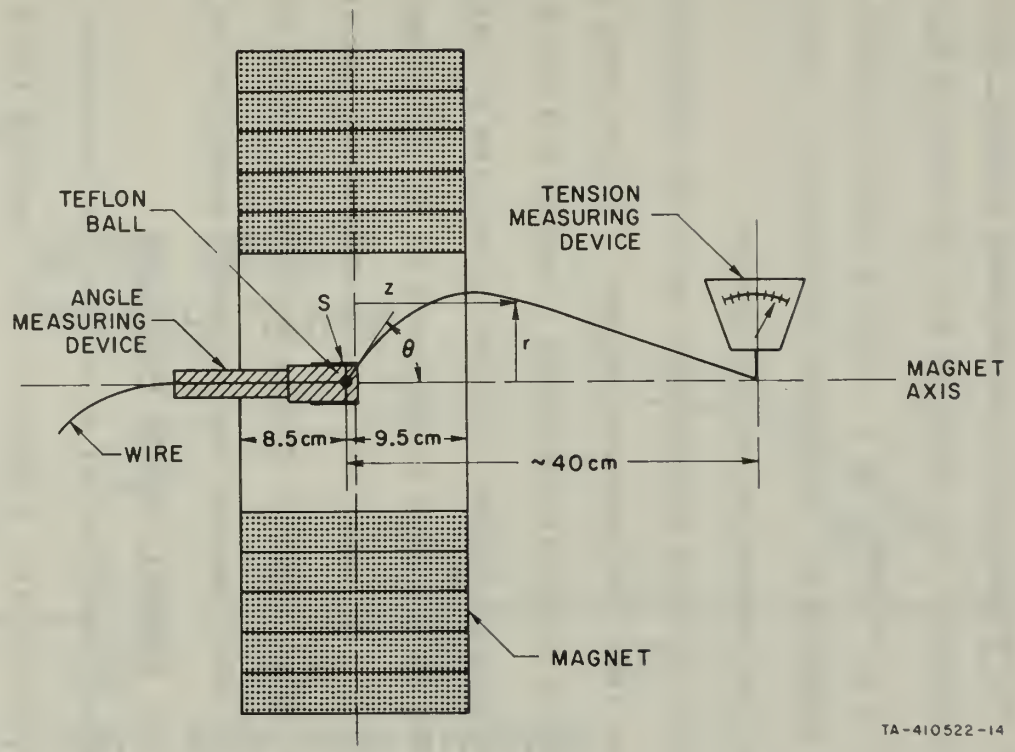


Figure 3. Schematic of Wire Orbit Method

For a given magnetic field and distance Z_o the current through the wire was gradually increased until the desired departure angle was obtained. Then the tension and the current were measured giving the momentum (for an assumed charge) which the wire trajectory represented. The shape of each trajectory was obtained by measuring r as a function of Z. Thirty seven different trajectories were measured and tabulated in reference 7 which also includes a detailed discussion of the method.

A comparison of these measurements with the computed trajectories showed that the measured maximum r values were about 17% larger than the calculated maximum r values and the measured Z_o values were about 8% larger than the calculated Z_o values. The natural stiffness of the wire is believed to be the primary cause of the discrepancy. A comparison of the wire orbit and the calculated trajectories is shown in Figure 4 for an H_2^+ ion with a departure angle of 48.17 degrees and scattered energy of 243 eV.

3. MAGNETIC VECTOR POTENTIAL

The trajectory equation has as one of its parameters the magnetic vector potential. Therefore, the measured field of the magnet must be related to this quantity before the orbits can be found. The well known expansion of $\vec{A}$ in terms of the field is found by following the development used originally by Busch[6].

Since there are no currents in the region of interest

$$\vec{\nabla} \times \vec{B} = 0$$

and, consequently

$$\vec{\nabla} \times (\vec{\nabla} \times \vec{A}) = 0$$

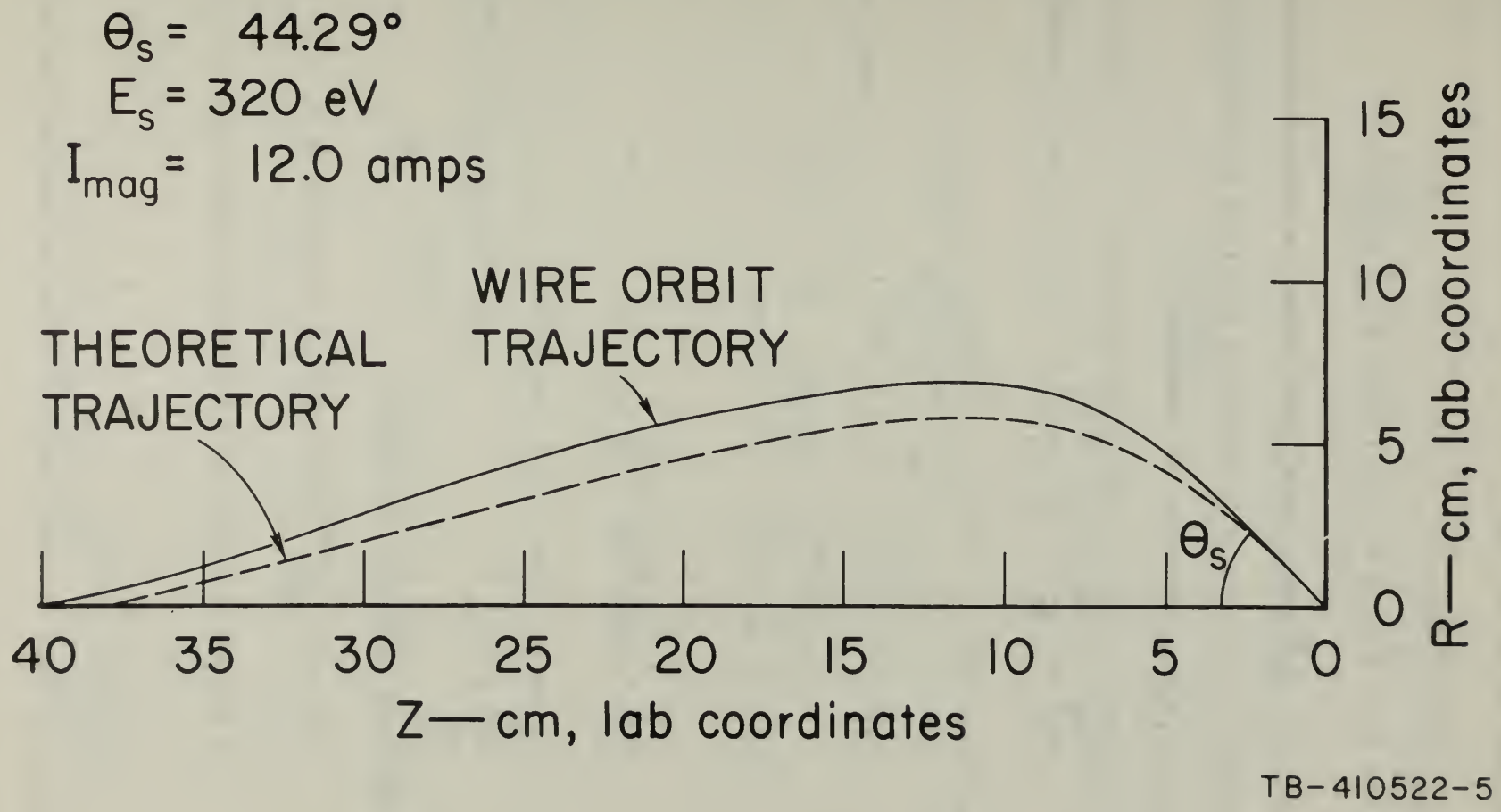


Figure 4. Comparison of Wire Orbit and Computer Trajectories for H_2^+

is the equation to solve. Now

$$\vec{\nabla} \times (\vec{\nabla} \times \vec{A}) = \vec{\nabla}(\vec{\nabla} \cdot \vec{A}) - \nabla^2\vec{A} \qquad (1)$$

and recalling that $\vec{J} = J_{\phi}\,\hat{\phi}$ only, then $A = \frac{\mu}{4\pi}\int \frac{\vec{J}(\vec{r})}{|\vec{r}|}\,dv$ requires that $\vec{A} = A_{\phi}\hat{\phi}$ and $A_r = A_z = 0$. Also, since cylindrical symmetry exists, A_{ϕ} is not a function of ϕ. Thus in cylindrical coordinates, (r,ϕ,z), equation (1) becomes

$$\frac{\partial^2 A_{\phi}}{\partial r^2} + \frac{1}{r}\frac{\partial A_{\phi}}{\partial r} - \frac{A_{\phi}}{r^2} + \frac{\partial^2 A_{\phi}}{\partial z^2} = 0. \qquad (2)$$

Now assume a solution

$$A_{\phi}(r,z) = A(r,z) = \sum_{n=0}^{\infty} a_n(z) r^n,$$

then

$$\frac{\partial A}{\partial r} = \Sigma\, n a_n\, r^{n-1}$$

$$\frac{\partial^2 A}{\partial r^2} = \Sigma n(n-1) a_n\, r^{n-2}$$

$$\frac{\partial^2 A}{\partial z^2} = \Sigma\, a_n''\, r^n.$$

Substituting into equation (2) gives

$$\Sigma\, n(n-1)a_n r^{n-2} + \Sigma\, n a_n r^{n-2} - \Sigma\, a_n r^{n-2} + \Sigma\, a_n'' r^n = 0$$

$$\Sigma\,[n(n-1) + n - 1]\, a_n r^{n-2} + \Sigma\, a_n'' r^n = 0$$

$$\Sigma\,(n-1)(n+1)\, a_n r^{n-2} + \Sigma\, a_n'' r^n = 0.$$

Each coefficient must be zero and shifting indices in the second term gives

$$\sum_{n=0}^{\infty}(n+1)(n-1)a_n r^{n-2} + \sum_{n=2}^{\infty} a_{n-2}'' r^{n-2} = 0,$$

and for $n = 0$: $-1(a_0) = 0$; $a_0 = 0$

$n = 1$: $0(a_1) = 0$; a_1 = arbitrary function of z

$n \geq 2$: $(n+1)(n-1)a_n + a''_{n-2} = 0.$

The recurrence relation for the coefficients is

$$a_n = \frac{-a''_{n-2}}{(n+1)(n-1)}$$

and since $a_0 = 0$, there are only odd n terms in the solution.

The general term is

$$a_{2k+1} = \frac{(-1)^k}{2^{2k} k!(k+1)!} a_1^{(2k)}$$

This gives

$$A(r,z) = \sum_{k=0}^{\infty} \frac{2(-1)^k}{k!(k+1)!} \left(\frac{r}{2}\right)^{2k+1} a_1^{(2k)}$$

or

$$A(r,z) = a_1 r - a_1'' \frac{r^3}{8} + a_1^{(IV)} \frac{r^5}{192} + \cdots .$$

Now to evaluate the coefficient $a_1(z)$ recall from $\vec{B} = \vec{\nabla} \times \vec{A}$

and the field symmetry that

$$B_z = \frac{1}{r} \frac{\partial(rA)}{\partial r} = \frac{1}{r} \frac{\partial}{\partial r} \left[a_1 r^2 - a_1'' \frac{r^4}{8} + a_1^{(IV)} \frac{r^6}{192} - \cdots\right]$$

$$= 2a_1 - 4a_1'' \frac{r^3}{8} + 6a_1^{(IV)} \frac{r^5}{192} + \cdots ,$$

but $B_z(r = 0) = 2a_1$ giving $a_1(z) = \frac{1}{2} B_z(r = 0)$.

This gives

$$A_{\phi}(r,z) = \sum_{n=0}^{\infty} \frac{(-1)^n}{n!(n+1)!} \left(\frac{r}{2}\right)^{2n+1} \frac{\partial^{2n} B_z(r=0)}{\partial z^{2n}} . \qquad (3)$$

Therefore, by knowing $B_z(Z)_{r=0}$ we also know $A_\phi(r,z)$, the quantity used to solve the orbit equation. The actual measurements were fitted to a 12^{th} order polynomial[10] in z such that

$$B_z(z) = \sum_1^{13} C_n z^{n-1}. \qquad (4)$$

With this expression for $B_z(z)$, the field values were reproducible to within 0.1% of the experimentally measured values.

Now using these expressions for $A_\phi(r,z)$ and $B_z(z)$ in the computer program one can calculate the trajectory of a particular $\vec{p}/q$ value for a selected magnetic field.

4. ORBIT EQUATION IN A NONUNIFORM FIELD

The thin lens spectrometer with its axially symmetric nonuniform field was chosen for this apparatus. It more easily produces the large field required to bend ions and it gives more spread in the intercept distances, allowing greater resolution. The equation of motion for a charged particle in an axially symmetric nonuniform magnetic field and the subsequent employment of this field geometry as a β-ray spectrometer has been discussed by several authors[8,9]. Our derivation of the trajectory equation essentially follows that of Busch[6], and was first applied to our particular problem by Gagliano[10].

An axially symmetric magnetic field can be represented by the curl of the magnetic vector potential having only an azimuthal component, A_ϕ (see previous section). The motion of a charged particle in such a field is governed by the equation

$$\vec{F} = q\,\vec{v} \times \vec{B} = q\,\vec{v} \times (\vec{\nabla} \times \vec{A}).$$

In cylindrical coordinates, (r, ϕ, z), the force components are:

$$F_r = m\left[\frac{d^2r}{dt^2} - r\left(\frac{d\phi}{dt}\right)^2\right] = q\,\frac{d\phi}{dt}\,\frac{\partial(rA_\phi)}{\partial r}\,, \tag{1}$$

$$F_\phi = m\left[2\left(\frac{dr}{dt}\right)\left(\frac{d\phi}{dt}\right) + r\frac{d^2\phi}{dt^2}\right] = -q\left[\left(\frac{dz}{dt}\right)\left(\frac{\partial A_\phi}{\partial z}\right) + \frac{1}{r}\,\frac{dr}{dt}\,\frac{\partial(rA_\phi)}{\partial r}\right], \tag{2}$$

$$F_z = m\,\frac{d^2z}{dt^2} = q\,r\,\frac{d\phi}{dt}\,\frac{\partial A_\phi}{\partial z}\,. \tag{3}$$

Now multiplying equation (2) by r and using the relation

$$\frac{d}{dt} = \frac{dz}{dt}\,\frac{\partial}{\partial z} + \frac{dr}{dt}\,\frac{\partial}{\partial r} \tag{4}$$

gives

$$\frac{d}{dt}\left[mr^2\,\frac{d\phi}{dt}\right] = -\,q\left[\frac{d(rA_\phi)}{dt}\right]$$

or

$$\frac{d}{dt}\left[mr^2\,\frac{d\phi}{dt} + q\,rA_\phi\right] = 0.$$

Therefore

$$mr^2\,\frac{d\phi}{dt} + q\,rA_\phi = \text{constant of the motion,}$$

or

$$mr\,\frac{d\phi}{dt} + q\,A_\phi = \text{constant}/r.$$

At $r = 0$ the left hand side is zero requiring that the constant be zero. Thus

$$\frac{d\phi}{dt} = -\,q\,A_\phi/mr. \tag{5}$$

Now substituting (5) into equations (1) and (3) gives

$$\frac{d}{dt}\left(m\,\frac{dr}{dt}\right) = -\frac{q^2}{m}\,A_\phi\,\frac{\partial A_\phi}{\partial r}$$

$$\frac{d}{dt}\left(m\,\frac{dz}{dt}\right) = -\frac{q^2}{m}\,A_\phi\,\frac{\partial A_\phi}{\partial z}\,.$$

Upon rearranging the derivatives in these two equations one obtains

$$\frac{d}{dt}\left(m\,\frac{dr}{dt}\right) = \frac{-q^2}{m}\,A_\phi\,\frac{\partial A_\phi}{\partial r} = m\left(\frac{dz}{dt}\right)^2\frac{d^2r}{dz^2} + \frac{dr}{dz}\left[\frac{dz}{dt}\,\frac{d}{dz}\left(m\,\frac{dz}{dt}\right)\right]$$

and

$$\frac{d}{dt}\left(m\,\frac{dz}{dt}\right) = \frac{-q^2}{m}\,A_\phi\,\frac{\partial A_\phi}{\partial z} = \frac{dz}{dt}\left[\frac{d}{dz}\left(m\,\frac{dz}{dt}\right)\right].$$

They can now be combined into the one equation

$$m\left(\frac{dz}{dt}\right)^2\frac{d^2r}{dz^2} - \frac{dr}{dz}\left[\frac{q^2}{m}\,A_\phi\,\frac{\partial A_\phi}{\partial z}\right] + \frac{q^2}{m}\,A_\phi\,\frac{\partial A_\phi}{\partial r} = 0. \qquad (6)$$

The term $\left(\frac{dz}{dt}\right)^2$ is eliminated using the vector velocity relationship, equation (4), and equation (5), as follows:

$$\vec{v} = \frac{dr}{dt}\,\hat{r} + r\,\frac{d\phi}{dt}\,\hat{\phi} + \frac{dz}{dt}\,\hat{z}$$

or

$$\left(\frac{dz}{dt}\right)^2 = v^2 - \left(\frac{dr}{dt}\right)^2 - r^2\left(\frac{d\phi}{dt}\right)^2$$

and substituting gives

$$\left(\frac{dz}{dt}\right)^2 = \left[v^2 - \left(\frac{q}{m}\,A_\phi\right)^2\right]\Big/\left[1 + \left(\frac{dr}{dz}\right)^2\right].$$

Now replacing $\left(\frac{dz}{dt}\right)^2$ in equation (6) leads to the desired trajectory equation

$$\frac{\frac{d^2r}{dz^2}}{\left[1+\left(\frac{dr}{dz}\right)^2\right]}\left[K^2 - A_\phi^2\right] - \frac{dr}{dz}\left[A_\phi\,\frac{\partial A_\phi}{\partial z}\right] + A_\phi\,\frac{\partial A_\phi}{\partial r} = 0. \qquad (7)$$

where $K^2 = p^2/q^2$.

Therefore one must choose the value of $\vec{p}/q$ to be used and know the relation for $A = f(B_z,z,r)$ developed in the previous section in order to integrate the trajectory equation.

The trajectories were calculated by numerical methods on the available computer. The integration routine, originally written by Gagliano[10], used a fourth order Runge-Kutta method. However, it was rewritten for the IBM 360-67 computer using the Hamming's modified predictor-corrector method which is the DHPGC subroutine of the IBM System/360 Scientific Subroutine Package. The complete computer program is listed in Appendix IV. Figure 5 shows a set of trajectories calculated on the computer for $^{6}Li^{+} + {}^{20}Ne$ where the energy of the incident Li ion was 100 eV. As in the case of the uniform magnetic field there are two methods of detecting particles scattered at different angles: (1) by moving the detector and keeping the focusing magnet current at a specific value; (2) by keeping the distance between the scattering cell and the detector fixed while varying the current through the focusing magnet coil. Both methods were used and acceptable results were obtained from each method.

5. ANGULAR AND ENERGY RESOLUTION

As is shown in the diagram (Figure 6), our experimental arrangement for measuring differential scattering cross sections, $d\sigma(\theta)$, as a function of scattering angle allows a spread of angles $\Delta\theta$ at θ to be admitted by the detector. Therefore there is some angular spread associated with every measurement which causes an uncertainty in the value of $d\sigma(\theta)$ obtained from the measurement. It is seen from the sketch (Figure 6) that the angular spread depends on the size of ΔZ_o, whose value is determined

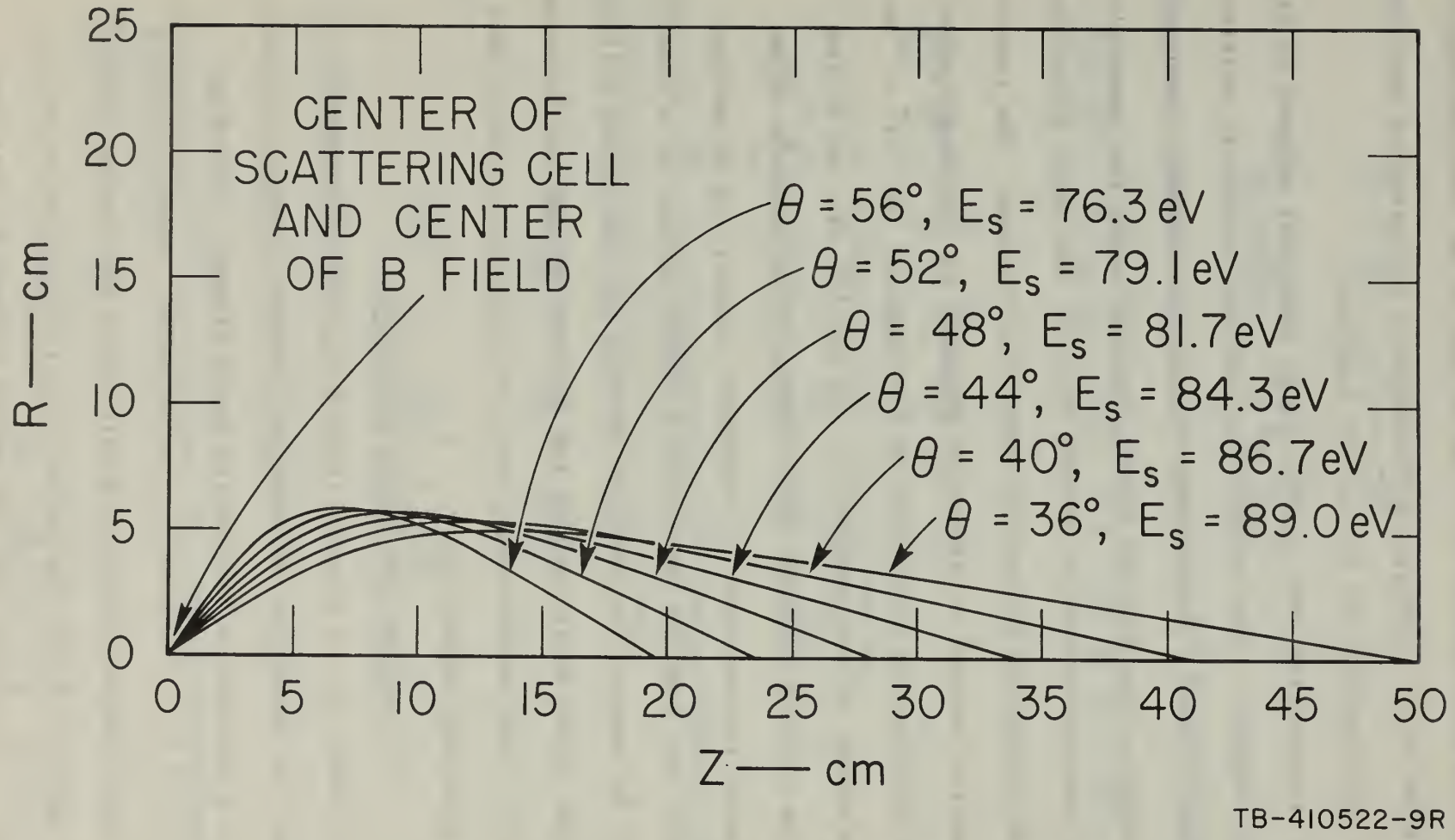


Figure 5. Numerically Computed Ion Trajectories for $^{6}Li^{+}$ on Ne at 100 eV.

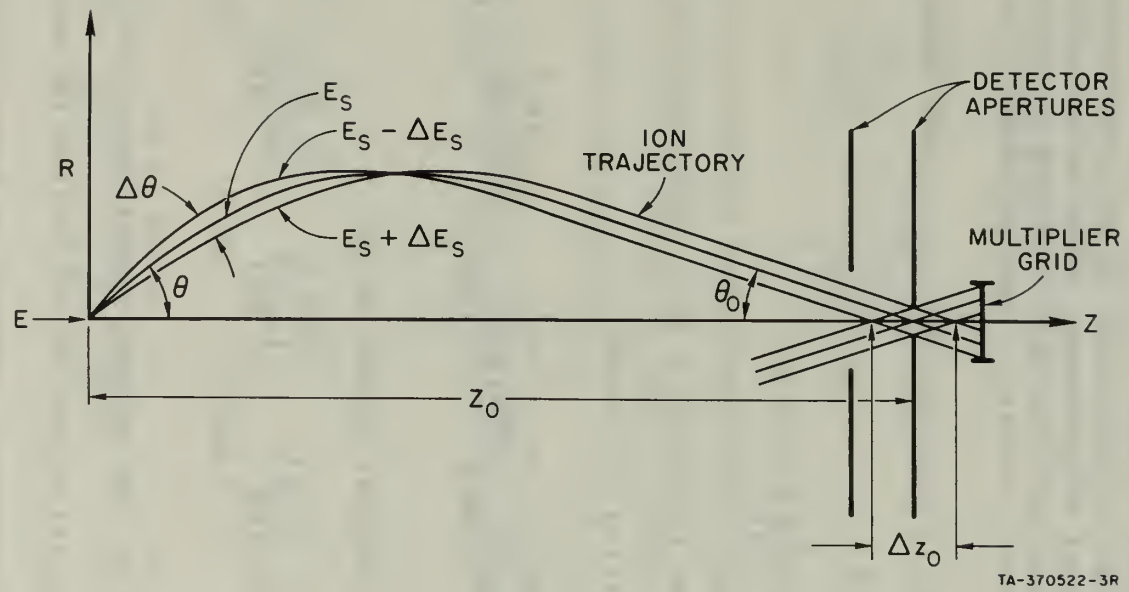


Figure 6. Angular Spread Allowed by the Detector Apertures.

by the detector apertures and θ. Thus, $\Delta\theta$ can be calculated from the relation between $\Delta\theta$ and ΔZ_o. This relation is obtained from

$$Z_o = f(E,\theta,B,R',Z',C) \qquad (1)$$

where E = energy of the incident ion
θ = angle of scatter
B = Magnetic field = $f(I)$; I = coil current
R' = target displacement from system axis
Z' = target displacement from system center
C = a constant for each reaction including mass ratios, inelastic energy losses, etc.

The coil current is constant during a given measurement making $dI = 0$, therefore

$$dB = \left(\frac{\partial f}{\partial I}\right) dI = 0.$$

Also, for a given reaction, C is a constant which makes $dC = 0$. Thus differentiating (1) leads to

$$dZ_o = \left(\frac{\partial Z_o}{\partial E}\right)_{\theta R' Z'} dE + \left(\frac{\partial Z_o}{\partial \theta}\right)_{E R' Z'} d\theta + \left(\frac{\partial Z_o}{\partial R'}\right)_{E \theta Z'} dR' + \left(\frac{\partial Z_o}{\partial Z'}\right)_{E \theta R'} dZ' .$$

Solving for the angular spread we get

$$d\theta = \left(\frac{\partial \theta}{\partial Z_o}\right)_{E R' Z'} dZ_o - \left(\frac{\partial \theta}{\partial Z_o}\right)_{E R' Z'} \left[\left(\frac{\partial Z_o}{\partial E}\right)_{E R' Z'} dE + \left(\frac{\partial Z_o}{\partial R'}\right)_{E \theta Z'} dR' + \left(\frac{\partial Z_o}{\partial Z'}\right)_{E \theta R'} dZ'\right]. \qquad (2)$$

The values of the various quantities in the expression for the angular resolution must be calculated for each and every cross section that is measured. However as shown by example in Appendix I the terms arising from the energy spread and the finite target size increase $d\theta$ by less than 10% for ion beam energy spreads less than 0.5 eV. Therefore the angular resolution is

$$d\theta = \left(\frac{\partial \theta}{\partial Z_o}\right)_E dZ_o \qquad (3)$$

when the terms containing dE, dR', and dZ' are ignored.

The second quantity of interest is the spread in energies, dE_s, that particles scattered at θ may have and still be detected. As can be seen from Figure 6, this quantity depends upon $\Delta\theta$ at θ and also upon the energy of the incident ion, E, and the reaction parameter C. Therefore

$$E_s = E_s\ (E,\theta,C)$$

and upon differentiating

$$dE_s = \left(\frac{\partial E_s}{\partial E}\right)_\theta dE + \left(\frac{\partial E_s}{\partial \theta}\right)_E d\theta.$$

If one considers only elastic processes, where the incident ion of mass m interacts with a target of mass M, then, due to the conservation of energy and momentum[11],

$$E_s = E\ \frac{M^2 - m^2 + 2m^2 \cos^2\theta + 2m \cos\theta \sqrt{M^2 - m^2 + m^2 \cos^2\theta}}{(M + m)^2}.$$

Using this

$$\left(\frac{\partial E_s}{\partial E}\right)_\theta = E_s/E$$

and

$$\left(\frac{\partial E_s}{\partial \theta}\right)_E = \frac{-2m\ E_s\ \mathrm{Sin}\ \theta}{\sqrt{M^2 - m^2 + m^2 \cos^2\theta}}$$

giving

$$dE_s = \left(\frac{E_s}{E}\right)_\theta dE - \left(\frac{2m\ E_s\ \mathrm{Sin}\ \theta}{\sqrt{M^2 - m^2 + m^2\ \mathrm{Cos}^2\theta}}\right)_E d\theta\ . \qquad (5)$$

Using equations (3) and (5) one can evaluate the angular resolution for a particular cross section. As an example, for the reaction $^{6}Li^{+}$ on He at 300 eV, I = 13.0 amps, dE = 0.25 eV and $\theta = 39.6^{o}$, one obtains

$$d\theta = 0.38^{o}$$

and

$$dE_{s} = 3.77 \text{ eV}$$

which are representative values of the reactions that were observed.

6. SOLID ANGLE

The major advantage of this method of measuring differential scattering cross sections is the greatly enhanced solid angle obtained by collecting all particles scattered into a conical shell $d\theta$ at θ. The solid angle for this system is

$$d\Omega = 2\pi \sin\theta \; d\theta.$$

As can be seen from Figure 6 all the particles scattered at θ must cross the axis in ΔZ_{o} at Z_{o} in order to be detected. This ΔZ_{o}, then, determines $d\theta$ at θ and, consequently, the value of the solid angle at θ. In the discussion of the angular resolution the expression

$$d\theta = \left(\frac{\partial\theta}{\partial Z_{o}}\right)_{E} dZ_{o}$$

was obtained. This is the relation used to calculate the solid angle. Thus

$$d\Omega(\theta) = 2\pi \sin\theta \left(\frac{\partial\theta}{\partial Z_{o}}\right)_{E} dZ_{o} .$$

However only 290^{o} of the available 360^{o} of the axial angle were open because of the way the scattering cell is constructed (see Chapter III, Section 5, for a full explanation). Correcting for this and expressing $\partial\theta_o/\partial Z_o$ in degrees/centimeters, the solid angle expression is written

$$d\Omega(\theta) = 0.0873 \sin\theta \left(\frac{\partial\theta}{\partial Z_o}\right)_E dZ_o \text{ steradians.}$$

This expression must of course be evaluated for every trajectory to be measured since it depends not only on the angle of scatter, θ, but also on ΔZ_o and the derivative $(\partial\theta/\partial Z_o)_E$. All of these quantities depend upon the particular ion trajectory considered.

Some representative values of the solid angle as a function of θ at various focusing magnet currents are shown in Figure 7. These curves are for the reaction $^{6}Li^{+} + {}^{20}Ne$ at 100 eV incident ion beam energy. Notice the dependence of the solid angle on the angle of scatter and the focusing magnet current (magnetic field). When the magnet current is held constant the intercept distance changes for each angle of scatter causing the solid angle to vary. These values at the solid angle are typical for all reactions observed.

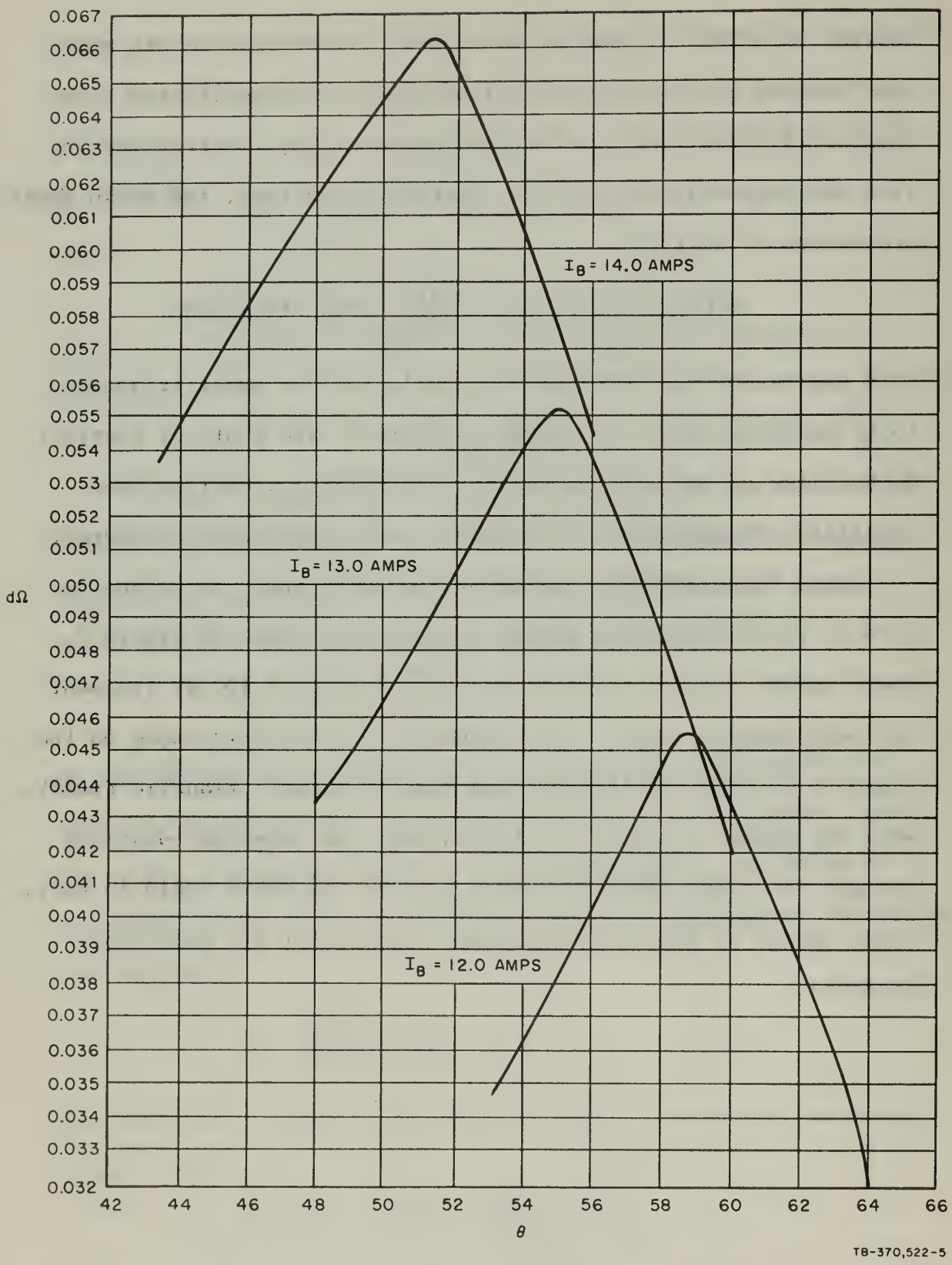


Figure 7. Solid Angle vs Angle of Scatter for Elastic Scattering of $^{6}Li^{+}$ on Ne at 100 eV Incident Ion Energy

CHAPTER III

EXPERIMENTAL APPARATUS

1. VACUUM SYSTEM

The vacuum shell shown in Figure 8 consists of aluminum cans with neoprene O-rings at the connecting flanges, feed throughs, and end plates.

Two six-inch diffusion pumps are used to maintain the vacuum. A National Research Corporation Model VHS6 diffusion pump having a 2400 liter per second pumping speed is connected to the detector end of the system. Water cooled baffles and a liquid nitrogen cold trap are located between the detector chamber and the diffusion pump. The forepump is a CENCO HYVAC 45 mechanical pump with a 280 liter per minute capacity. A stacked half-moon baffle is placed in the foreline to reduce backstreaming from the forepump. At the opposite end of the system, where the ion source and the mass analyser are located, a Dresser Model DPD-6 diffusion pump is utilized. The Dresser pump has an 1800 liter per second pumping speed and is connected to a Welch Duo-Seal forepump. Water cooled baffles and liquid nitrogen trap are installed between the diffusion pump and the mass analyser chamber. Dow Corning 704 diffusion pump oil is used in both diffusion pumps. This arrangement provides ultimate pressures of 2.0×10^{-7} Torr in the detector chamber, and 1.0×10^{-7} Torr in the ion source chamber. With gas in the scattering cell at a pressure of 2.0×10^{-3} Torr the pumps maintain the detector chamber at 2.0×10^{-5} Torr and the mass analyser chamber at 4.0×10^{-6} Torr. These pressures are low enough to insure that reactions outside

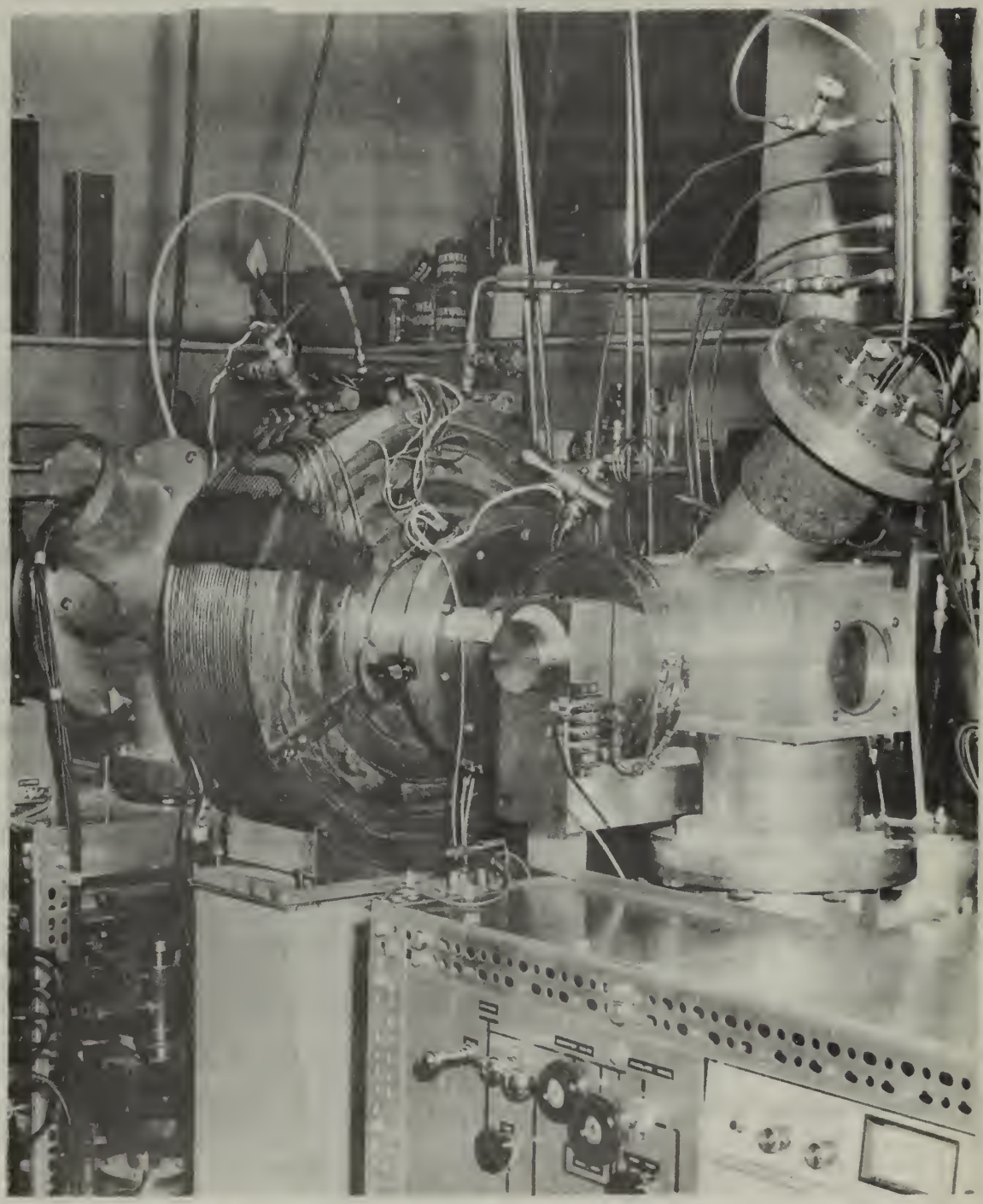


Figure 8. Experimental Apparatus

the scattering cell are negligible. Tests also showed that the pressure in the detector chamber is low enough to eliminate any pressure effects on the electron multiplier which served as the detector for the scattered particles.

2. ION SOURCES

In order to generate the ion beams used in the differential scattering cross section measurements, two different types of ion sources were used: Lithium ions were produced by a thermal emitter; helium and hydrogen ions by an electron impact source. The pertinent facts for both types of sources are reported here while a more detailed account of our developmental work on the electron impact source is presented in Appendix VI.

Lithium Ion Source

The lithium ion source used was essentially the source described by Heinz and Reaves[12] and is shown in Figures 9 and 10. It is a thermal emitter consisting of a very porous tungsten matrix into which the minerals beta-eucryptite ($Li_2O \cdot Al_2O_3 \cdot 2SiO_2$) or spodumene ($Li_2O \cdot Al_2O_3 \cdot 4SiO_2$) have been fused. The lithium ions are produced when the tungsten matrix is heated to temperatures in excess of 1100°C by a separate filament (see Figure 10). The emitter was enclosed in a heat shield to keep filament power requirements low. The shielded emitter was mounted on a 8-1/2 inch diameter stainless steel flange using a stainless steel mounting. In front of the emitter was an extraction electrode and a three electrode einzel lens. To extract the ion beam, the emitter, shield, and filament were placed at a potential corresponding to the desired beam energy. The filament power was

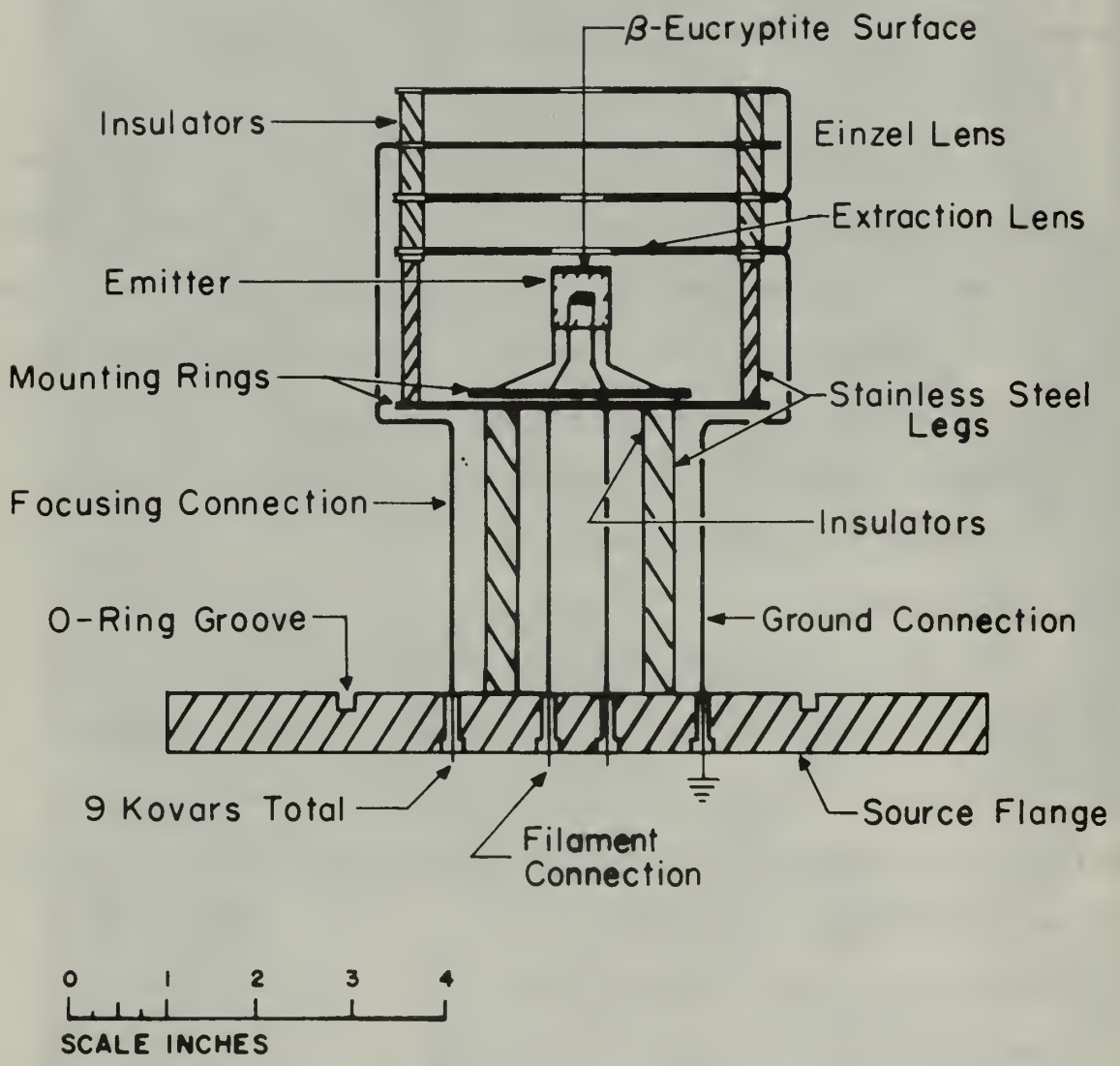


Figure 9. Schematic of the Lithium Ion Source.

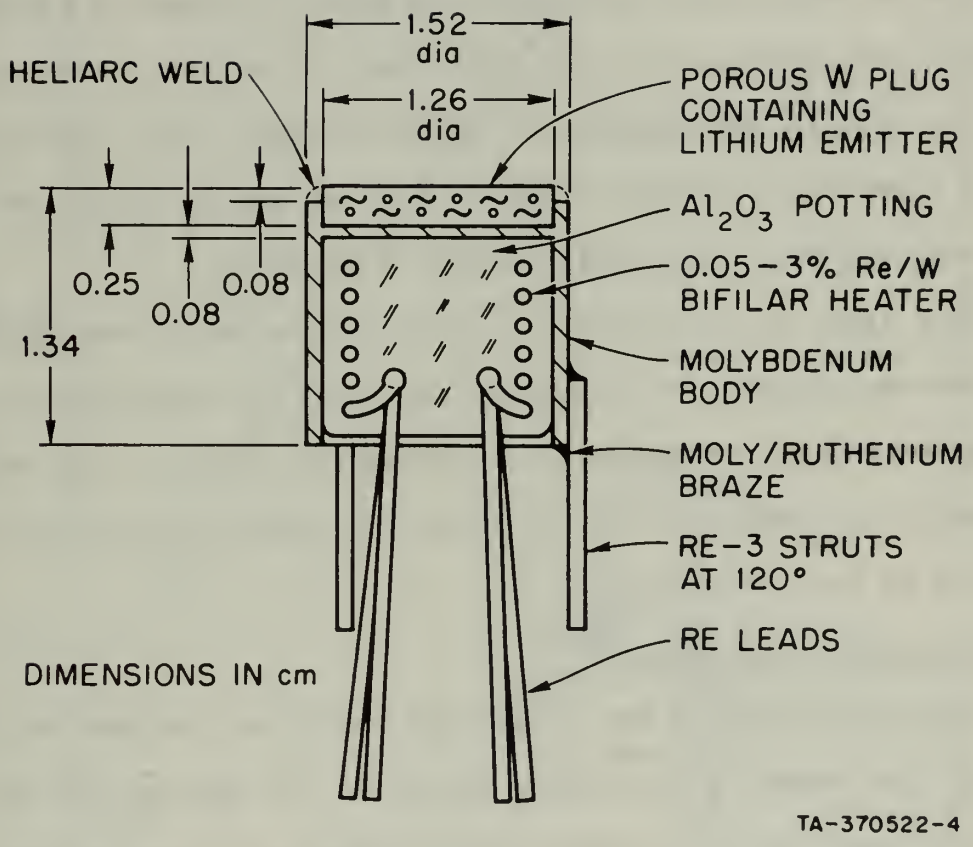


Figure 10. Lithium Ion Source Emitter Detail.

adjusted for an emitter temperature of about 1170°C which was found to be an optimum operating point. The effect of the emitter temperature on the total ion emission is shown in Figure 11. The extraction grid was grounded producing a beam of the desired energy. The einzel lens apertures were 1.4 centimeters in diameter and the lenses were 1.4 centimeters apart. The center lens was 4.0 centimeters from the extraction electrode. These dimensions were obtained from the einzel lens relations given in Appendix VI and produced ion beams up to 1.0×10^{-7} amps in the scattering cell when the emitter was operated at optimum output. The ion beam obtained from the source was found to have an energy spread of no more than 0.5 eV in the energy range 15 to 800 eV.

This type of ion source has several advantages over plasma type sources: simplicity of operation, small gas load on the system, stable and highly monoenergetic beams of high purity. The major drawback of course is a limited number of species which can be produced by this technique.

Electron Impact Ion Source

This ion source is one of a large family of sources which produces ion beams by creating a plasma in the appropriate gas and extracting ions from the plasma by externally applied electrostatic fields. In the particular source shown in Figure 12, the plasma is produced by electron bombardment of the low pressure gas. Electrons, emitted from the filament, accelerated radially outward through the concentric grid and decelerated as they approach the cylindrical walls, oscillate between the filament and the wall until they are collected on the grid. The

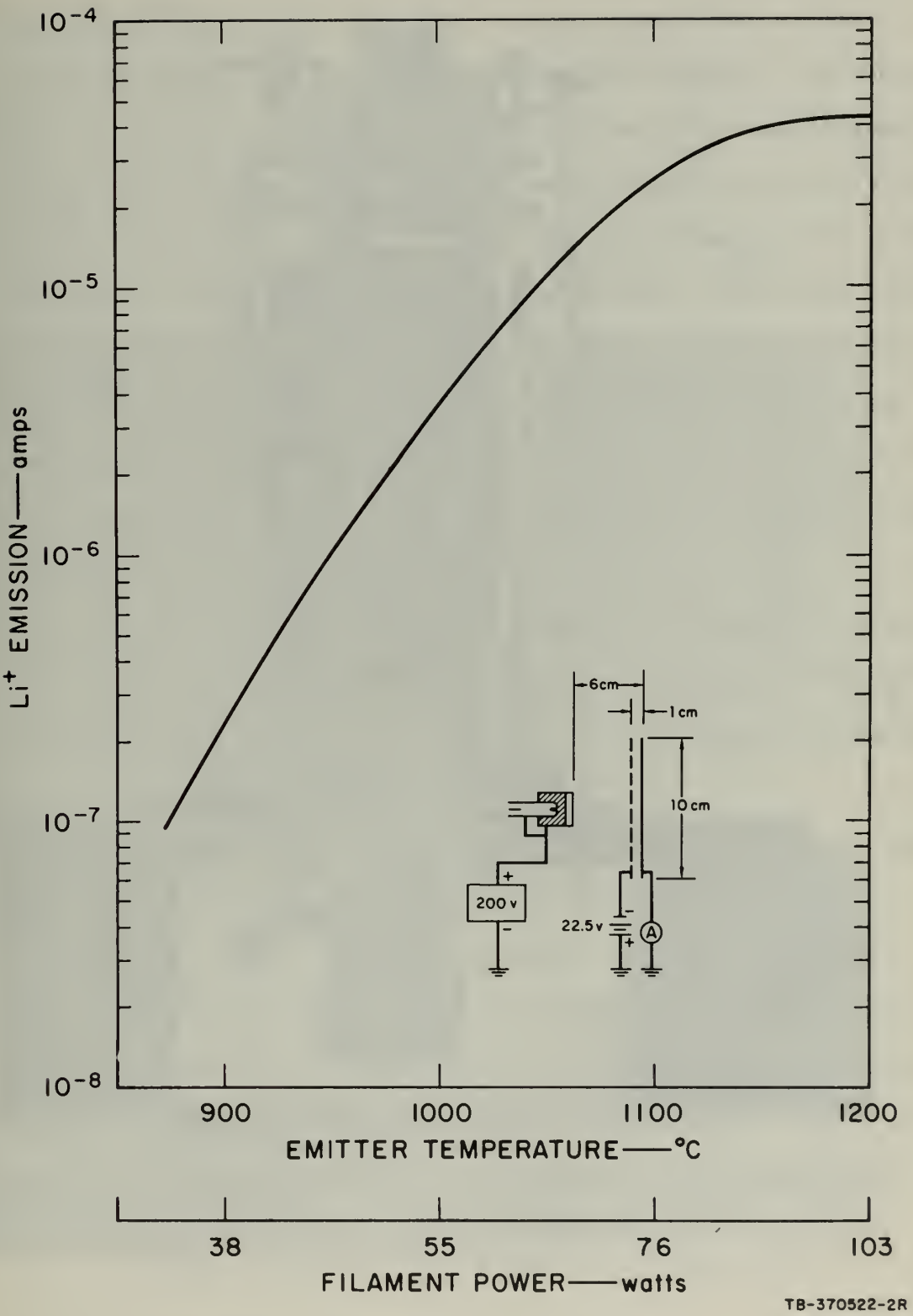


Figure 11. Lithium Ion Source Emission Curve.

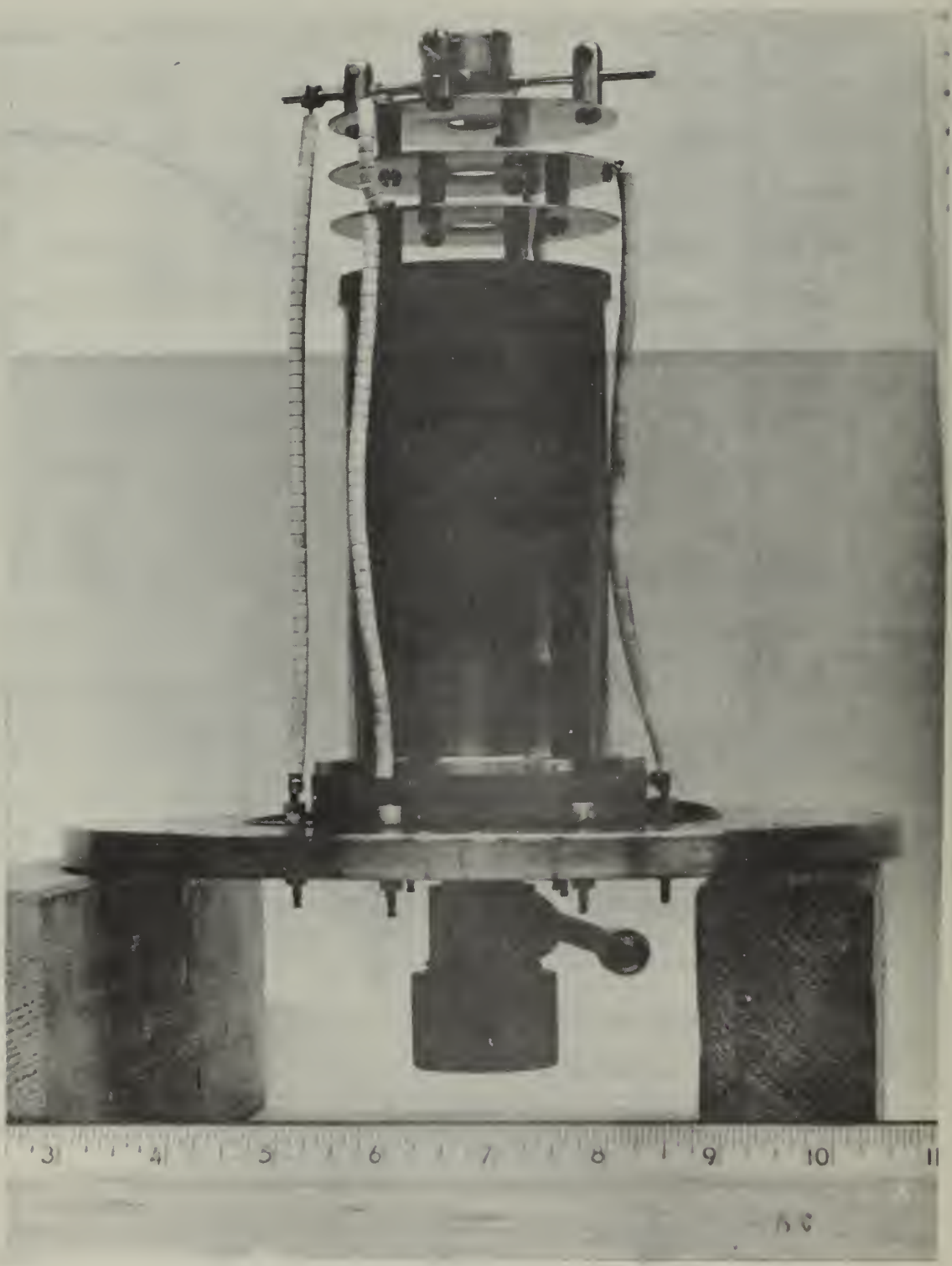


Figure 12. Electron Impact Ion Source.

plasma forms between the grid and filament and the ions are extracted axially from it. To produce an ion beam, source gas is introduced into the source can at a rate that will maintain a pressure of about 1×10^{-3} Torr within the source. The potentials are set at the desired ion beam energy and the filament power is increased until enough electrons (usually about 90 ma) are produced to maintain the discharge. The grid is usually 100 volts above the common can and filament potentials. An einzel lens placed directly in front of the extraction hole helps produce ion beams up to 3.0×10^{-8} amps in the scattering cell. Our measurements indicate a rather large energy spread of about 8 eV although other workers using the same source have reported energy spread as low as .5 eV*.

The source is fairly easy to operate and maintain, although requiring more maintainance than the lithium source. The primary drawbacks are the gas load it imposes on the vacuum system and the fairly large energy spread.

A more detailed account of our developmental work on this ion source is presented in Appendix VI.

3. MASS ANALYSER

The ion sources used tend to produce a variety of ions from the same source. This was especially true when using a plasma type ion source. Although the source parameters could be varied to enhance the production of one particular ion, other ions could

*Private communication from Dr. W. Aberth, SRI.

not be reduced to insignificant values. Therefore, it was decided that mass analysis of the ion beam prior to its entering the scattering cell was necessary.

The mass analyser shown in Figure 13 was designed and calibrated by Strohsahl[13]. It has a 45^{o} angle of bend in order to allow for both high beam transmission, up to 90%, and a resolution $\Delta m/m$ of about 40 allowing mass analysis of singly charged particles up to mass number 40 and energies up to one kilovolt. Using a coil current of 8 amps, it had a maximum field strength of about 4000 gauss confined between 40^{o} wedge sector shaped pole pieces with a 3/4 inch gap width. The pole pieces were external to the vacuum system which allowed increased flexibility and enhanced the vacuum integrity of the entire system.

One effect resulting from the use of the mass analyser was the reduction of background signal at the detector by a factor of 100 or more. This fact made it worth while to use the mass analyser even in cases where the ion source did produce only one type of ion.

4. FOCUSING MAGNET

The magnet cell consists of five concentric brass spools wound with a total of 7938 turns of number 15 wire connected in such a way (see Table I) that the total resistance was approximately 10.75 ohms. A single layer of 1/4 inch outside diameter copper tubing was placed over the outermost layer of wire on each spool. Water was run through the tubing for cooling. Thus it was possible to use up to 14 amps through the coils. A Sorenson Nobatron model DCR 150-15 power supply was used to supply the required magnet coil current regulated to $\pm$ 0.1%.

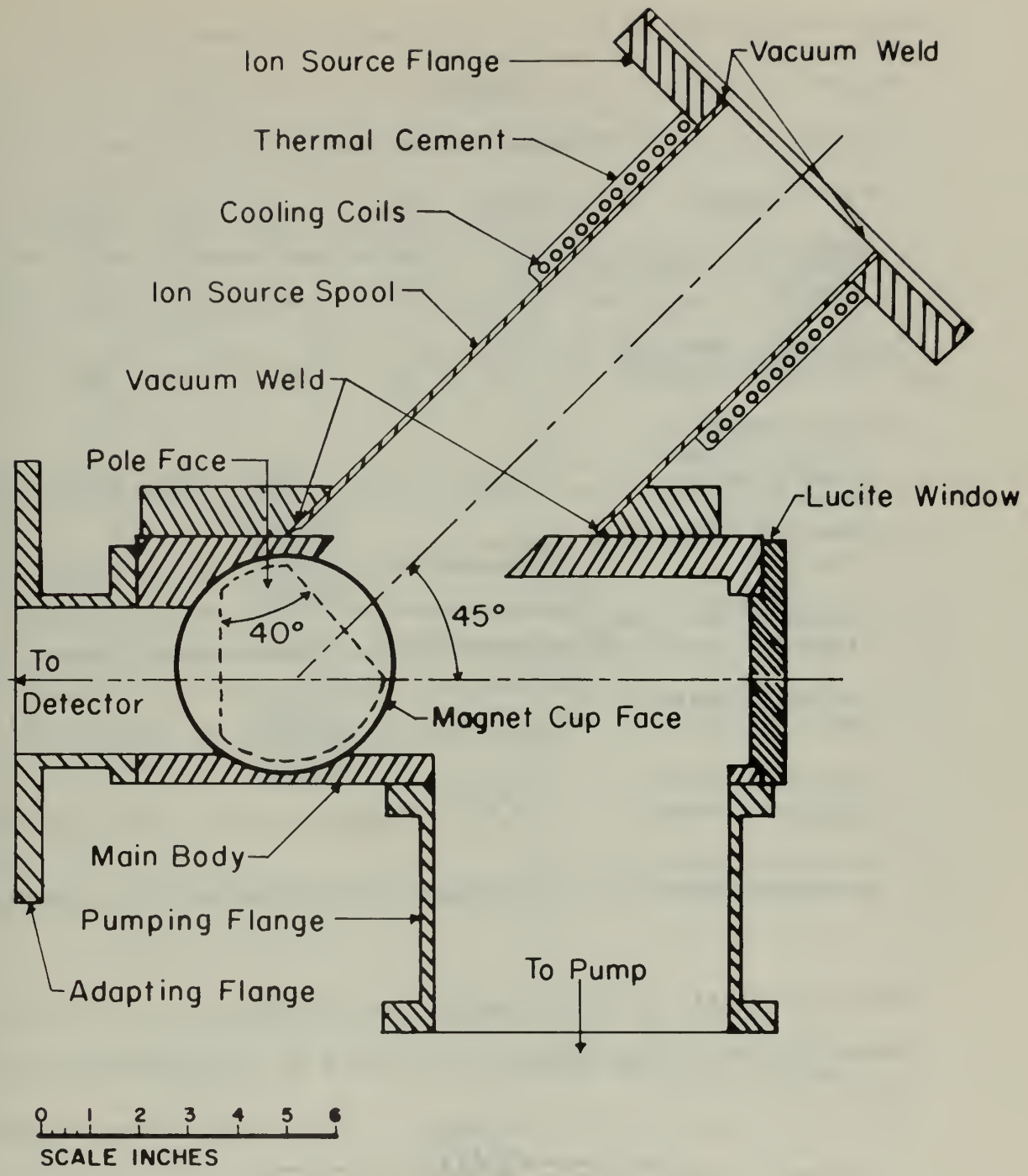


Figure 13. Schematic of Mass Spectrometer.

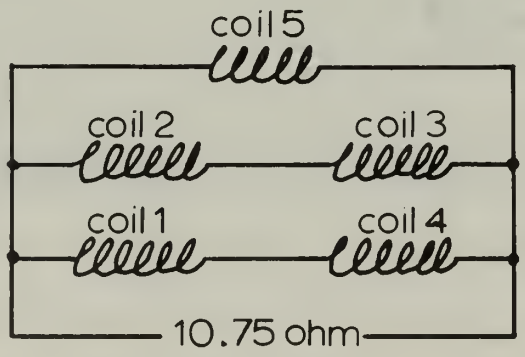
TABLE I

FOCUSING MAGNET DATA

ITEM	COIL 1	COIL 2	COIL 3	COIL 4	COIL 5	TOTAL
1. Number of layers of winding	22	18	16	12	14	82
2. Average number of turns per layer*	97	95	97	99	98	
3. Total number of turns on spool (item 1 x item 2)	2116	1710	1552	1188	1372	7938
4. Measured resistance (ohms)	20.46	18.36	20.86	18.04	23.92	10.75
5. Length of wire (ft) (item 4 x 1000/2.58)**	6010	6790	7560	6790	9300	36,450
6. Inside diameter of spool (inches)	7.750	11.155	14.300	17.250	19.750	7.750
7. Inside diameter of winding (inches)	8.000	11.400	14.550	17.500	20.000	8.000
8. Outside diameter of spool (inches)	11.140	14.285	17.235	19.735	22.250	22.250

*Based on actual count of several random layers.

**Based on nominal resistance for 15 wire of 3.25 ohms/1000 ft at 25°C.



COIL ARRANGEMENT

Since the magnetic vector potential can be expressed in terms of the axial component of the magnetic field on the axis only this quantity was carefully measured. The measurements were carried out by Kelly[7] using a Hall probe calibrated in a magnetic field varied from 0 to 5 kilogauss against a known nuclear magnetic resonance probe accurate to ± 1 gauss at 1000 gauss. Figure 14 illustrates the method used to position the magnetic field probe.

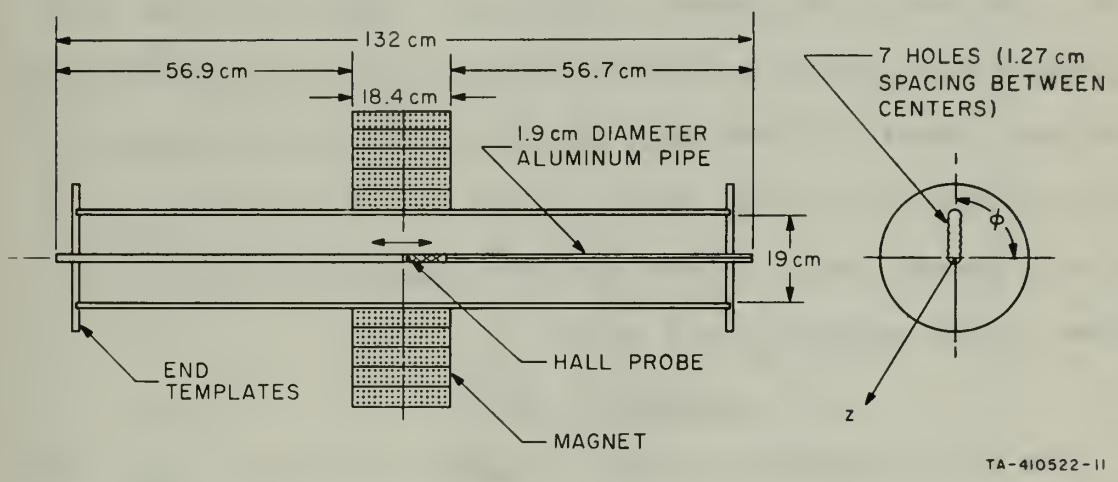


Figure 14. Arrangement for Measuring the Magnetic Field.

The probe was placed inside an aluminum pipe on the tip of a wooden rule accurate to 0.5 mm. The wooden rule provided an adequate measurement of the distance of the Hall probe from the center of the magnet. The aluminum pipe holding the probe was fitted through templates at either end of a larger aluminum pipe held rigid inside the magnet coil and positioned concentric with the magnet coil axis. The end plates could be rotated to different radial angles and they had seven holes, 1.27 cm apart, along a radius which allowed field measurements at various r and Ø values.

The axial component of the magnetic field on the axis was measured at 4 centimeter intervals at current settings of 2,4,6, 8,10,12, and 14 amps. A plot of these measurements is shown in Figure 15. These values were fitted to a $12^{\underline{th}}$ order polynomial in Z and used to calculate the magnetic vector potential as explained in Section 3 of Chapter II. Figure 16 shows the value of the axial component of the magnetic field measured at various r and Ø values at the center of the coil. These and other measurements tabulated in reference 7 demonstrated that the magnetic field was symmetric about both the center of the coil and the coil axis to within 0.1%. This allowed use of the coil axis and coil centerline as references for alignment of the entire system to the magnetic field axis.

5. SCATTERING CELL

The scattering cell, shown in Figures 17 and 18, constructed of stainless steel, is designed to allow particles scattered at all azimuthal angles to leave the scattering cell and eventually be collected at the detector. Figure 18 illustrates how this was accomplished by opening the scattered beam exit slit about 290^{o} around the scattering cell.

Attached to the front of the scattering cell is a circular aperture of variable diameter which can be adjusted from outside the vacuum system. Through appropriate wiring the ion currents to the front section of the scattering cell can be monitored. In the front section of the scattering cell a 0.5 centimeter diameter by 1.0 centimeter long beam entrance tube was drilled. These dimensions were chosen to reduce gas flow out from the scattering

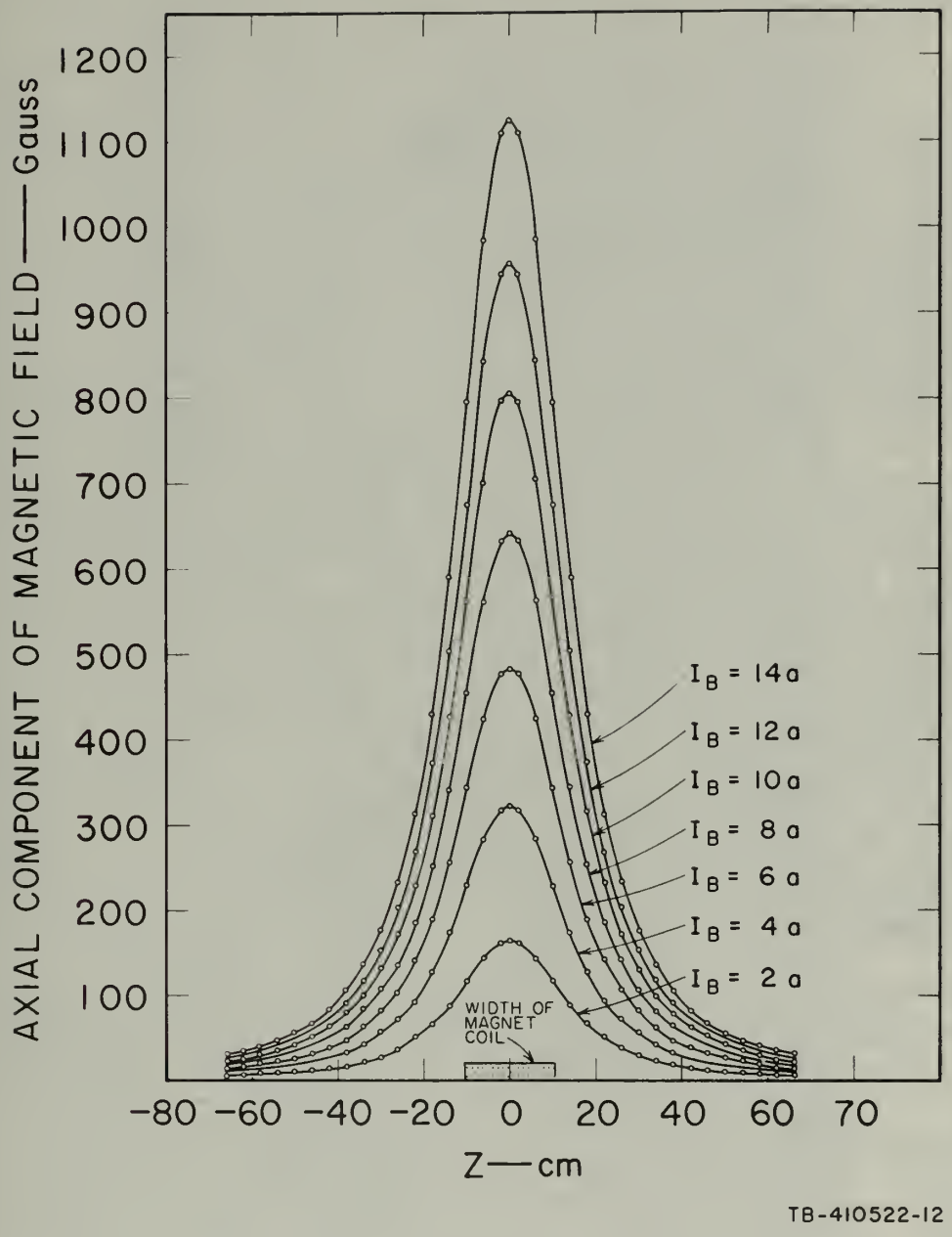


Figure 15. Axial Magnetic Field Strength vs Distance.

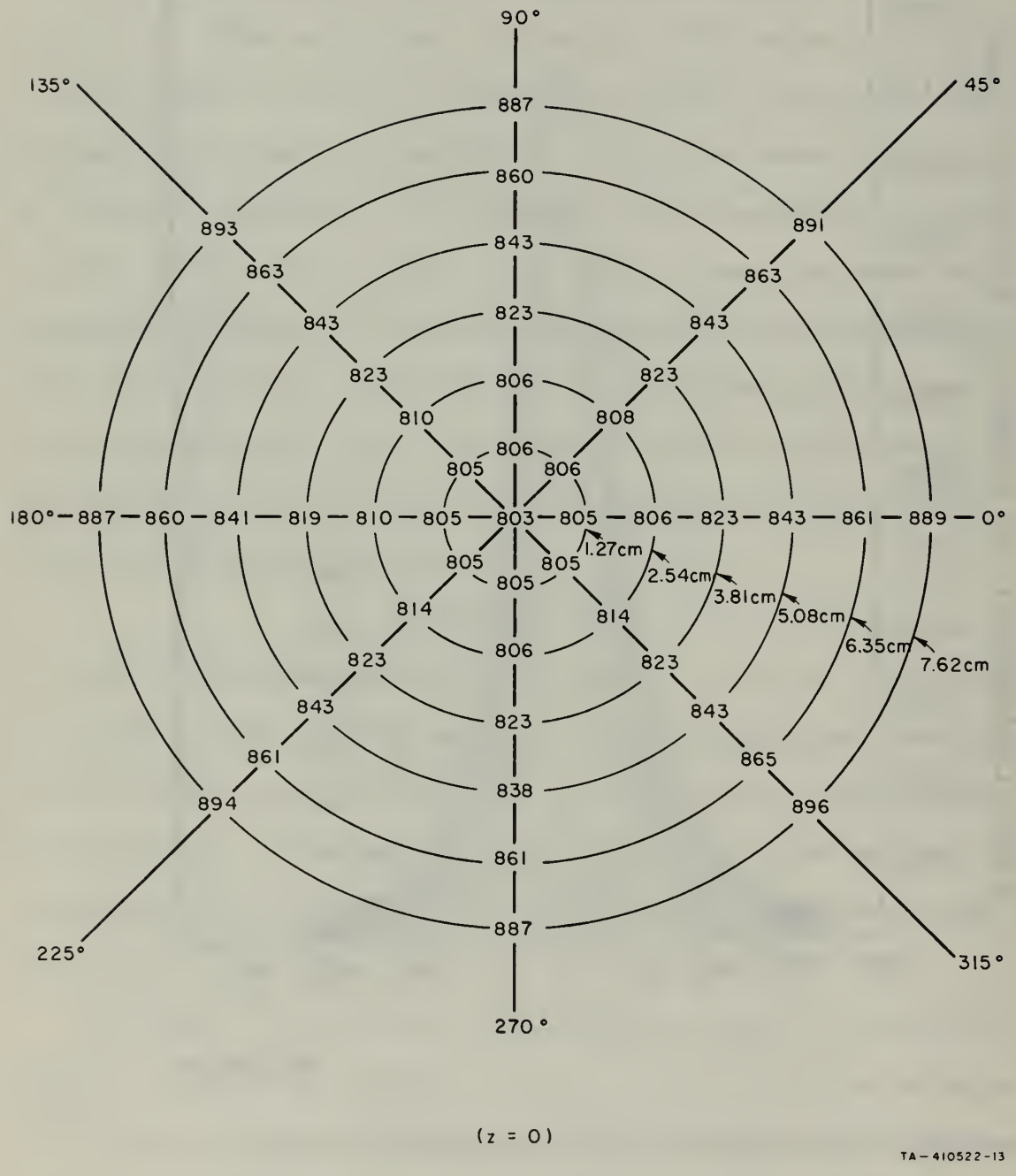


Figure 16. Axial Magnetic Field Strength Measured at Various r and Ø Values.

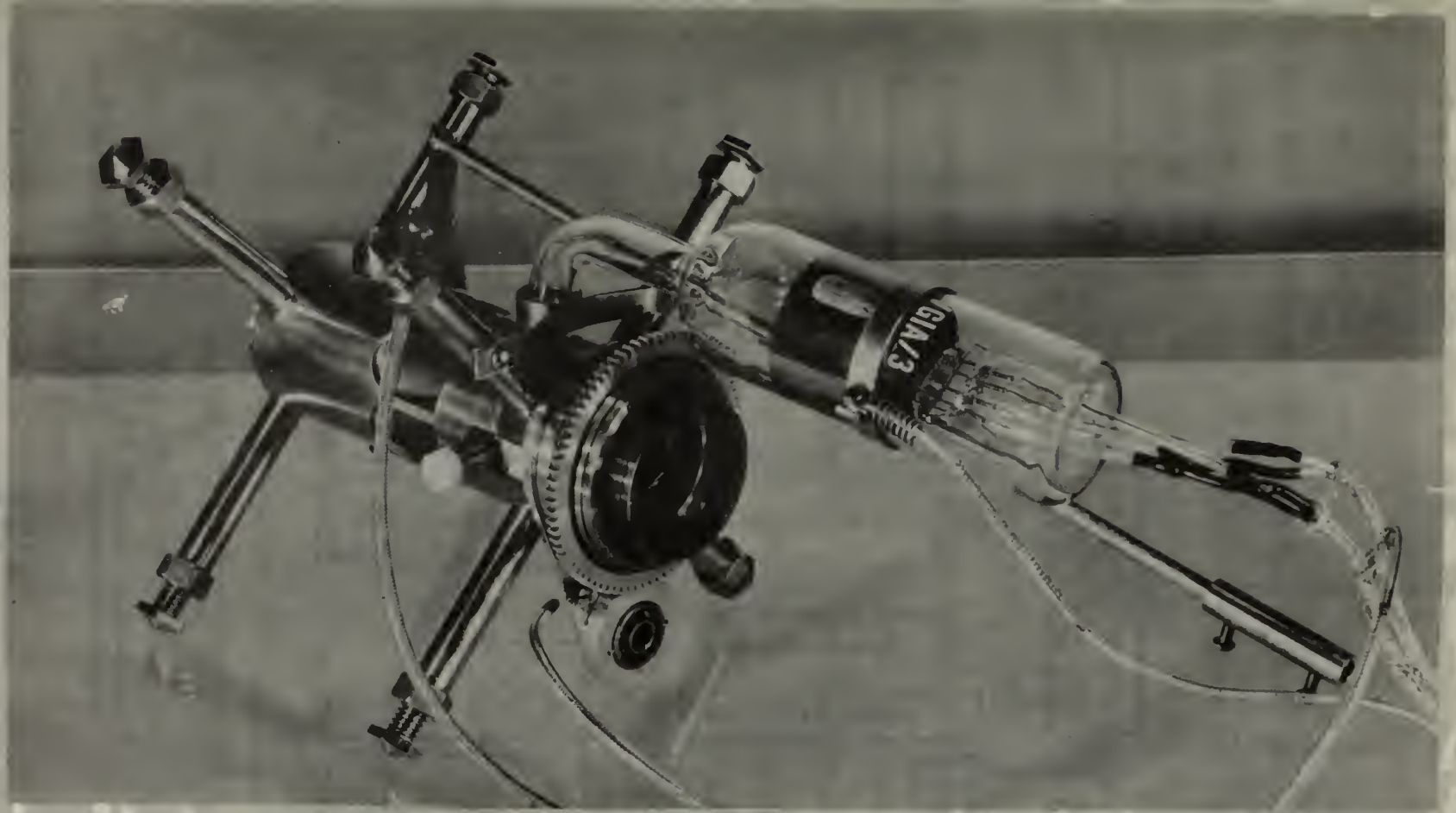


Figure 17. Scattering Cell.

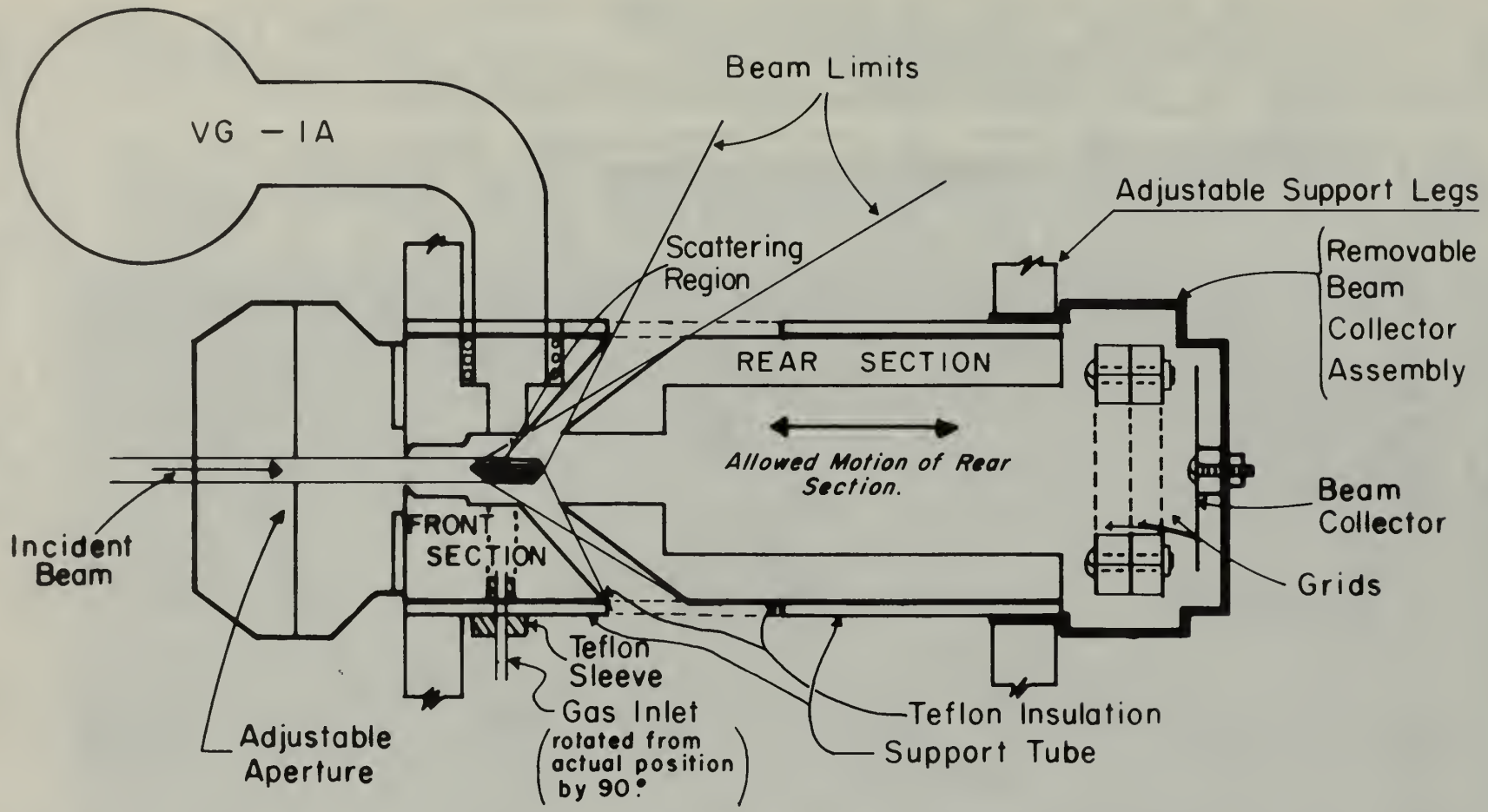


Figure 18. Schematic of Scattering Cell and Beam Collector.

cell and allow maximum flexibility in the 1.0 centimeter diameter by 1.0 centimeter long scattering chamber itself. Into the bottom of this chamber a 1/8 inch outside diameter copper tube was placed, through which target gas entered. A precision gas metering valve placed at the other end of the inlet tube was used to allow precise control of the gas flow into the scattering chamber. A VG-1A ion gauge was located so that its entrance tube was placed 90° from the gas inlet tube. The narrowest portion of the path to the ion gauge was 0.5 centimeters in diameter, occuring where it entered the scattering chamber itself. From the rear of the scattering chamber the front section of the scattering cell sloped upward to the outer edge of the cell at an angle of 49° from the horizontal. This surface acts as the front edge of the scattered beam exit slit. The back edge of the slit was formed by the face of the rear of the scattering cell which sloped upward at an angle of 36°. As shown in Appendix III these two angles determined the gas target thickness. The inside of the rear of the scattering cell was opened up to a 2.54 centimeter diameter in order to allow free travel of the unscattered ion beam to the beam collector. This after section is also wired so that ion currents to it can be measured. The rear section of the scattering cell can be moved horizontally from outside the vacuum system. In this way the target thickness could be varied. The opening could be adjusted to any desired length from fully closed to up to 0.8 centimeters when fully opened.

The front and rear sections of the scattering cell were placed inside a stainless steel tube (0.18 centimeter wall thickness) and separated from it by teflon insulation. The support tube ran the length of the entire scattering cell but was cut away at the exit slits so that only 19% of the tube was left to obstruct the scattered beam. This area was accounted for in the calculation of the solid angle. The tube has four variable length legs on each end (a total of eight). The individual legs in each set are placed 90^{o} apart around the circumference of the tube end. This arrangement gives very stable support to the cell and yet allows easy adjustment for alignment.

The beam collector consists of three grids and a collector. Normally, the grid farthest from the collector was grounded, the middle grid was given s small positive potential to keep slow positive ions from reaching the collector, and the grid nearest the collector was given a small negative potential to suppress secondary electron emission from the collector. The collector was kept at ground potential. The beam collector and its grids are placed inside a metal cup which both shields them from external charged particles and also acts as a gas cap over the rear end of the scattering cell. The beam collector assembly is mounted on a rod which allows the assembly to be pulled away from the rear of the scattering cell and then swung out of the path of the incident ion beam. This is done to allow alignment of the entire apparatus along the magnet axis and to allow the incident ion beam to fall directly on the detector for calibration purposes.

6. SCATTERED ION DETECTOR

The differential scattering cross sections to be measured are extremely small, and therefore it will be necessary to use some sort of amplification so that the scattered particle current can be measured on an ammeter. A Model 306 Magnetic Electron Multiplier manufactured by Bendix Corporation, Cincinnati, Ohio, was chosen as the beam detector and amplifier. This multiplier, developed by Goodrich and Wiley[14], could provide reproducible current gains up to 10^6, sufficient for the projected measurements.

The multiplier, shown schematically in Figure 19, consists of two plane parallel glass surfaces each 5.5 centimeters long and placed 0.5 centimeters apart. The glass strips are coated on their facing sides with a thin, high resistance (approximately 10^8 ohms) layer of tin oxide and antimony. Attached to the top of the field strip is an entrance grid of etched nickel mesh, 1.9 centimeters wide and 1.2 centimeters high, with greater than 90% transparency. Attached to the top of the dynode strip and directly behind the entrance grid is a tungsten cathode 2.54 centimeters long. Permanent Alnico V magnets placed outside both the field strip and the dynode strip produced a uniform magnetic field of 400 to 600 gauss in the space between the strips. This magnetic field is oriented perpendicular to the long dimension of the strips and parallel to their faces. At the bottom of the strips and between them a stainless steel anode is located. The entire structure is quite rugged and easy to handle. Its outside dimensions are 10.2 centimeters high, 3.35 centimeters long, and 2.06 centimeters deep.

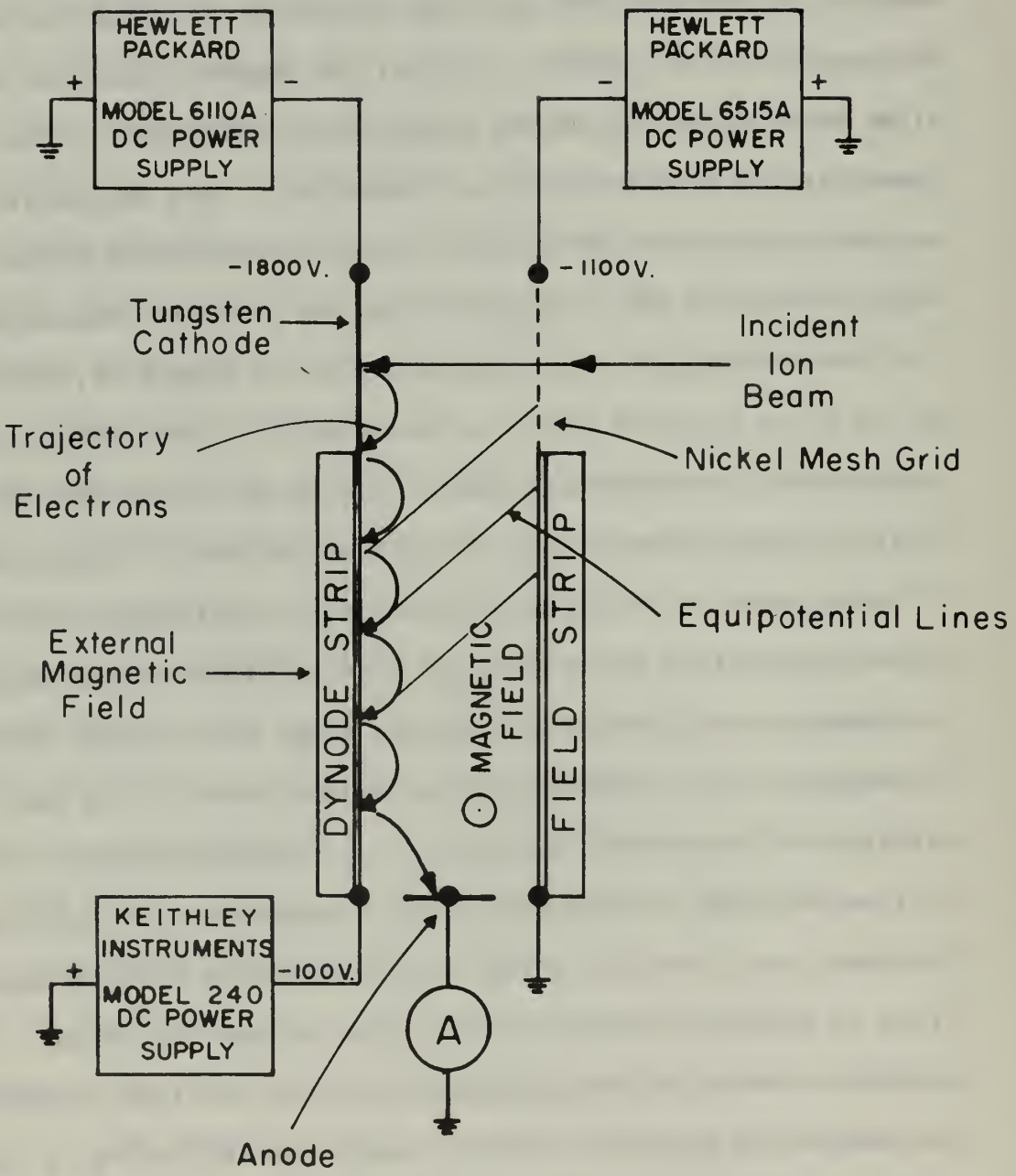


Figure 19. Operational Schematic of the Bendix Model 306 Magnetic Electron Multiplier.

In the multiplier's normal mode of operation a potential difference is applied the length of each strip in such a way that the end of the strips nearest the anode is the more positive end, and so that the field strip is positive with respect to the dynode strip. This arrangement, along with the magnetic field of the permanent magnets, produces crossed electric and magnetic fields in the region between the two surfaces. In this field configuration the motion of any electron released from rest at any point on the dynode strip is a cycloidal motion in an $\vec{E} \times \vec{B}$ direction (down the long dimension of the strip). Because the equipotential lines are slanted with respect to the dynode strip surface the electron strikes the surface before the completion of the first cycle. For sufficiently high applied potentials the electron has enough energy to cause secondary emission with a secondary emission ratio greater than unity. The secondary electrons thus generated repeat the process of the original electron, until most all electrons reach the anode and are collected. Therefore any current incident on the tungsten cathode is read out on the ammeter connected to the anode multiplied by some measurable gain.

As the scattered ion detector in the experimental apparatus, the multiplier has to be operated in a magnetic field of up to 200 gauss. The effect of this magnetic field causes the secondary electrons of the multiplier to drift perpendicular to the long axis of the dynode strip. Thus some of these electrons drift off the side of the dynode strip and never reach the anode, thereby reducing the gain of the multiplier. The rate of drift increases with increase in the magnetic field, causing the multiplier gain

to decrease with increasing field. Shielding the multiplier from the external field was attempted using μ-metal, netic, and conetic foils. This proved unsatisfactory for two reasons. First, the large amount of shielding material required so disturbed the focusing field that scattered particle trajectories were not predictable. Second, the gain of the multiplier could not be reproduced whenever the focusing field was changed and then returned to the original value. This was probably due to the hysteresis in the shielding material. The most satisfactory system has been to operate the multiplier inside an aluminum shield to protect it from random background and to choose the various strip potentials which give the highest gain and lowest noise. For a particular set of potentials the multiplier gain was measured at different focusing magnetic field values. This was done by varying the magnet coil current and keeping the multiplier at a fixed distance from the magnet center and also by fixing the coil current and varying the distance of the multiplier from the magnet center. both methods gave essentially the same gain for equal values of the axial magnetic field. A plot of these measurements and a $10^{\underline{th}}$ order fit of the data points is shown in Figure 20. The fitted value was used in the actual calculation of cross sections. An actual gain measurement is made as follows: with the multiplier installed inside the apparatus, the focusing magnet current and the detector distance are established at their desired values. Then the field strip and the anode of the multiplier are grounded while the cathode is connected to an ammeter. The ion beam from the source is directed onto the cathode. This current (which has to

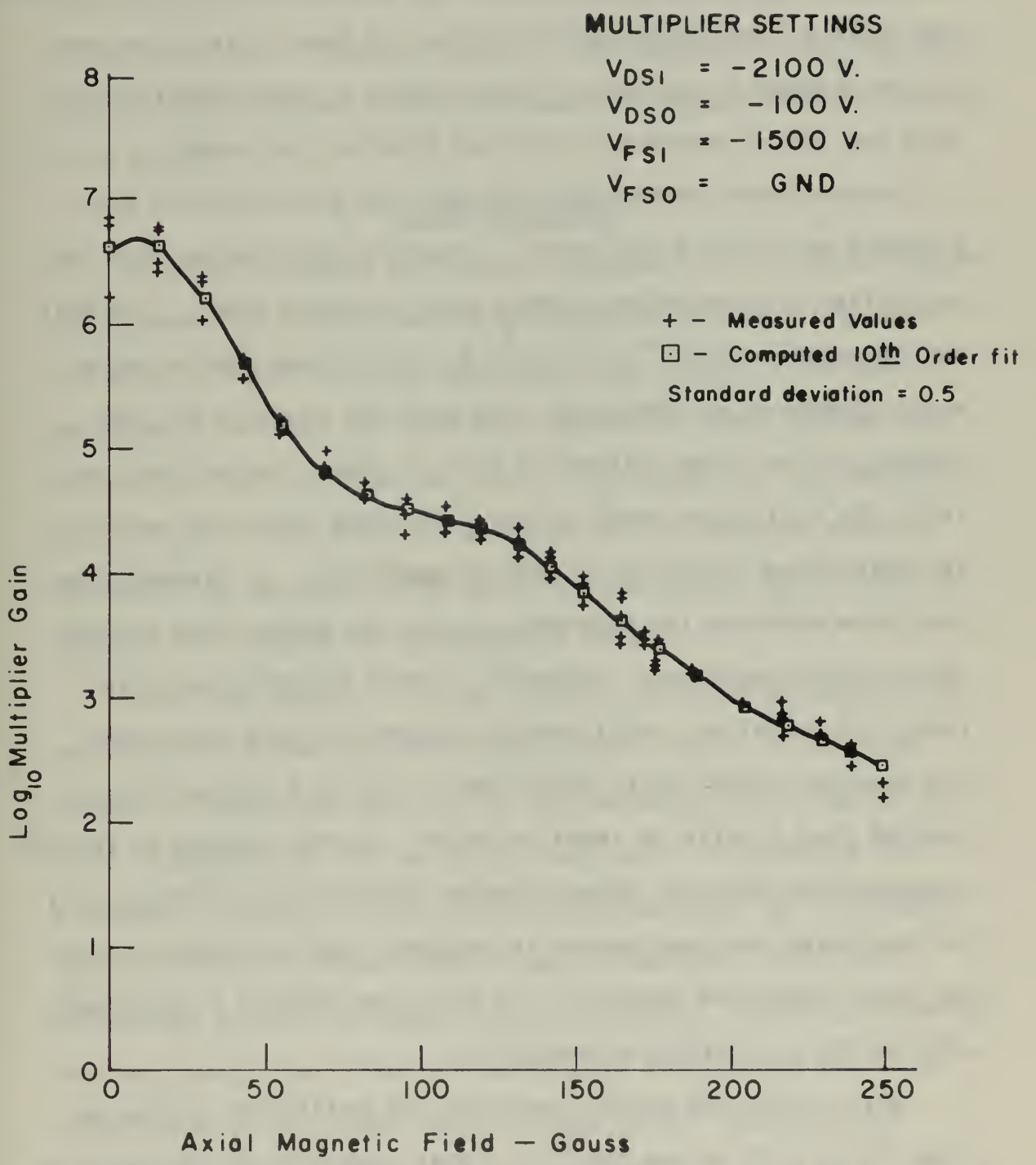


Figure 20. Log_{10} Multiplier Gain vs Axial Magnetic Field Strength.

be kept below 10^{-11} amps to prevent saturation of the multiplier output) is then measured. Then, without changing the current incident on the multiplier cathode the multiplier is placed in its normal operating condition and the anode current is determined. The ratio of the anode current to the ion beam current measured at the cathode is the gain. This process is then repeated for each new set of magnet currents and detector distances.

Measurements showed that the gain did not vary with gas pressure up to 2.0×10^{-4} Torr, a pressure much higher than the multiplier ever encountered when data was being taken. The gain was measured using Li^6, Li^7, He^4, H_2, and H ions and no ion or mass dependence was detected. The gain was found to be independent of the anode current up to 10^{-5} amps. Above these currents the multiplier tends to saturate since the anode current is approaching the strip current in magnitude. To prevent slow ions from entering the detector, a grid was placed over the detector shield aperture. Normally, a small positive potential (about 20 volts) was sufficient to screen out this background. The detector signal falls about 50% as the grid voltage is increased from 0 volts to about 10 volts. As the voltage is further increased, the detector signal remains essentially constant until the scattered ion beam energy is reached, then the detector signal again decreases sharply. The grid also permits a crude analysis of the scattered ion energy.

After about two months operation the multiplier strips became coated with vacuum pump oil. This caused large increases in the multiplier noise resulting in false current measurements.

Cleaning the strips with a pencil eraser to remove the deposits reduced the noise and did not effect the multiplier gain.

Subject to the limitations outlined above the magnetic electron multiplier proved to be a reliable detector for the scattering apparatus. Although initial measurements of the gain were tedious, once they were made, subsequent checking showed the gain to be stable.

7. SYSTEM ALIGNMENT

In order to detect particles scattered at a particular angle the detector must be placed on the focusing magnetic field axis at the point where the scattered particles focus on the axis. The program for calculating the intercept distance assumes that scattering took place on the axis at the center of the focusing magnet field. Therefore the accuracy of the angle of scatter determination depends on how well the scattering center and the detector are aligned to the magnetic field.

Since the geometric centerline of the focusing magnet coil was found to be the magnetic field axis to within 0.1%, this geometric centerline was used as the reference for aligning all other components to the magnetic field axis. To perform the alignment, crosshairs were placed on either side of the magnet spool to mark its axis. Then a small laboratory laser was positioned so that its beam lay on the magnet axis established by the two crosshairs. The crosshairs were removed and the line established by the laser beam was used as the reference for aligning all other components to the focusing magnet axis. This

method made possible the aligning of the scattering cell, the detector, and the focusing lenses to the magnetic field axis to an accuracy of 1.0 milimeter radical displacement off the axis. Analysis of computed trajectories showed this error to be essentially undetectable.

The incident ion beam was aligned by adjusting the position of the source and the mass analyser with the ion beam on until the maximum possible beam reached the scattering cell beam collector using no deflector voltages.

CHAPTER IV

EXPERIMENTAL RESULTS

1. PRELIMINARY TESTS

The differential scattering cross section shown in equation (1) of Chapter I can be rewritten in terms of the quantities actually measured as follows:

$$d\sigma(\theta) = \frac{I_D/G}{I_i(P_{sc}\rho)t\, d\Omega} \quad cm^2 \qquad (1)$$

where
- I_D = current at MEM detector anode in amps
- G = MEM detector gain
- I_i = incident ion beam current in amps
- P_{sc} = pressure of target gas in Torr
- ρ = 3.536×10^{16} particles/cm^3-Torr
- t = target length in cm
- $d\Omega$ = solid angle

To measure a cross section, then, a target gas pressure and a target length are established in the system. The magnet current and/or the detector distance are varied to cover the range of scattering angles to be observed. These two quantities also determine the value of the multiplier gain and, along with the angle of scatter, the solid angle. Then at each setting of the magnet current and the detector distance, I_D and I_i are observed. These values are used to calculate $d\sigma(\theta)$ using the appropriate computer program listed in Appendix IV.

In order to eliminate any spurious signals a series of measurements was undertaken to test the effect of the variables I_i, P_{sc} and t upon the measured value of $d\sigma$. For a particular angle of scatter

$$d\sigma = K \frac{I_D}{I_i P_{sc} t}, \text{ where } K = \text{constant.}$$

Now for constant incident ion beam current, I_i, and constant target length, t,

$$I_D = \left(\frac{d\sigma}{C_1}\right) P_{sc}. \tag{2}$$

The experimental data plotted in Figure 21 verify this linear relation. Notice that the data are linear but does not extrapolate to zero. The fact that I_D does not go to zero is probably due to multiplier background noise. However this error is not important above 1.0×10^{-3} Torr pressure where the measurements were usually made. Another linear relationship which must exist is

$$I_D = \left(\frac{d\sigma}{C_2}\right) I_i \tag{3}$$

for constant target pressure and target thickness. Figure 22 shows a plot of one set of experimental data which demonstrates this characteristic. Finally, if the incident ion beam current and the target pressure are kept constant then the detector current must vary linearly with the target thickness. This relation, which is

$$I_D = \left(\frac{d\sigma}{C_3}\right) I_i \tag{4}$$

is shown experimentally in Figure 23. These three curves show that our detector signal has the proper dependence on the various parameters and behaves like a scattered particle current. For the differential scattering cross sections measured the ion current at the beam collector was about 10^{-7} amps, the current to the rear of the scattering cell was about 10^{-9} amps, the ion current on the

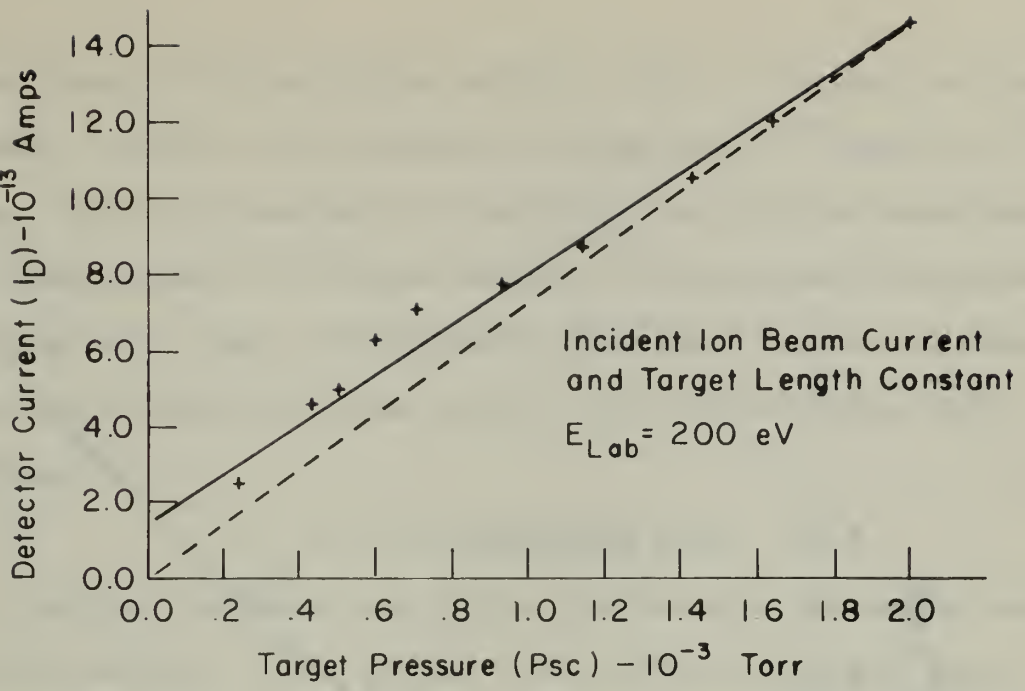


Figure 21. Detector Current vs Target Pressure for $^{6}Li^{+}$ on He at 40.42°.

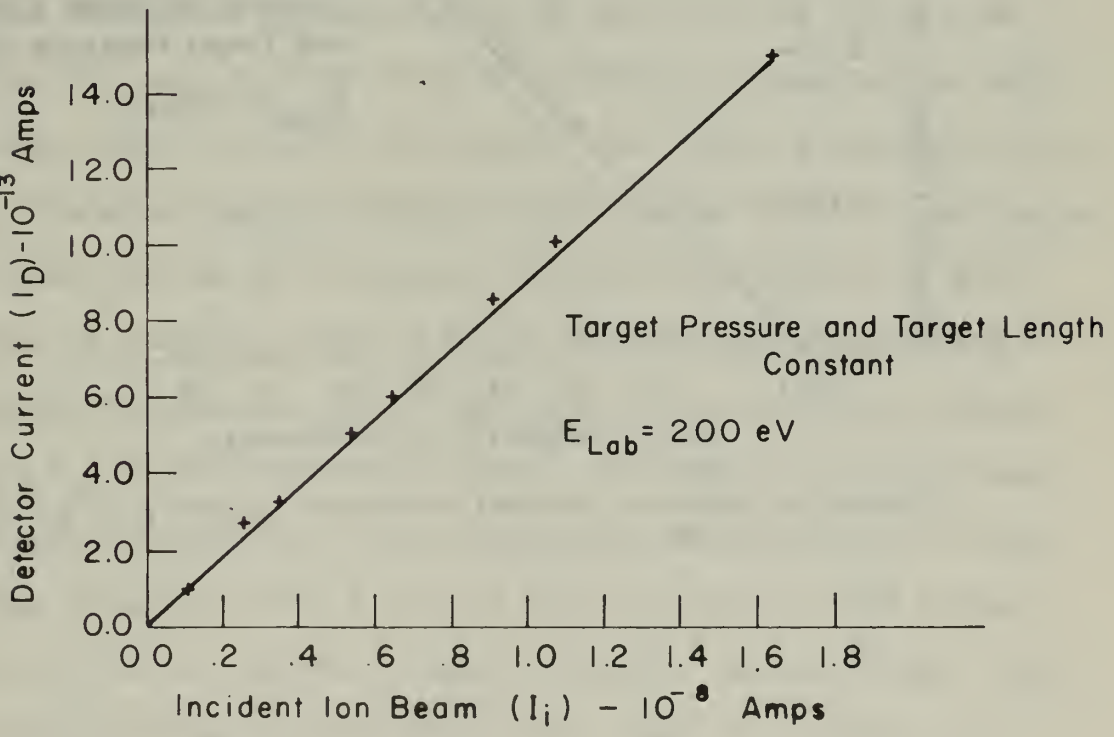


Figure 22. Detector Current vs Ion Current for $^{6}Li^{+}$ on He at 40.96°.

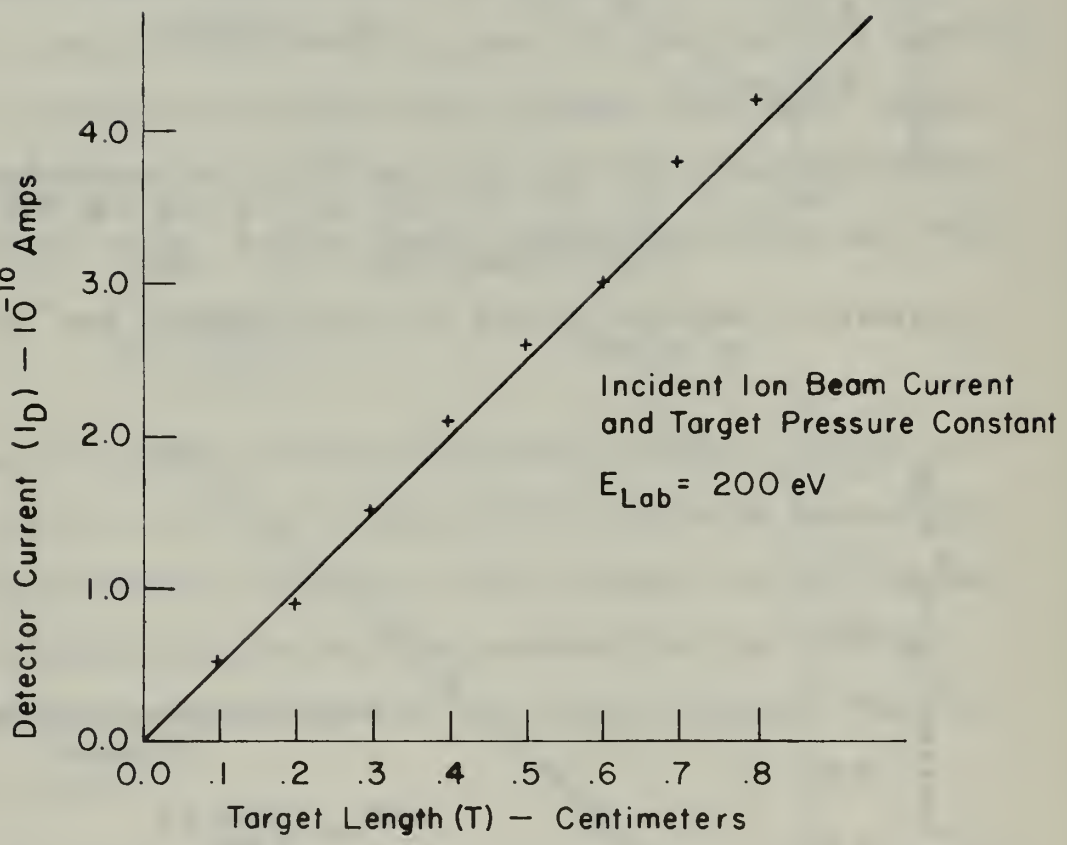


Figure 23. Detector Current vs Target Length for $^{6}Li^{+}$ on He at 39.1°.

front face of the scattering cell was about 10^{-8} amps, and the detector signal of the MEM output varied from 10^{-8} amps to 10^{-13} amps. With no target gas in the scattering cell and essentially the same current to the beam collector the detector current drops to about 10^{-15} amps. Consequently the signal due to scattered ions was at least 100 times greater than the multiplier dark current.

2. He^+ + He SCATTERING DATA

Another important test of our technique is the comparison of data measured by our method to data obtained by more conventional methods. We therefore measured the elastic differential scattering cross sections for He^+ on He at 300 eV from 40° to 52° and at 400 eV from 42° to 54°, and compared our data to that taken by Lorents and Aberth[1], as shown in Figures 24 and 25. The gross shape of our data and Lorents' data is essentially the same, but we do not observe the fine structure in as much detail as they do. This is due to two effects, both tending to increase the angular resolution ($\Delta\theta \cong 1^\circ$ for our data, compared to $\Delta\theta \cong 0.5^\circ$ for the Lorents data). One effect is the increase in angular spread that occurs because of the anomalously large energy spread of about 8.0 eV in the incident ion beam energy. The other effect is the increase in angular spread brought about by the spiraling of the incident ions about the magnetic axis. This spiraling will allow the incident ions to enter the target area at small angles with respect to the system axis, thereby increasing the angular spread the detector sees. Nevertheless these results do show that our technique can give reliable cross section measurements on an absolute basis.

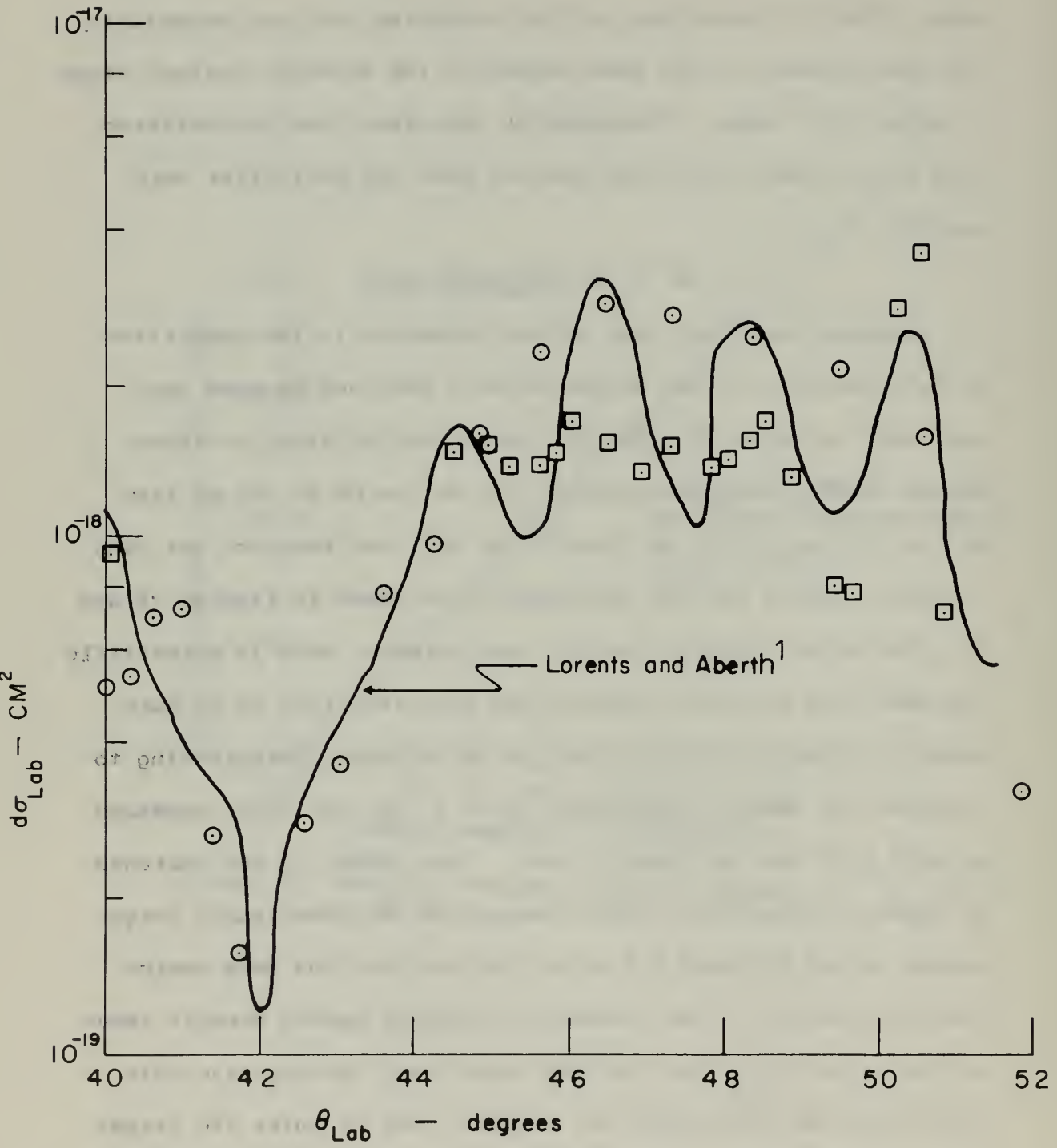


Figure 24. $d\sigma(\theta)_{lab}$ vs θ_{lab} for He^+ on He, E_{lab} = 300 eV

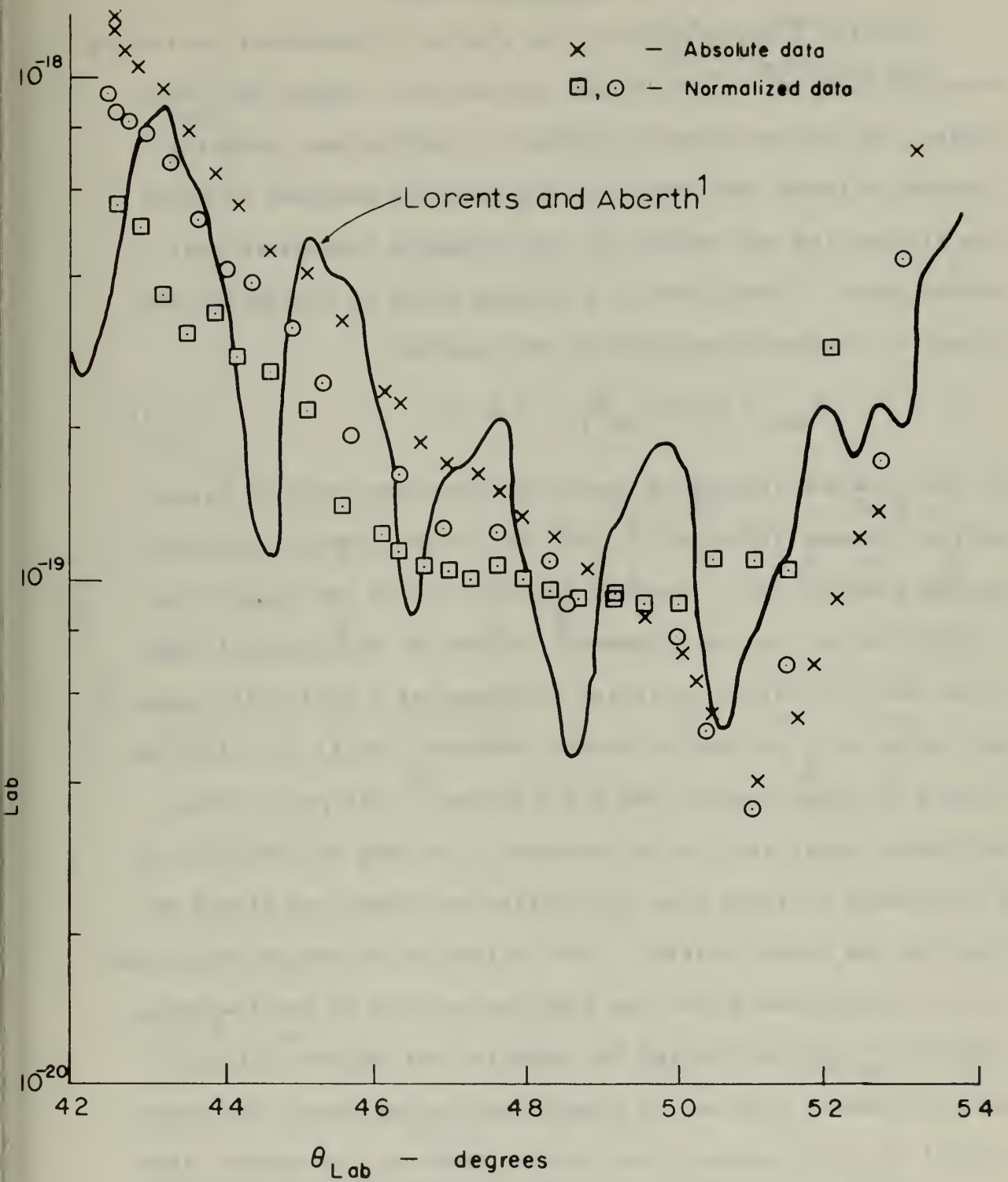


Figure 25. $d\sigma(\Theta)_{lab}$ vs Θ_{lab} for He^+ on He, E_{lab} = 400 eV.

3. Li^+ + He SCATTERING DATA

Finally, a measurement of the elastic differential scattering cross section of $^6Li^+$ on He was carried out. Since, for this system, the helium target atoms have a smaller mass than the incident lithium ions there are two possible energies at which the lithium ion may scatter at any allowable laboratory scattering angle. There also is a maximum angle of scatter in the laboratory system determined by the relation

$$\theta_{max} = \sin (M_{He}/M_{Li}) = 41.7^{o} \qquad (5)$$

At this maximum scattering angle the laboratory elastic cross section becomes infinite[15]. This particular property made this system suitable for a check of the accuracy of our angular determination and system alignment. Since our experimental apparatus does not detect particles scattered at a particular angle, but rather at a particular vector momentum (recall that the trajectory is determined by the $\vec{p} \times \vec{B}$ forces), this peak in the laboratory cross section can be seen by setting the detector at a convenient distance from the scattering center and slowly decreasing the magnet current. This allows us to measure the cross sections continuously from the high energy side to the low energy side of θ_{max} without moving the detector out of the scattered particle beam. Thus we are able to determine closely the magnet current for the largest cross section observed and compare that magnet current value with current value for θ_{max} calculated from the theoretical trajectories. The results of these measurements are shown in Figures 26 and 27 which are plots of the laboratory

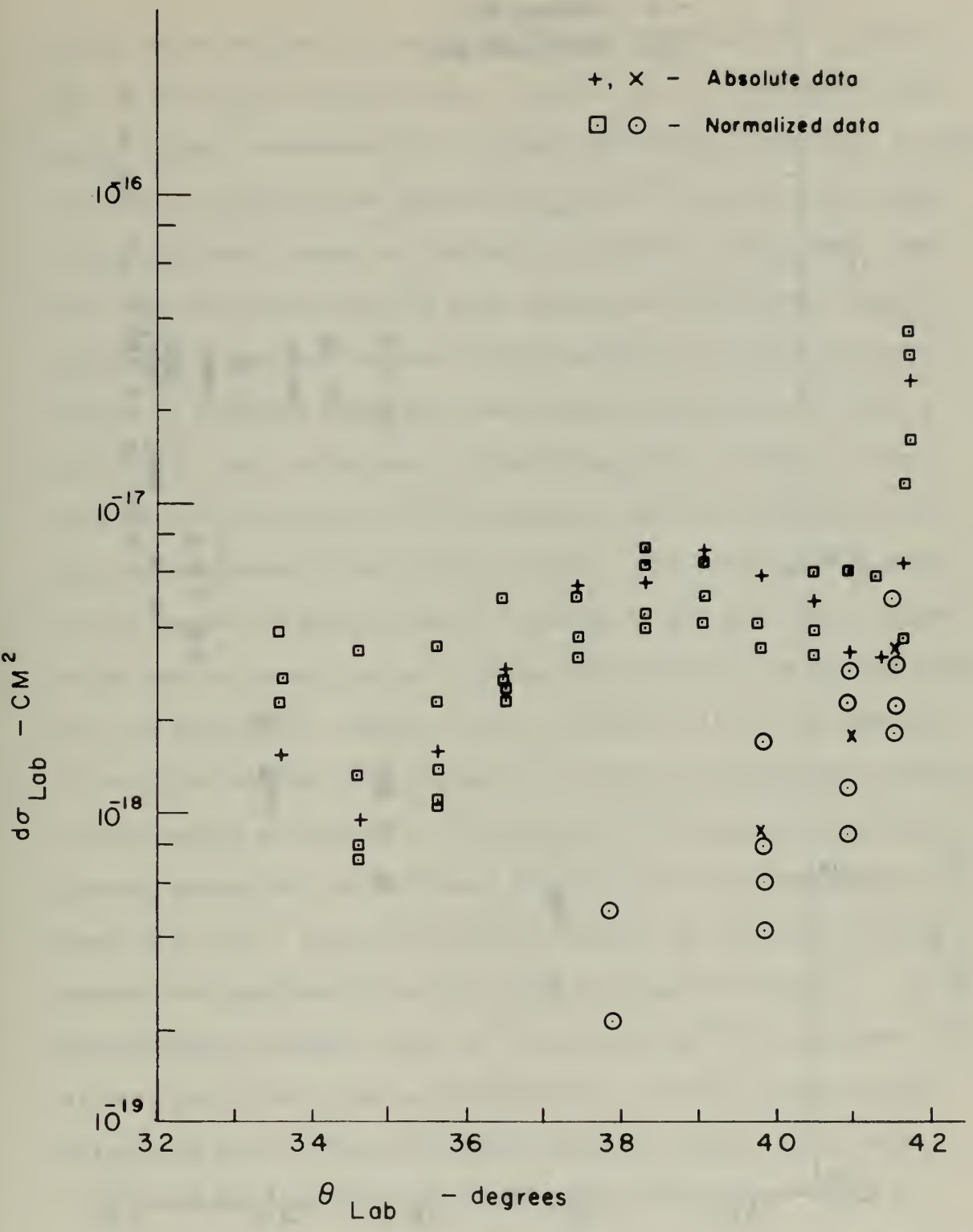


Figure 26. $d\sigma(\theta)_{lab}$ vs θ_{lab} for $^{6}Li^{+}$ on He, E_{lab} = 200 eV.

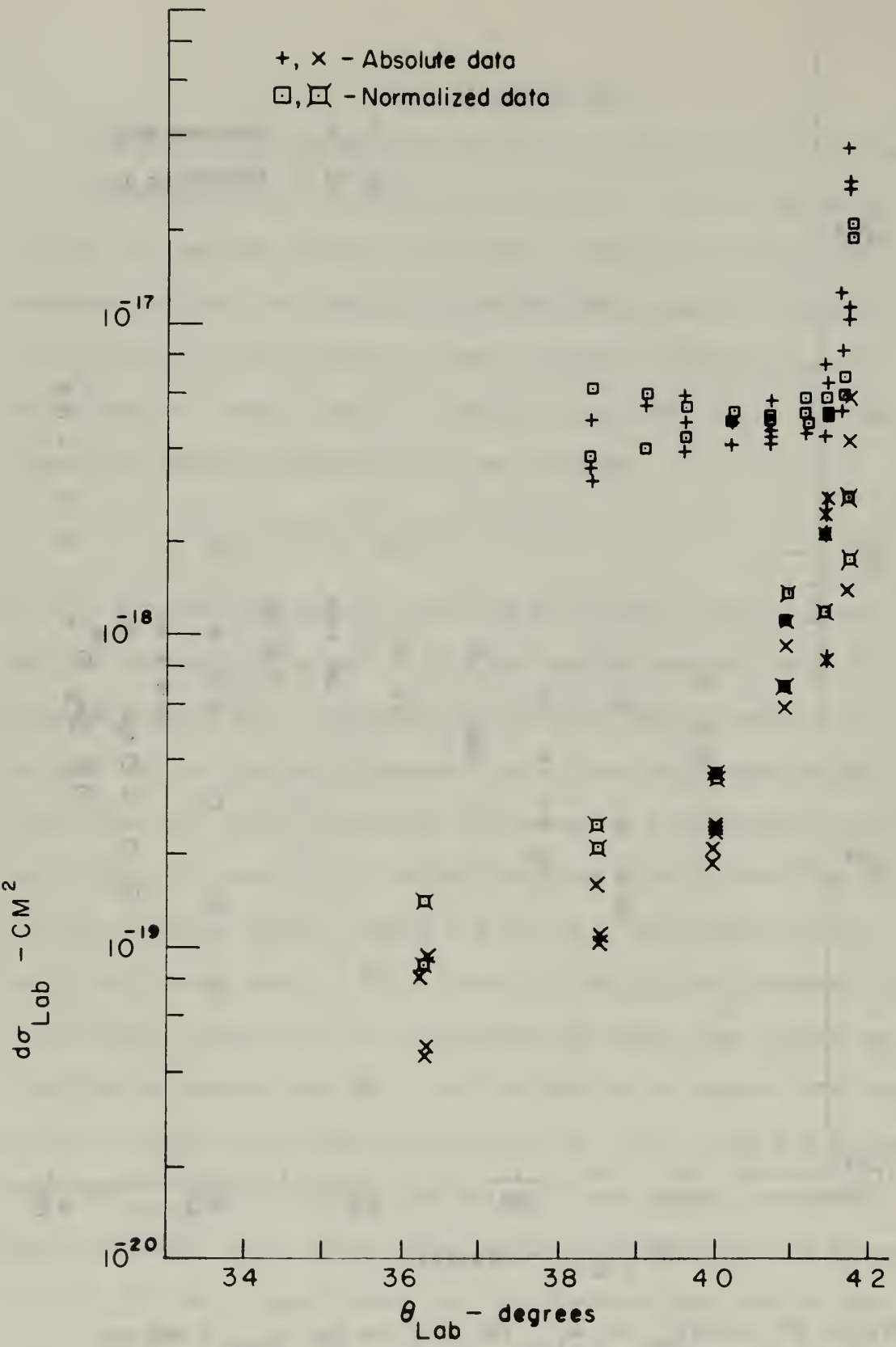


Figure 27. $d\sigma(\theta)_{lab}$ vs θ_{lab} for $^{6}Li^{+}$ on He, E_{lab} = 300 eV.

differential scattering cross section vs the angle of scatter at 200 eV and 300 eV respectively. Notice that in both cases the upper branch, corresponding to higher scattering energies, suddenly increases sharply as we approach $\theta_{max}(41.7^{o})$ and then decreases along the lower branch as the angle of scatter decreases. The fact that the cross section peak appears at the correct angle illustrates that our angular determination is correct and our system is properly aligned. The spread in the data is about a factor of 2 and is believed to be largely due to error in the multiplication factor G of the magnetic electron multiplier and will be discussed in more detail below. The same data is shown in the center of mass system in Figures 28 and 29. There appears to be some structure in both curves most easily seen in the smooth data in Figure 30. However, from this data, it is not possible to conclude whether this structure is due to instrumental effects or represents an oscillation in the cross section produced by quantum mechanical interference effects. For the homonuclear case (e.g. He^{+} + He) oscillations produced by the interference of gerade and ungerade states has been thoroughly studied[16]. In heteronuclear systems (e.g. Li^{+} + He) Lichten[17] has proposed that at very small internuclear separations a similar interference effect may occur since the active electron might find itself in a field resembling that of a homonuclear molecule. This, of course, would cause structure in the differential scattering cross section. On the other hand, there are reasons to believe that instrument effects cause the oscillations. In the 80 eV data, the large dip in the cross section at 95^{o} may be due to interaction

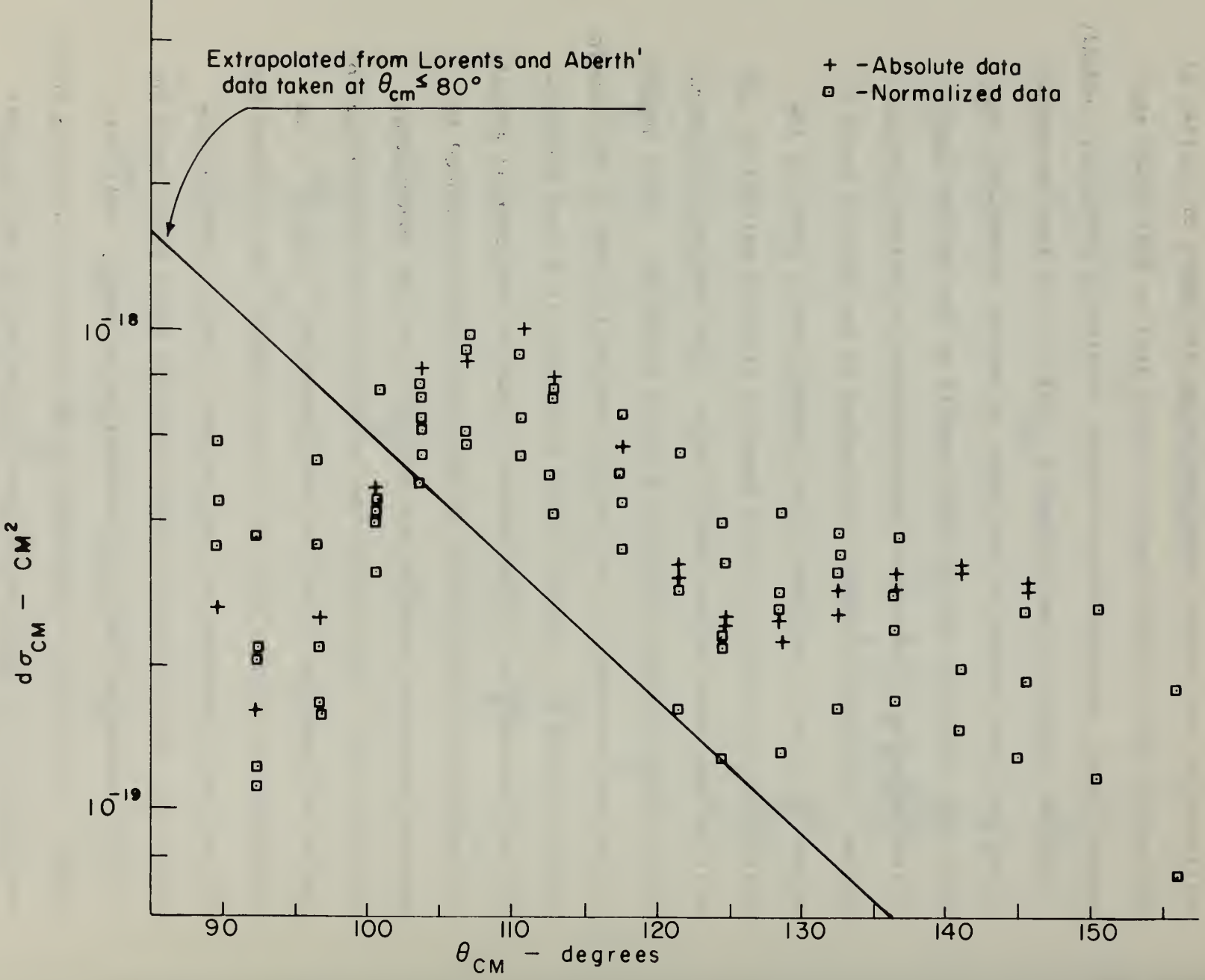


Figure 28. $d\sigma(\theta)_{cm}$ vs θ_{cm} for $^{6}Li^{+}$ on He, E_{cm} = 80.0 eV.

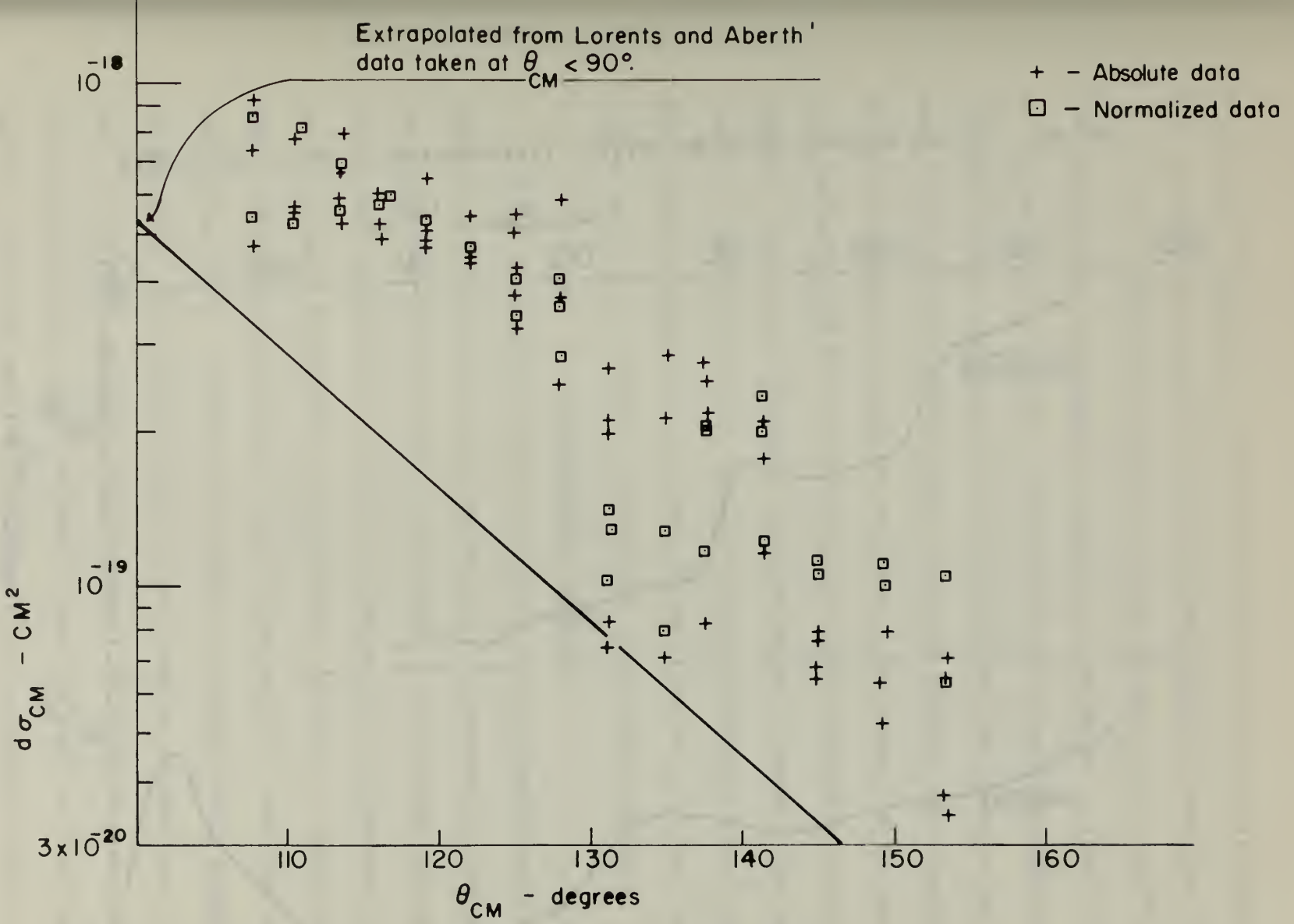


Figure 29. $d\sigma(\theta)_{cm}$ vs θ_{cm} for $^{6}Li^{+}$ on He, E_{cm} = 120.0 eV.

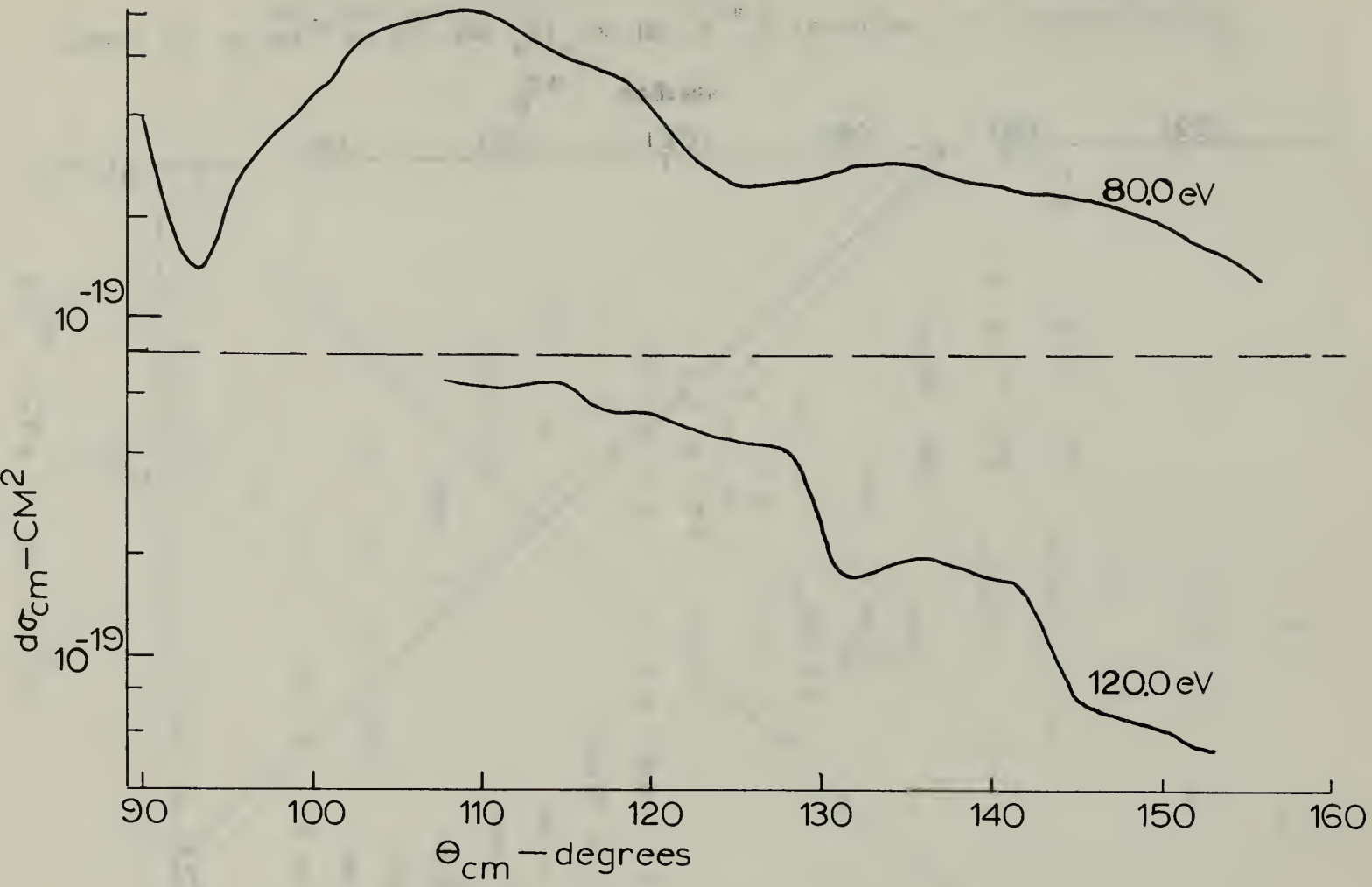


Figure 30. Elastic Differential Scattering Cross Section for $^{6}Li^{+}$ on He.

of the scattered particle beam with the scattering cell exit slit. This problem can occur for particles scattered at less than 36^{o} in the lab. The dips at 125^{o} in the 80 eV data and at 130^{o} in the 120 eV data correspond to particles scattered at about 41.7^{o} in the laboratory system. Consequently it is possible that the dips are due to inaccuracy in the calculated solid angle very near the laboratory cutoff angle. Notice however that regardless of the structure our data has slightly less slope and is above the line extrapolated from data taken at smaller angles by Lorents and Aberth[2]. Our data indicates that the center of mass cross section tends to level out as the center of mass scattering angle increases. Thus there is essential agreement between our data at the larger angles and that of Lorents and Aberth at the lower angles.

4. EXPERIMENTAL ERRORS

There are several sources of error in the measurements. One source of error which cannot be entirely eliminated arises from the spiraling of the incident ions about the focusing magnet axis. As already pointed out in Section 2 above this introduces an error in the angular measurement, and is most important in measurements where the cross section has large variations as a function of the scattering angle. However, the effect is minimized by proper alignment of the incident beam to the focusing magnet axis. The gain of the MEM, which is the scattered ion detector, is a rather sensitive function of the magnetic field strength of the focusing magnet. Thus any small error in setting the magnet current or the detector distance would result in actual gains slightly different from those used in the cross section calculations. The error in

setting the detector distance and the magnet current would also cause differences between the actually observed angle of scatter and solid angle and their expected values from which the cross sections are calculated. The detector distance can be set to $\pm$ 1 mm and the magnet current can be regulated to $\pm$ 0.05 amp. For the $^{6}Li^{+}$ on He data this results in a possible error in the scattered angle of less than 0.05^{o} and in the solid angle of less than 5%. Another source of error is in the measurement of the target gas pressure in the scattering cell. Although an accurate determination of this error was not possible it is apparent from the scattering cell geometry that the actual pressure is higher than the measured pressure used in the cross section calculation. It is felt that the primary source of scatter in our data is due to the multiplier which had to be operated at potentials different from the recommended values in order to obtain high gain in the magnetic field. An analysis of the cross sections for $^{6}Li^{+}$ on He give a precision which is on the order of $\pm$ 20% of the average value of a set of measurements.

CHAPTER V

CALCULATION OF THE INTERATOMIC POTENTIAL OF THE Li^+ - He SYSTEM

1. INTRODUCTION

The estimation of the interaction energy between two atoms as a function of their separation distance is of primary importance in the understanding of numerous chemical and physical problems. The interaction energy can be found in several ways; however the most direct method is to calculate it from elastic scattering cross sections. In this chapter the potential function for Li^+ on He was calculated from the cross sections measured by our technique and some data taken by Aberth and Lorents[2]. The procedure used to calculate the potential function is based on Firsov's[3] method (outlined by Lane and Everhart[18]) using Gauss-Mehler quaduatures to perform the necessary integration. The potential function was then fitted to a Born-Mayer form and compared to the potential function calculated by Zehr and Berry[19] from their experimental data.

2. THEORY

Classical scattering theory, valid for this calculation[11], relates the potential function, V(r), to the center of mass angle of scatter, Θ, and the impact parameter, b, by the expression

$$\Theta(E,b) = \pi - 2\int_{r_o}^{\infty} \frac{b}{r}\left[\left(1-\frac{V(r)}{E}\right)r^2 - b^2\right]^{-\frac{1}{2}} dr \qquad (1)$$

where E is the center of mass energy,
r is the separation distance, and
r_o is the distance of closest approach.

The necessary and sufficient conditions for scattering particles into the element of solid angle $d\Omega_{cm} = 2\pi \sin\theta \, d\theta$ is that the particles be incident in the annular ring of area $2\pi b \, db$. Therefore the cross section $\sigma(\theta)$ is related to b and θ by

$$2\pi\sigma(\theta) \sin\theta \, d\theta = - 2\pi b \, db$$

or

$$b^2 = 2\int_{\theta}^{\pi} \sigma(\theta) \sin\theta \, d\theta. \qquad (2)$$

Since the functional form of $\sigma(\theta)$ isn't known the integration cannot be carried out. However b can easily be found from a plot of $\sigma(\theta) \sin\theta$ vs θ. The area under the curve from π to θ is then $b^2/2$. Thus the relation between θ and b can be obtained directly from the scattering data. However equation (1) cannot be used to obtain V(r) directly, so the following method will be used to determine the potential function from the $\theta = f(b)$ result. Let

$$q^2 = \left[1 - \frac{V(r)}{E}\right] r^2$$

or

$$V(r) = \left[1 - q^2/r^2\right] E \qquad (3)$$

and by knowing q and r, V(r) is determined. Making this substitution in (1) gives

$$\theta = \pi - \int_{b}^{\infty} 2b \left[\left(\frac{dr}{r}\right)/dq\right] \left[q^2 - b^2\right]^{-\frac{1}{2}} dq$$

$$= \pi - \int_{b}^{\infty} 2b \, (d \ln r/dq)(q^2 - b^2)^{-\frac{1}{2}} \, dq \, .$$

Now using the fact that

$$\pi = \int_b^\infty b(d\ell n\ q^2/dq)(q^2-b^2)^{-\frac{1}{2}}\ dq$$

leads to

$$\Theta(b) = b\int_b^\infty [d\ell n(q_1^2/r^2)/dq_1][q_1^2 - b^2]^{-\frac{1}{2}}\ dq_1$$

where the integration variable has been changed to q_1. Now multiply through by $db/(b^2-q^2)^{\frac{1}{2}}$ and integrate from q to infinity. Thus

$$\int_q^\infty \frac{\Theta(b)db}{(b^2-q^2)^{\frac{1}{2}}} = \int_q^\infty bdb \int_b^\infty \frac{[d\ell n(q_1^2/r^2)/dq_1]\ dq_1}{(b^2-q^2)^{\frac{1}{2}}(q_1^2-b^2)^{\frac{1}{2}}} . \qquad (4)$$

The integral on the right can be transformed using Dirchlet's formula[20] to give

$$\int_q^\infty \frac{\Theta(b)db}{(b^2-q^2)^{\frac{1}{2}}} = \frac{1}{2}\int_{q^2}^\infty \frac{d(q_1^2)}{2q_1}\ d\ell n(\frac{q_1^2}{r^2})dq_1 \int_{q^2}^{q_1^2} \frac{d(b^2)}{(b^2-q^2)^{\frac{1}{2}}(q_1^2-b^2)^{\frac{1}{2}}} .$$

The right hand integral can be placed in a standard form and integrated to give π. Thus equation (4) becomes

$$\int_q^\infty \frac{\Theta(b)db}{(b^2-q^2)^{\frac{1}{2}}} = \frac{\pi}{2}\int_{q^2}^\infty \frac{d(q_1^2)}{2q_1}\ d\ell n(q_1^2/r^2)dq_1 = \frac{\pi}{2}\ \ell n\ r^2/q^2 .$$

Thus

$$r(q) = q\ \exp\left[\frac{1}{\pi}\int_q^\infty \frac{\Theta(b)db}{(b^2-q^2)^{\frac{1}{2}}}\right] \qquad (5)$$

and by evaluating this equation and using the results in equation (3) one can obtain V(r). The evaluation of the integral in equation (5) is done using Gauss-Mehler quadratures[21], where

$$\int_0^1 f(y)(1-y^2)^{-\frac{1}{2}}\,dy = \frac{\pi}{n}\sum_{j=1}^{n/2} f(\cos\frac{2j-1}{2n}\pi)$$

and n = even integer. For our case let y = q/b, then

$$\int_q^\infty \frac{\Theta(b)db}{(b^2-q^2)^{\frac{1}{2}}} = \int_0^1 \frac{\Theta(q/y)dy}{y(1-y^2)^{\frac{1}{2}}}$$

Thus

$$f(y) = \frac{\Theta(q/y)}{y}\ .$$

3. PROCEDURE

As an example of the procedure consider the calculation of V(r) from the data for $^6Li^+$ on He at 80.0 eV. The cross section is plotted in Figure 30. A linear fit of thisdata was used in the potential calculation. From this data a plot of $\sigma(\Theta)\sin\Theta$ is constructed. This plot is shown in Figure 31. The curve has to be extended to 180^o. The area under the curve from any Θ to 180^o is $b^2/2$. The result of this integration is plotted as $\Theta(b)$ vs b and is shown in Figure 32. From this graph r(q) is evaluated. A value of q is chosen and $\Theta(q/y)$ is found for each term of the Gauss-Mehler quadrature formula. Then the individual f(y) terms are found and the integral is evaluated. From this one obtains r(q) and finally V(r) using equation (3). The Gauss-Mehler quadratures give the same answer to four significant figures for n = 8,10, or 12. However we used n = 12 for all calculations.

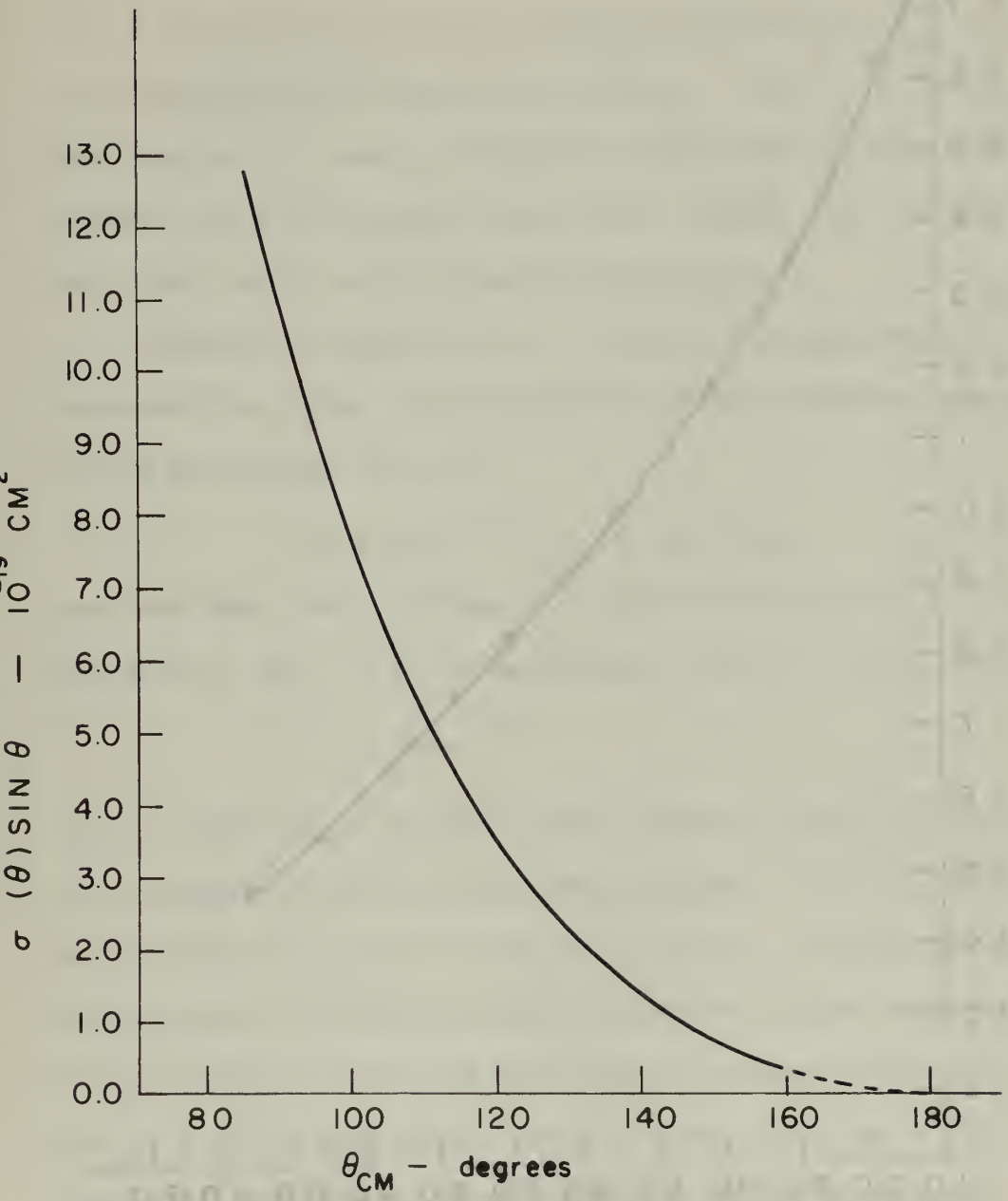


Figure 31. $\sigma(\theta)\sin\theta$ vs θ for $^{6}Li^{+}$ on He, E_{cm} = 80.0 eV.

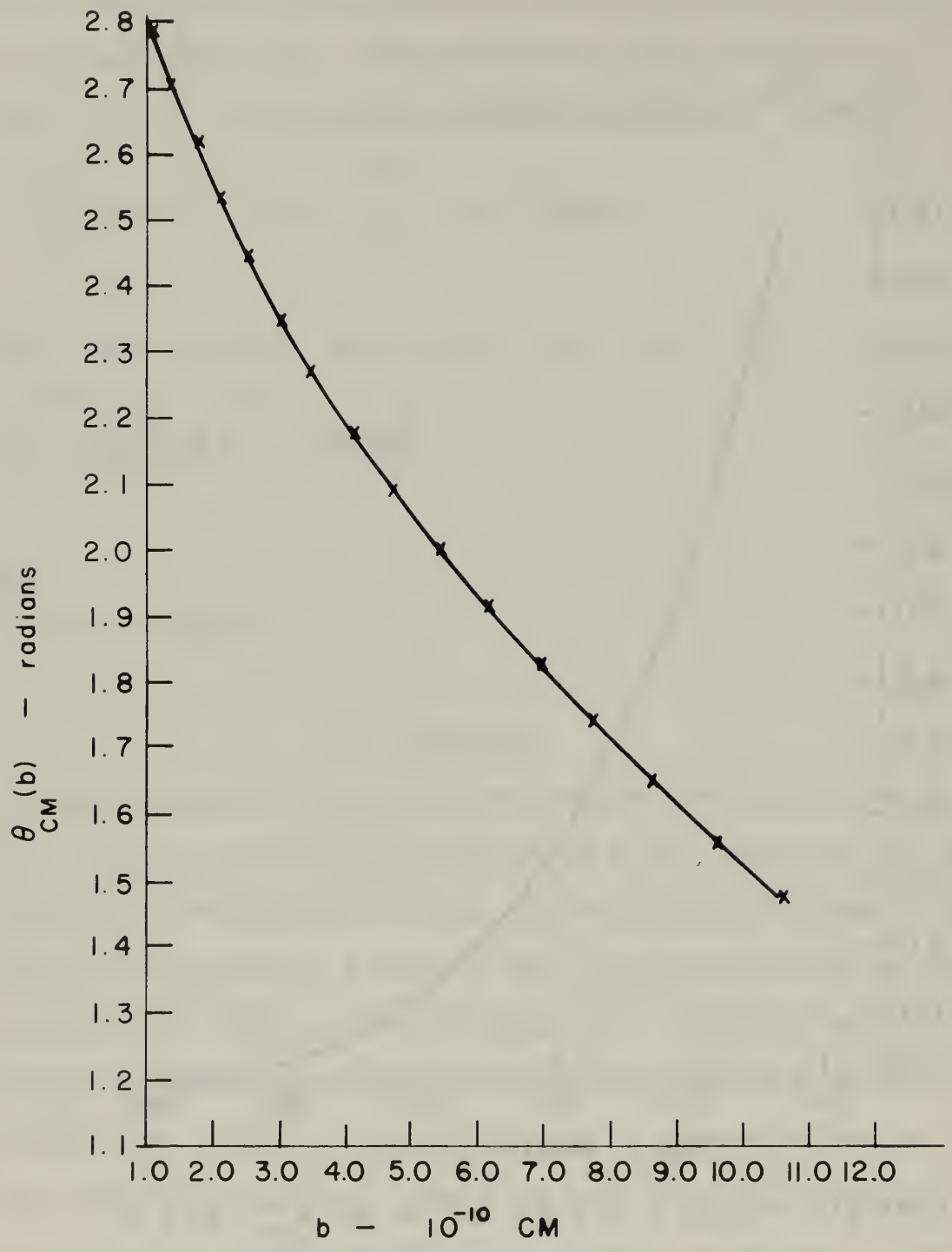


Figure 32. Θ(b) vs b for $^{6}Li^{+}$ on He, E_{cm} = 80.0 eV.

4. RESULTS

Using the procedure outlined above the potential function was calculated from our data at E_{cm} = 80.0 eV and E_{cm} = 120.0 eV and from Aberth and Lorents data at E_{cm} = 109.1 eV and E_{cm} = 72.7 eV. The results are shown in Figure 33 where the potential is plotted against the internuclear separation. Notice that our data fits quite well with that of Aberth and Lorents.

The plot of $\log_e V(r)$ vs r was found to approximate a straight line, thus the potential function could be represented by the Born-Mayer form as

$$V(r) = 259e^{-4.4r}, \quad r \text{ in } 10^{-8} \text{ cm.}$$

Zehr and Berry who also measured the scattering of $^7Li^+$ on He found their data to fit a Born-Mayer potential which is expressed as

$$V(r) = 370e^{-5.1r}$$

This is plotted on the same graph with our potential (Figure 33). The agreement is quite good down to about $r = 0.3 \times 10^{-8}$ cm, below which their curve rises more sharply. This discrepancy at small values of the internuclear distance is not surprising in view of the fact that the measurement by Zehr and Berry was carried out by a difference method which is more accurate at the smaller angles of scattering corresponding to larger internuclear distances. The agreement with the data of Lorents and Aberth appears to be excellent.

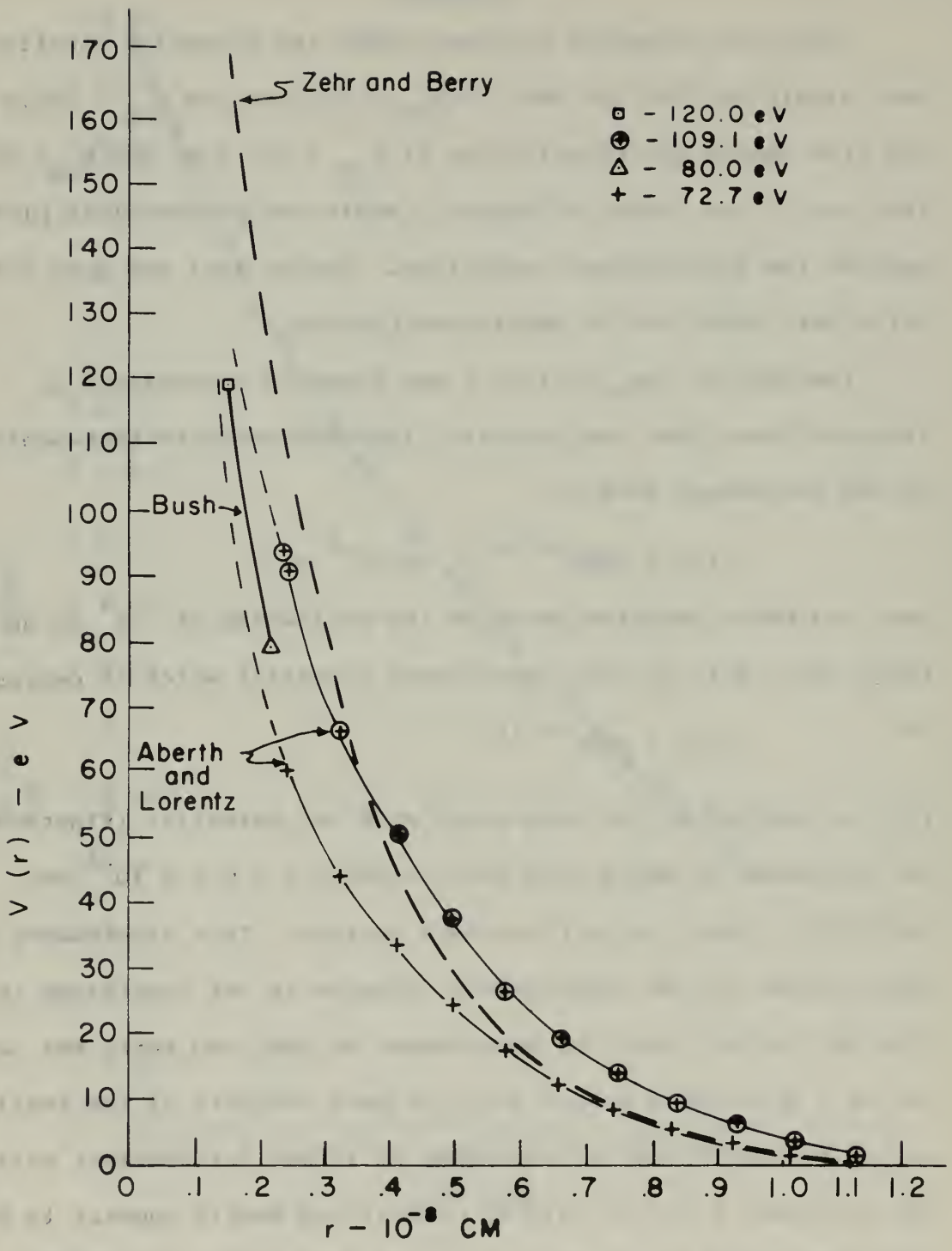


Figure 33. Interatomic Potential for Li^+ -He as a Function of Internuclear Separation.

CHAPTER VI

CONCLUSIONS

The most difficult and most time consuming portion of the work reported here was designing the apparatus and demonstrating the feasibility of using the focusing properties of an axially symmetric magnetic field to measure differential scattering cross sections. This was accomplished by showing that data taken by this method is in essential agreement with that measured by other means. Therefore this method with its much larger solid angle will allow future measurements of heretofore too-small-to-be-observed cross sections.

The second accomplishment of this research was the measurement of the differential scattering cross section of $^{6}Li^{+}$ on He at large angles, thereby extending the data about 80^{o} past previous measurements. These measurements also demonstrated the case in data collection that this technique (with its built in momentum analysis) offers for systems with heavy incident ions and lighter targets. Finally the interatomic potential function at distances less than 1Å for the Li^{+} on He system was calculated from our data. The agreement of this result with that derived from other scattering measurements is additional evidence for the soundness of our technique.

BIBLIOGRAPHY

1. Lorents, D.C., and Aberth, W., "Elastic Differential Scattering of He^+ Ions by He in the 20-600 eV Range," The Physical Review, 139, A1017 (1965).

2. Aberth, W., and Lorents, D.C., "Elastic Differential Scattering of Li^+ Ions by He, O_2 and N_2 in the 10 to 600 eV Range," 4th International Conference on the Physics of Electronic and Atomic Collisions (Science Bookcrafters, Inc., Hastings-on-Hudson, N.Y., 1965) p.269. Also private communications.

3. Firsov, O.B., Journal of Experimental and Theoretical Physics (USSR), 24, 279, (1953).

4. Siegbahn, K., Alpha-,Beta-, and Gamma-Ray Spectroscopy (North Holland Publishing Co., Amsterdam, 1966).

5. DuMond, J.W.M., "Conditions for Optimum Luminosity and Energy Resolution in an Axial β-Ray Spectrometer with Homogeneous Magnetic Field," The Review of Scientific Instruments, 20, 160 (1949), and Persico, E., "A Theory of Solenoid β-Ray Spectrometer," The Review of Scientific Instruments, 20, 191 (1949).

6. Busch, H., "Berchnung der Bahn von Kathodenstrahlen im axialsymmetrischen electromagnetischen Felde," Annalen Der Physik, 81, 974 (1926).

7. Kelly, P.J., "Analogue Measurement of Charged Particle Trajectories in an Inhomogeneous Magnetic Field," Unpublished Master's Thesis, Naval Postgraduate School, Monterey, California, 1965.

8. Verster, N.F., "Theory of a Magnetic Lens Type Beta Ray Spectrometer," Applied Scientific Research, B1, 363 (1950).

9. Keller, J.M., Koenigsberg, E., and Paskin, A., "Ring Focus in a Thin Magnetic Lens Beta-Ray Spectrometer," The Review of Scientific Instruments, 21, 713 (1950).

10. Gagliano, R.A., "Theoretical Trajectories of Charged Particles in an Inhomogeneous Magnetic Field," Unpublished Master's Thesis, Naval Postgraduate School, Monterey, California, 1966.

11. McDaniel, E.W., Collision Phenomena in Ionized Gases (New York: John Wiley and Sons, Inc., 1964).

12. Heinz, O., and Reaves, R.T., "Lithium Ion Emitter for Low Energy Beam Experiments," Review of Scientific Instruments, 39, 1229 (1968).

13. Strohsahl, G.H., Jr., "Construction and Calibration of a Mass Spectrometer for the Analysis of Light Ions." Unpublished Master's Thesis, Naval Postgraduate School, Monterey, California, 1967.

14. Goodrich, G.W., and Wiley, W.C., "Resistance Strip Magnetic Electron Multiplier," Review of Scientific Instruments, 32, 846 (1961).

15. Schiff, L.I., Quantum Mechanics (McGraw-Hill Book Co., Inc., New York, 1955), 2nd Ed.

16. Marchi, R.P., and Smith, F.T., "Theory of Elastic Differential Scattering in Low-Energy He^+ He Collisions," The Physical Review, 139, A1025 (1965).

17. Lichten, W., "Resonant Charge Exchange in Atomic Collisions, II. Further Applications and Extension to the Quasi-Resonant Case," The Physical Review, 139, A27 (1965).

18. Lane, G.H., and Everhart, E., "Ion-Atom Potential Energy Functions Obtained from keV Scattering Data," The Physical Review, 120, 2064 (1960).

19. Zehr, F.J., and Berry, H.W., "Elastic Scattering of Lithium Ions in Helium and Hydrogen," The Physical Review, 159, 13 (1967).

20. Whitaker, E.T., and Watson, G.N., Modern Analysis, (Cambridge University Press, Cambridge, 1927), 4th Ed., p. 77.

21. Kopal, Z., Numerical Analysis (Chapman and Hall, Ltd., London, 1961), p. 384.

22. Klemperer, O., Electron Optics (Cambridge University Press, Cambridge, 1953).

23. Jahnke, E., and Emde, F., Tables of Functions (Dover Publications, New York, 1945).

24. Chancon, P.,Annuals of Physics, 2, 333 (1947).

25. Dawson, P.H., and Tickner, A.W., "Detection of H_5^+ in the Hydrogen Glow Discharge," Journal of Chemical Physics, 37, 672, (1962).

APPENDIX I

THE EFFECT OF TARGET SIZE AND ION BEAM

ENERGY SPREAD ON THE SOLID ANGLE

The expression for the angular spread (see Section 5, Chapter II) was

$$d\Theta = \frac{dZ_o - \left(\frac{\partial Z_o}{\partial E}\right)_{\Theta R'Z'} dE - \left[\left(\frac{\partial Z_o}{\partial R'}\right)_{E\Theta Z'} dR' + \left(\frac{\partial Z_o}{\partial Z'}\right)_{E\Theta R'} dZ'\right]}{\left(\frac{\partial Z_o}{\partial \Theta}\right)_{ER'Z'}},$$

where E is the ion beam energy,

dE is the energy spread of the beam,

dR' is the effective target radius,

dZ' is the effective target length.

No analytical method exists for calculating the four partial derivatives. They are computed by solving a number of trajectories where E, Θ, R', and Z' are varied appropriately and the corresponding change in the intercept distance, Z_o, is noted. The value of dE offers no problem since it is the energy spread of the incident ion beam. It depends only on the source being used and can be measured independently (for the $^6Li^+$ source $dE \cong 0.25$ eV). The quantities dR' and dZ' cannot be arbitrarily chosen because they are functions of the trajectories and the detector geometry. The maximum size of the interaction region is determined by the diameter of the cell's beam entrance aperture and the cell's exit slit through which the scattered ions depart as illustrated in Figure 18 (Section 5 of Chapter 3). However, the actual region from which an ion can scatter and enter the detector is smaller

than this and depends upon the trajectory of the ion. This can be seen by recalling that the effective detector opening is determined by ΔZ_o, which depends on θ_o (see Appendix II), which in turn depends on the particular trajectory. Thus a particle can enter the detector only if it crosses the axis within $Z_o \pm \Delta Z_o/2$ and at the proper angle, θ_o, regardless of where it originated in the target gas. Therefore to evaluate dR' or dZ' one would have to evaluate trajectories for many different values of dR' or dZ' until the trajectory with the maximum dR' or dZ' is found. In general the derivatives $(\partial Z_o/\partial R')$ and $(\partial Z_o/\partial Z')$ are linear for a given reaction. Thus the change in $d\theta$ due to varying values of dR' and dZ' is linear and symmetric about its value for dR' = 0 and dZ' = 0. The most extreme values of dR' and dZ' an ion can have and still be detected will give the largest positive and negative corrections to $d\theta$. At values larger than these, $d\theta$ is zero and, consequently, $d\Omega$ is zero. Thus it is apparent that the finite target size corrections are such that the average $d\Omega$ is essentially equal to the value of $d\Omega$ obtained for scattering from the target center. It is suggested that a detailed study of the problem be made on an analog computer by tracing the trajectories backwards from the detector to the scattering cell and defining dR' and dZ' by this technique. The average solid angle is then obtained by integration over the total target volume contributing at each detector and magnet setting.

However, one may obtain an estimate of the maximum effect of finite target size on the solid angle by calculating the change in ΔZ_o due to changes in the interaction volume, as follows: For

an ion to be detected, it must recross the axis within a length $Z_o \pm \Delta Z_o/2$ where Z_o is the distance between the detector and the scattering center and ΔZ_o is determined by θ_o and the detector geometry (see Appendix II). Now let the detector be placed at Z_o so that it will detect particles scattered from the center of the cell at an angle θ. The angle the particles make with the axis as they recross it is θ_o. Ions scattered at θ at some point in the target other than the center will recross the axis at Z_o' with an angle θ_o'. Since ΔZ_o decreases as θ_o increases those particles with $\theta_o' > \theta_o$ will be detected only if

$$Z_o - \frac{\Delta Z_o}{2} < Z_o' < Z_o + \frac{\Delta Z_o}{2}$$

and there will be no increase in the effective solid angle from them. However, those particles with $\theta_o' < \theta_o$ will be detected when

$$Z_o - \frac{\Delta Z_o'}{2} \leq Z_o' \leq Z_o + \frac{\Delta Z_o'}{2}$$

and the effective solid angle will be increased. Therefore we need only to consider those trajectories where $\theta_o' < \theta_o$. An analysis of the trajectories of ions scattered from different places in the target show that those scattered on the ion source side of the center and those scattered off the axis will recross it at distances less than those scattered from the center and that they will have larger θ_o values. Consequently they cause no increase in ΔZ_o since they must cross the axis within ΔZ_o of Z_o to be detected. Those scattered on the detector side of the center or those which originate off the axis and recross it before leaving

the scattering cell will cross at distances greater than those scattered from the center and will have a smaller θ_o value. Thus they will be detected if they have a $Z_o' \leq Z_o + \frac{\Delta Z_o'}{2}$. Therefore the actual ΔZ_o correction is

$$\Delta Z_o^c = \frac{\Delta Z_o + \Delta Z_o'}{2} .$$

Therefore, for a particular energy, angle of scatter, and magnetic field one finds $(\partial \theta_o / \partial Z_o)$ for varying dR' and dZ' values from trajectory results, then gets

$$\theta_o' = \theta_o + \left(\frac{\partial \theta_o}{\partial Z_o}\right) \Delta Z_o$$

which gives a $\Delta Z_o'$. This is applied to give the proper value of ΔZ_o^c. Table II shows the results of the ΔZ_o^c calculation for $^6Li^+$ on N_2 at 100 eV. Notice that varying dR' gives the larger value for $(\partial \theta_o / \partial Z_o)$ and therefore the smallest value of θ_o'. This was used to calculate $\Delta Z_o'$ since this was the largest correction. The largest error is about 8% and as the angle increases the error decreases.

The energy correction is straightforward. The derivative $(\partial Z_o / \partial E)$ is evaluated from trajectory data. The energy spread dE is determined separately for the particular ion source and the correction $(\partial Z_o / \partial E)dE$ is calculated. This correction is about 6%.

TABLE II. Solid Angle Corrections for $^6Li^+$ on N_2 at 100 eV

I_B	θ	Z'	R'	Z_o	θ_o	ΔZ_o	$\frac{\partial Z_o}{\partial Z'}$	$\frac{\partial Z_o}{\partial R'}$	Vary R' $\partial\theta_o/\partial Z_o$	Vary Z' $\partial\theta_o/\partial Z_o$	θ'_o	$\Delta Z'_o$	$\frac{\Delta Z_o+\Delta Z'_o}{2}$	$\frac{\Delta Z_o^c}{\Delta Z_o}$	$\frac{\partial Z_o}{\partial E}dE$	ΔZ_o^c	$\frac{\Delta Z_o^c}{\Delta Z_o}$
13.80	38.0	.0	.0	23.97	18.96	-1.73	4.28	-5.30	-.72	-.66	17.72	-1.99	-1.86	1.07	-.069	-1.80	1.04
		.0	.3	22.38	20.12												
		.3	.0	25.31	18.10												
		-.3	.0	22.74	19.81												
13.47	40.0	.0	.0	23.99	19.86	-1.59	4.37	-5.04	-.76	-.69	18.66	-1.80	-1.70	1.06	-.070	-1.66	1.04
		.0	.3	22.48	21.01												
		.3	.0	25.36	18.94												
		-.3	.0	22.74	20.77												
13.10	42.0	.0	.0	24.14	20.65	-1.46	4.48	-4.87	-.78	-.72	19.52	-1.64	-1.55	1.05	-.071	-1.53	1.05
		.0	.3	22.68	21.79												
		.3	.0	25.54	19.67												
		-.3	.0	22.85	21.63												
12.75	44.0	.0	.0	24.16	21.52	-1.35	4.57	-4.63	-.81	-.75	20.43	-1.49	-1.42	1.05	-.072	-1.42	1.05
		.0	.3	22.77	22.65												
		.3	.0	25.59	20.47												
		-.3	.0	22.85	22.55												
12.35	46.0	.0	.0	24.37	22.22	-1.26	4.75	-4.50	-.82	-.77	21.19	-1.39	-1.32	1.05	-.073	-1.33	1.05
		.0	.3	23.02	23.34												
		.3	.0	25.86	21.11												
		-.3	.0	23.01	23.33												
12.05	48.0	.0	.0	24.06	23.31	-1.12	4.77	-4.20	-.87	-.82	22.34	-1.15	-1.14	1.01	-.073	-1.19	1.06
		.0	.3	22.80	24.41												
		.3	.0	25.56	22.13												
		-.3	.0	22.70	24.48												
11.68	50.0	.0	.0	24.04	24.17	-1.02	4.87	-4.00	-.90	-.85	23.26	-1.03	-1.02	1.00	-.074	-1.09	1.07
		.0	.3	22.84	25.25												
		.3	.0	25.57	22.91												
		-.3	.0	22.65	25.41												

11.30	52.0	.0	.0	24.03	25.00	-0.93	5.00	-3.87	-.93	-.88	24.14	-0.93	-0.93	1.00	-.075	-1.00	1.08
		.0	.3	22.87	26.08												
		.3	.0	25.60	23.67												
		-.3	.0	22.60	26.32												

All distances measured in cm and angles and degrees. I_B measured in amps.

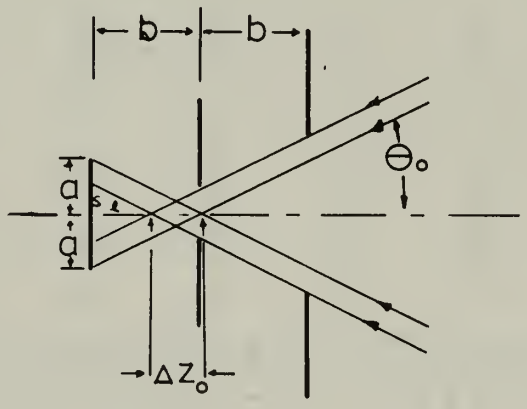
APPENDIX II

CALCULATION OF THE INTERCEPT SPREAD

The fact that the detector apertures are of a finite size allows all ions whose intercept values are $Z_o \pm \Delta Z_o/2$ to enter the detector and be collected. This allowable intercept spread, ΔZ_o, depends on the detector aperture geometry and on the angle θ_o between the ion path as it enters the detector apertures and the center line. This is readily seen in Figure A2-1. In general, then, as θ_o increases, ΔZ_o decreases.

The specific relationships between ΔZ_o and θ_o can be found as follows:

Consider an incident beam of ions whose outer edge is determined by the outer aperture and whose inner edge is determined by the multiplier grid opening. ΔZ_o for this case can be calculated from the geometry shown below.



Now $\Delta Z_o = (-\ell + a) \cot \theta_o$

but $\ell = s \cot \theta_o$

and $\frac{s+f}{2b} = \tan \theta_o$

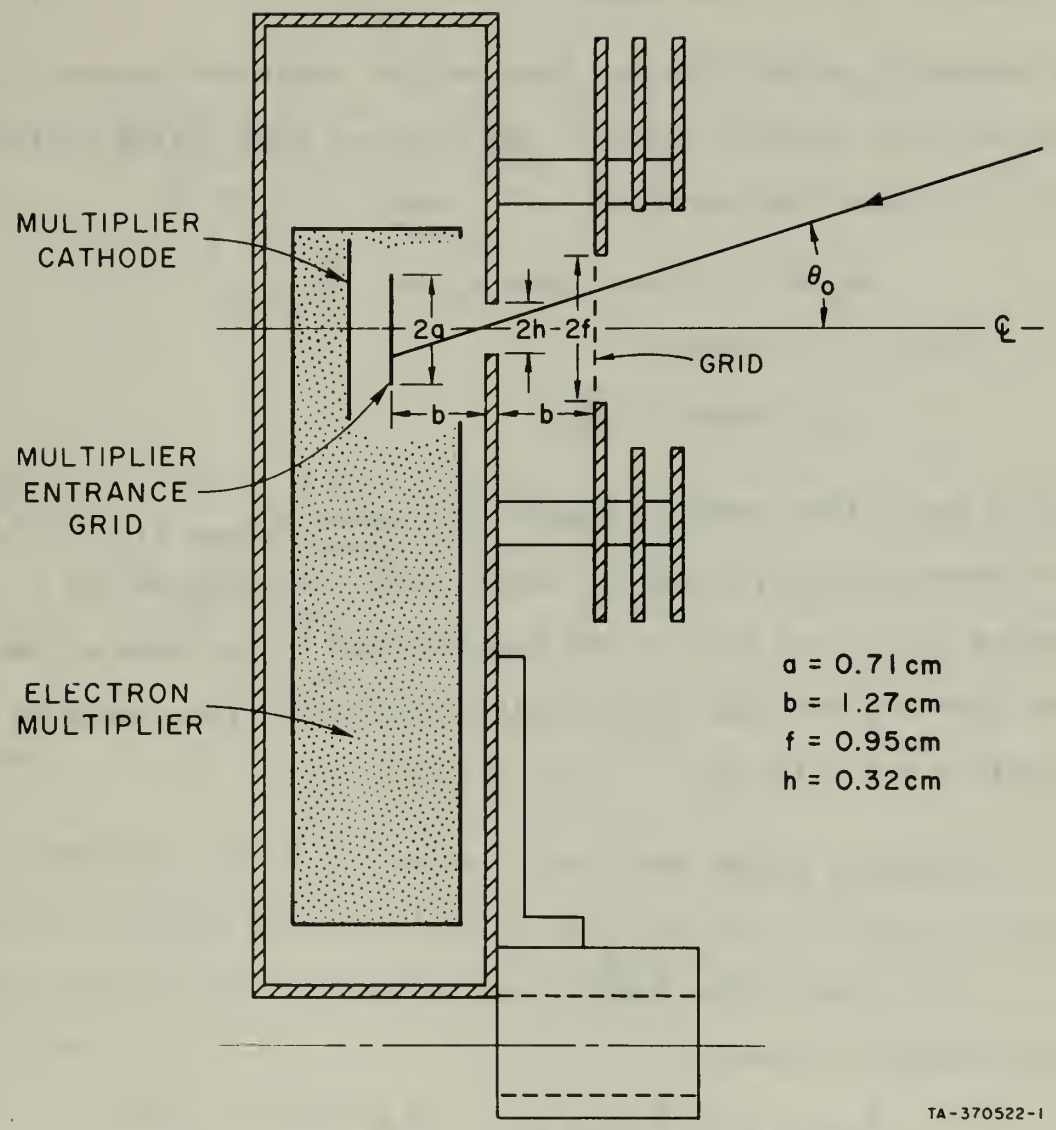


Figure A2-1. Detector Aperture Geometry.

or $s = 2b \tan \theta_o - f$

giving $\ell = 2b - f \operatorname{cotan} \theta_o$

which gives $\Delta Z_o = (f+a) \operatorname{cotan} \theta_o - 2b.$ (1)

The maximum θ_o a particle can have is that angle defined by a line from the outer aperture edge to the farthest edge of the multiplier grid. For this trajectory $\Delta Z_o = 0$. Thus

$$\Delta Z_o = 0 = (f+a) \operatorname{cotan} \theta_o - 2b$$

$$\operatorname{cotan} \theta_o = 2b/(f+a)$$

$$\theta_o = \operatorname{cotan}^{-1} \left(\frac{2b}{f+a}\right)$$

putting the values shown in Figure A2-1 gives $\theta_{o(\max I)} = 33.2^o$. As we decrease θ_o equation (1) holds until the angle of the incoming ion is the same as the angle formed by the edge of the outer aperture and edge of the shield aperture. This angle is found from the relation

$$\tan \theta_o = \frac{f-h}{b}$$

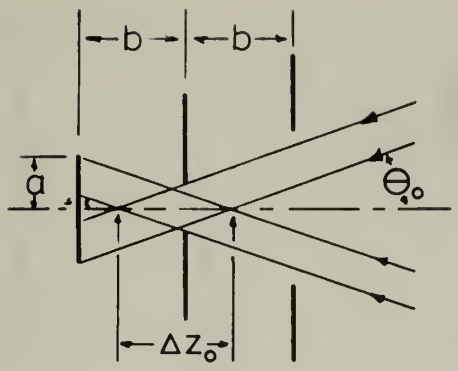
$$\theta_o = \tan^{-1} \left(\frac{f-h}{b}\right)$$

and putting the values

$$\theta_{o(\min I)} = \theta_{o(\max II)} = 26.6^o.$$

This is the smallest θ_o for which equation (1) determines ΔZ_o.

Now consider an incident beam of ions with $\theta_o = 26.6^o$ whose outer edge is determined by the shield aperture and whose inner edge is determined by the multiplier grid opening. This is shown in the following figure.



Again $\Delta Z_o = -\ell + a \text{ cotan } \Theta_o$

$\ell = s \text{ cotan } \Theta_o$

and $\frac{h+s}{b} = \tan \Theta_o$

$s = b \tan \Theta_o - h$

giving $\Delta Z_o = (h+a) \text{ cotan } \Theta_o - b.$ (2)

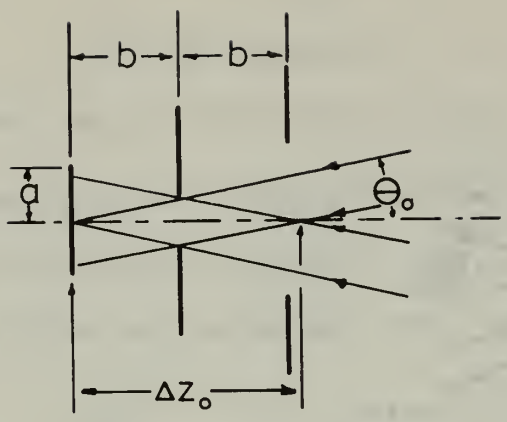
As Θ_o decreases the limit on the inner edge of the incident ion beam will finally be determined by the line from the edge of the shield aperture to the nearest edge of the multiplier grid. At this time

$$\tan \Theta_o = \frac{a-h}{b}$$

or $\Theta_{o(\text{min II})} = \Theta_{o(\text{max III})} = 17.3^o.$

This is the lower limit on the use of equation (2).

The final case occurs when the incident beam of ions is limited only by the shield aperture. The following sketch illustrates these limits.



Here $\Delta Z_o = 2h \text{ cotan } \theta_o$. (3)

Thus, the three possible ways a beam of incident ions can be limited by our detector geometry along with the applicable expression for ΔZ_o are:

I. For $33.2^o \geq \theta_o \geq 26.6^o$

$\Delta Z_o = (f+a) \text{ cotan } \theta_o - 2b;$

II. For $26.6^o \geq \theta_o \geq 17.3^o$

$\Delta Z_o = (h+a) \text{ cotan } \theta_o - b;$

III. For $17.3^o \geq \theta_o \geq 0^o$

$\Delta Z_o = 2h \text{ cotan } \theta_o$

Figure A2-2 shows a plot of ΔZ_o vs θ_o over the appropriate angular range.

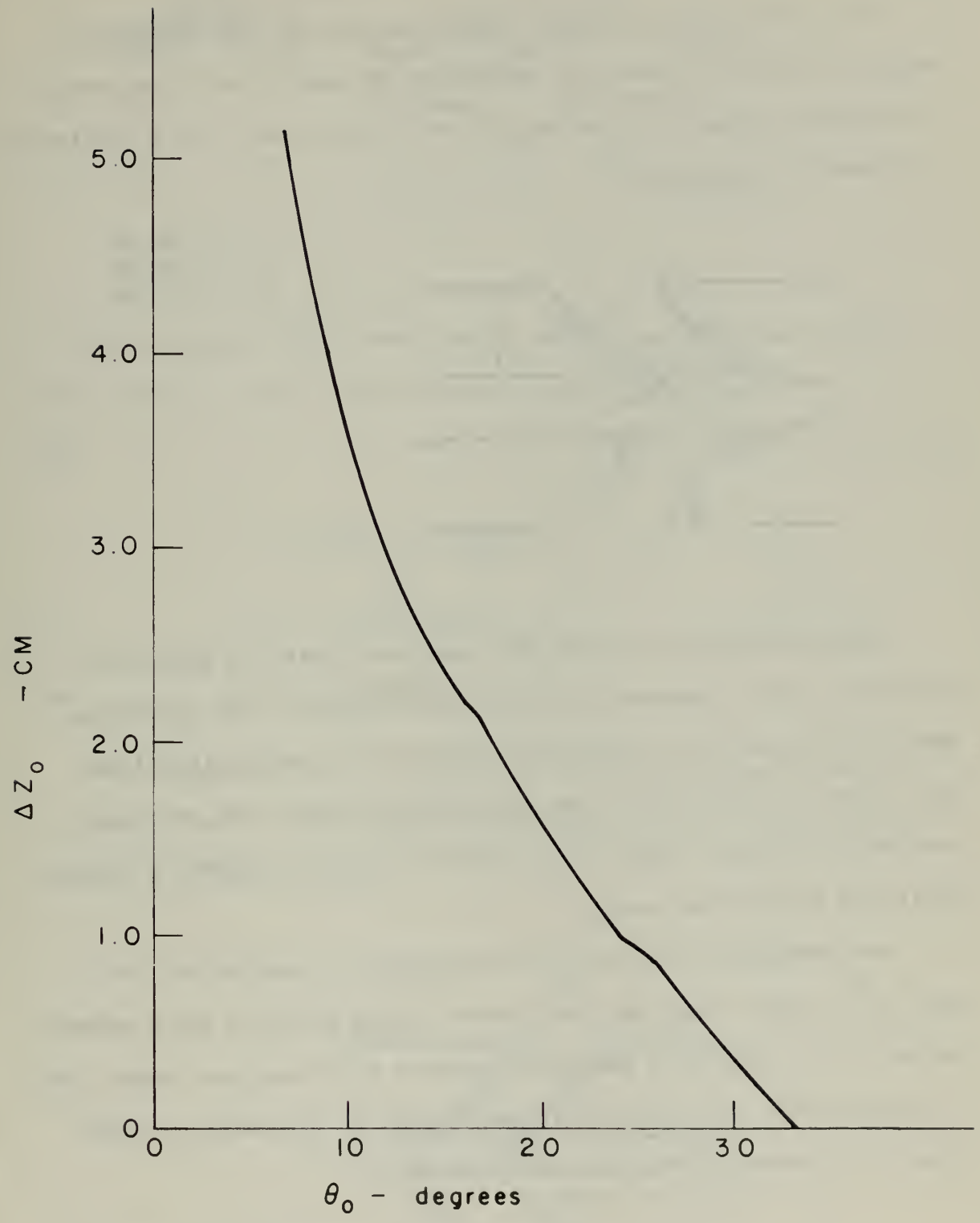
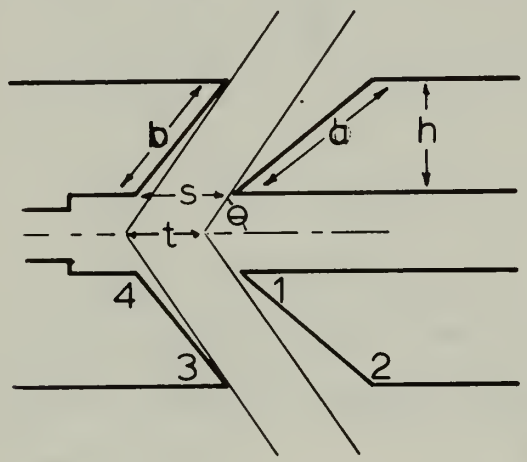


Figure A2-2. Intercept Spread vs Intercept Angle.

APPENDIX III

CALCULATION OF TARGET THICKNESS

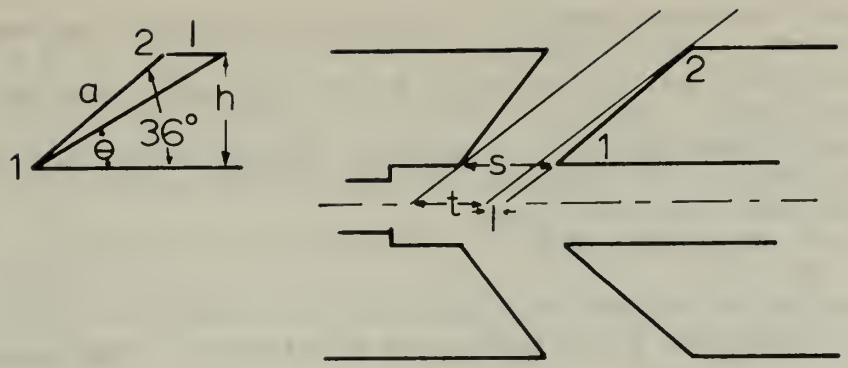
The thickness, t, of the target depends on the scattering angle, θ, the slit openings, which can be controlled from outside the vacuum system, and the angles which the sides of the scattering cell make at the exit slit.



a = 2.54 cm
b = 2.00 cm
h = 1.50 cm

From the above sketch of the scattered particle beam exit, the four points (numbered 1,2,3,4,) that restrict the scattered beam can be seen. For particles scattered at angles less than 36°, points 2 and 4 limit the scattering length. For particles scattered at angles equal to or greater than 49°, points 1 and 3 limit the scattering length.

Now consider t for particles scattered at angles, θ, less than 36°. Then t must be the distance along the cell axis between two parallel lines each making an angle θ with the axis, where one of the parallel lines passes through point 2; the other through point 4, as shown on the following sketch.



To find t analytically, construct a third line parallel to the first two and require that it pass through point 1.

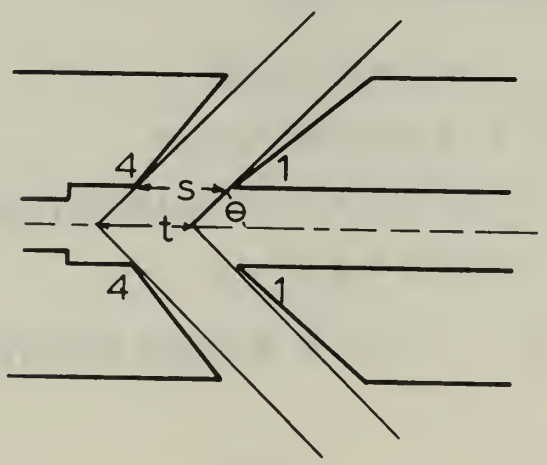
Then $t = s - \ell$ and ℓ can be found from the law of sines

$$\frac{\ell}{\sin(36^\circ-\theta)} = \frac{a}{\sin\theta}$$

or $$\ell = a \sin(36^\circ-\theta)/\sin\theta$$

and $$t = s - a \sin(36^\circ-\theta)/\sin\theta. \qquad (1)$$

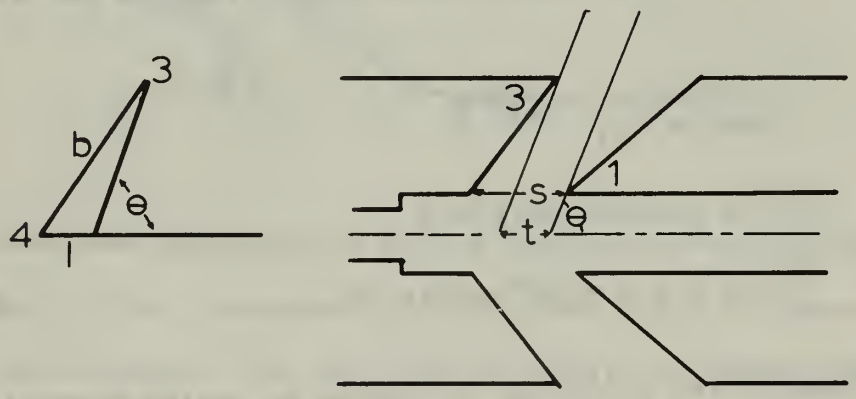
Now consider t for particles scattered at angles θ equal to or greater than 36° but less than or equal to 49°. This case is shown in the sketch below.



Here t is the distance along the scattering cell axis between two parallel lines each making an angle θ with the axis; one of the lines passing through point 1, the other through point 4. Then it is obvious that for this case

$$t = S. \qquad (2)$$

Finally, consider t for particles scattered at angles greater than 49°. For this case t must be the distance along the cell axis between two parallel lines each making an angle θ with the axis; one of the lines passing through point 1, the other line passing through point 3, as shown below.



It can be seen from the sketch that $t = S - \ell$.

Again using the law of sines one has

$$\frac{\ell}{\mathrm{Sin}(\theta-49^{\circ})} = \frac{b}{\mathrm{Sin}\theta}$$

giving $\ell = b\ \mathrm{Sin}(\theta-49^{\circ})/\mathrm{Sin}\theta$

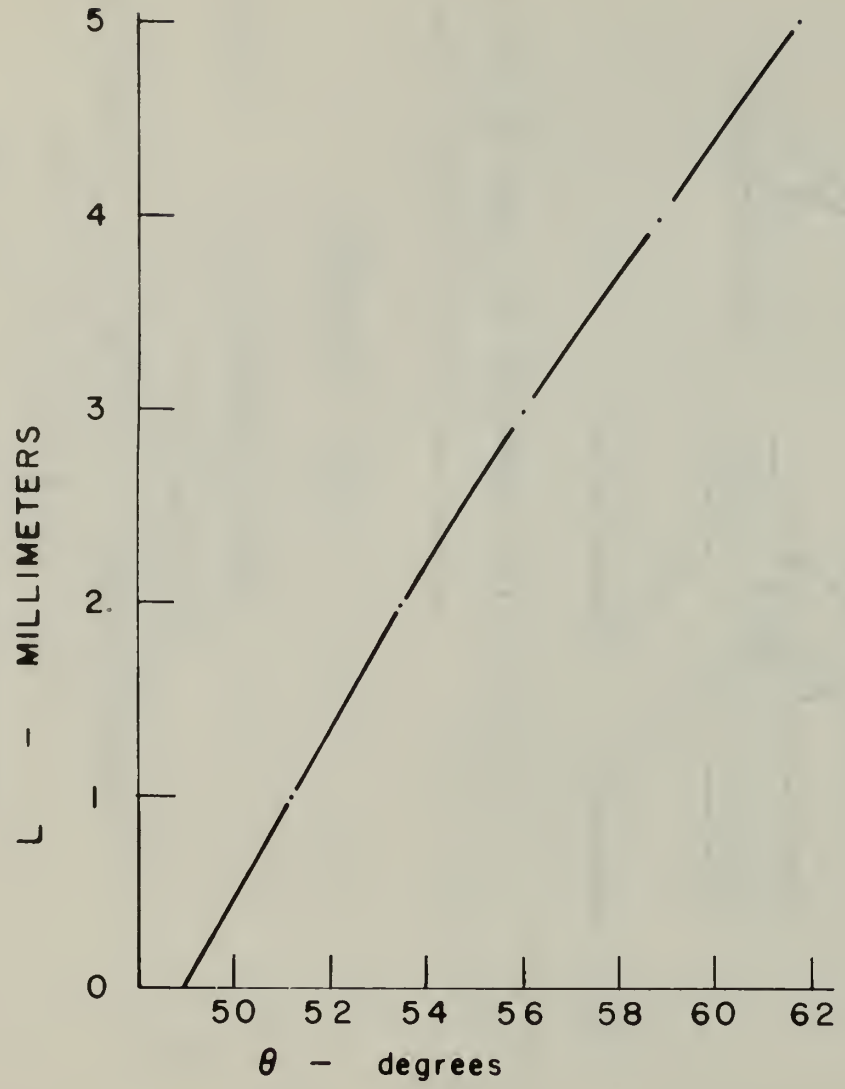
$$t = S - b\ \mathrm{Sin}(\theta-49^{\circ})/\mathrm{Sin}\theta. \qquad (3)$$

In summary: $\theta < 36^{\circ}$: $t = S - a\ \mathrm{Sin}(36^{\circ}-\theta)/\mathrm{Sin}\theta$

$36^{\circ} \le \theta \le 49^{\circ}$: $t = S$

$49^{\circ} \le \theta$: $t = S - b\ \mathrm{Sin}(\theta-49^{\circ})/\mathrm{Sin}\theta$

A plot of ℓ vs θ is shown in Figure A3-1. From this relation the scattering length, t, can be obtained. Figure A3-2 is a plot of t vs θ for a scattering cell opening of 0.3 centimeters. Note that it depends on two things: (1) the length of the scattering cell exit slit and, (2) the angle of scatter being observed.



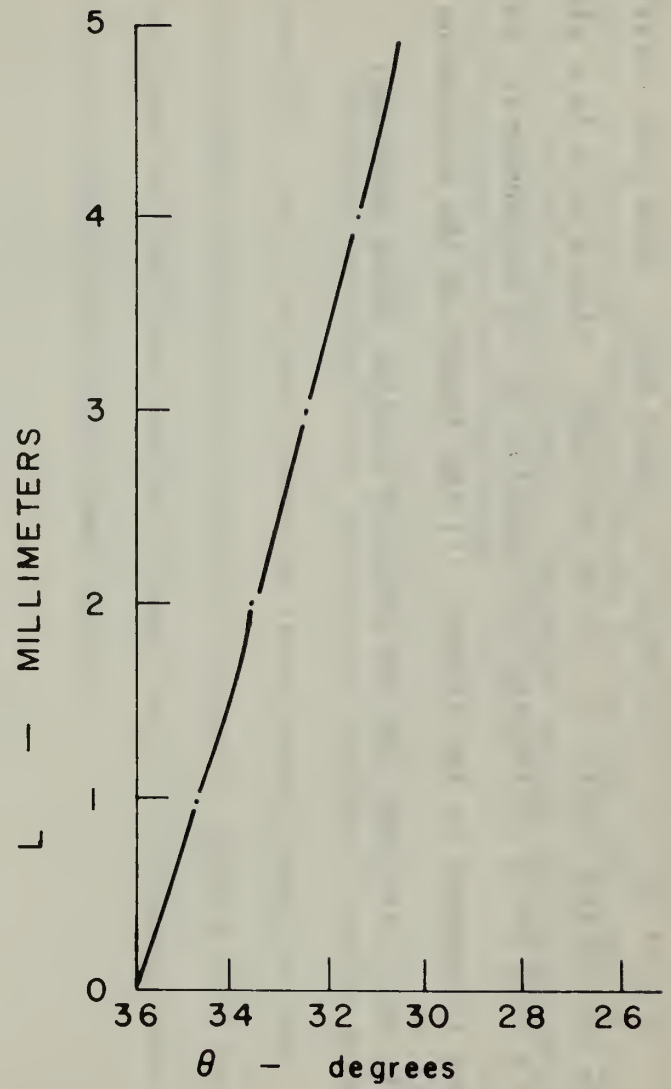


Figure A3-1. Target Thickness Correction vs Scattering Angle (Lab).

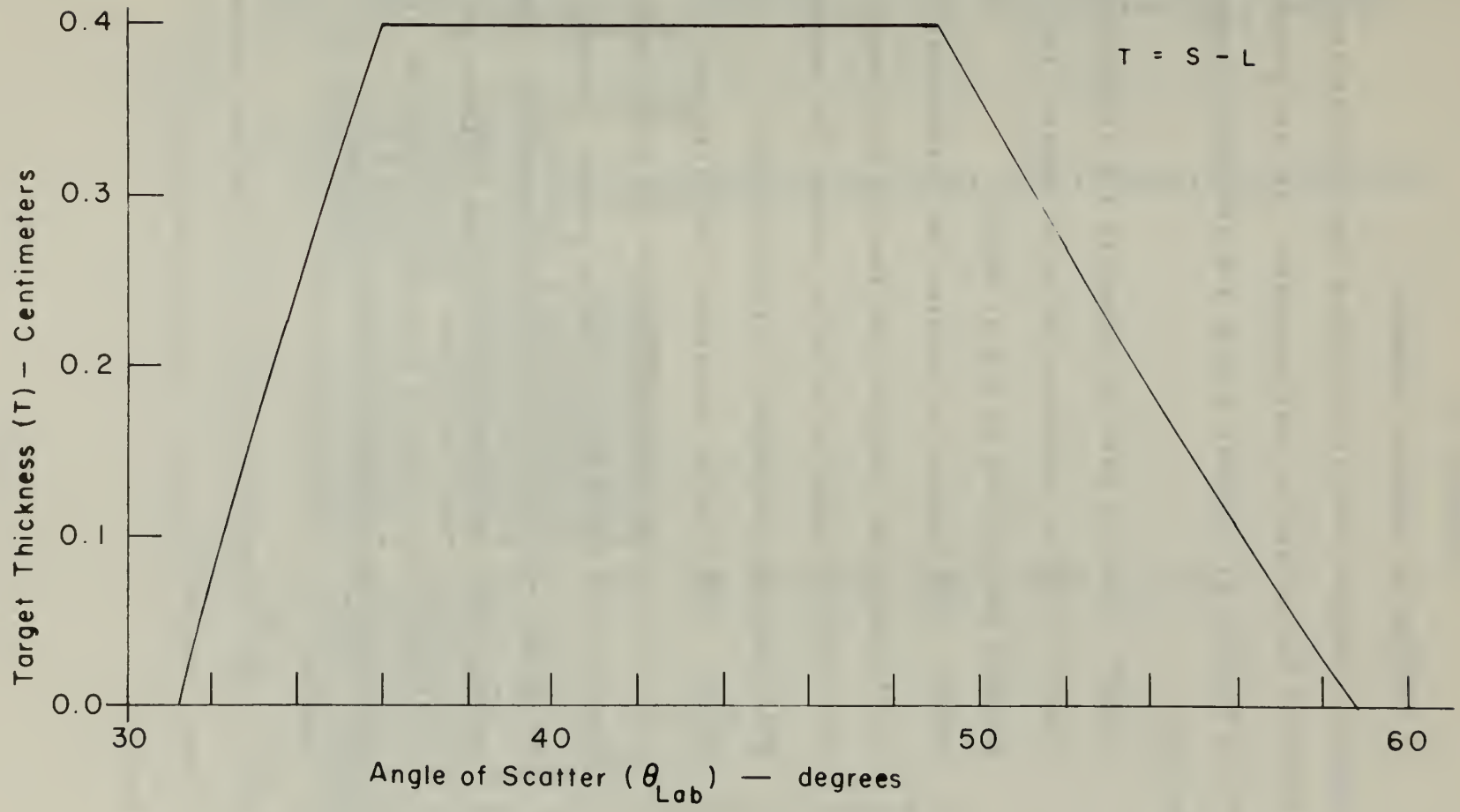


Figure A3-2. Target Thickness vs Scattering Angle for an 0.4 cm Cell Opening.

APPENDIX IV

LISTING OF COMPUTER PROGRAMS

The computer programs used to calculate the solid angles and the cross sections are listed in this appendix. All the programs were written in Fortran VI and were run on the IBM 360-67 computer. The programs are:

1. SOLANG: This is used to integrate the trajectory equation and to calculate the solid angle. This program was written by N.R.A. Smyth.
2. CSVSZ: This program calculates the differential scattering cross section from the raw data where the observed angle is varied by moving the detector while keeping the magnet current constant.
3. CSVSI: This program calculates the differential scattering cross section from the raw data where the observed angle of scatter is varied by changing the magnet current while keeping the detector fixed.
4. PSIGMA: This program calculates the differential scattering cross section from the raw data for the case where the target has less mass than the projectile.

All three cross section programs give both the laboratory system and center of mass system values for the cross section and scattering angle.

```
C   THIS PROGRAM CALLS ON THE SUBROUTINE DHPCG TO SOLVE TWO DIFFERENTIAL
C   EQUATIONS DESCRIBING THE TRAJECTORY OF THE SCATTERED ION.  IT ALSO
C   MAKES LEAST SQUARES FITS OF THE TRAJECTORY RESULTS AND USES THEM TO
C   CALCULATE THE SOLID ANGLE.
C
C
      IMPLICIT REAL*8(A-H,O-Z)
      REAL*8 ITITLE(12)/12*8H          /
      REAL*8 LABEL/8H          /
      REAL*4 THET,ZEE
      DIMENSION PRMT(9),Y(2),DERY(2),AUX(16,2),B(13),THESD(99),THEZD(99)
     *,ZEROD(99),THET(99),ZEE(99)
      COMMON B,P,OKAY
      EXTERNAL FCT,OUTP
      CALL CANCEL(2)
      B( 1)=  8.0498907D-02
      B( 2)=  2.3351831D-02
      B( 3)= -4.8664438D+00
      B( 4)=  4.2887590D+01
      B( 5)= -4.3626183D+02
      B( 6)=  3.9271101D+03
      B( 7)= -2.2648265D+04
      B( 8)=  8.2393030D+04
      B( 9)= -1.9359723D+05
      B(10)=  2.9437706D+05
      B(11)= -2.8025472D+05
      B(12)=  1.5200646D+05
      B(13)= -3.5865075D+04
C
C   F IS THE PROJECTILE MASS AND T IS THE TARGET MASS IN AMU.
      READ(5,17)F,T
   17 FORMAT(2F10.0)
      READ(5,4001) NOT
 4001 FORMAT(I2)
      DO 400 NO =1,NOT
      READ(5,10)(ITITLE(J),J=1,6)
   10 FORMAT(6A8)
      WRITE(6,11)(ITITLE(J),J=1,6)
   11 FORMAT(1H1,6A8,////)
      JON=1
      READ(5,3)ENIT,CUR,THINIT,THINC,THFIN
    3 FORMAT(5F10.5)
      TOM=THINIT-THINC
      NGR=(THFIN-THINIT)/THINC +1.0
      DO 50 I=1,NGR
```

```
      PRMT(1)=0.0
      PRMT(2)=0.9
      PRMT(3)=0.1D-01
      PRMT(4)=0.1D-06
      PRMT(6)=0.0
      TOM=TOM+THINC
      THESD(JON)=TOM
      A=T*T-F*F
      THR=THESD(JON)*3.14159/180.
      G=F*DCOS(THR)
      C=(T+F)*(T+F)
      AA=A+G*G
      IF(AA)50,50,20
   20 ENER = ENIT*(A+2.*G*G+2.*G*DSQRT(AA))/C
      OKAY=(2.0727D-08)*F*ENER
      P=CUR/10.0
      Y(1)=0.0
      TILT=THESD(JON)/57.2957795131
      STILL=DTAN(TILT)
      Y(2)=STILL
      NOGOOD=0
    4 DERY(1)=0.5
      DERY(2)=0.5
      CALL DHPCG(PRMT,Y,DERY,2,IHLF,FCT,OUTP,AUX)
      IF(IHLF-11)30,22,22
   22 NOGOOD =NOGOOD+1
      PRMT(3)=PRMT(3)/10.0
      PRMT(4)=PRMT(4)/100.0
      IF(NOGOOD-3)21,30,30
   21 Y(1)=0.0
      Y(2)=STILL
      GO TO 4
   30 CONTINUE
      FRACT=PRMT(7)/(PRMT(7)-Y(1))
      Y(1)=0.0
      Y(2)=PRMT(8)+FRACT*(Y(2)-PRMT(8))
      ZEROD(JON)=(PRMT(6)+FRACT*(PRMT(9)-PRMT(6)))*100.0
      THO=DATAN(Y(2))
      THOD=THO*57.2957795131
      THEZD(JON)=DABS(THOD)
      WRITE(6,5)  I,CUR,ENIT,ENER,THESD(JON),ZEROD(JON),Y(1),THEZD(JON)
    5 FORMAT(     2X,'RUN=',I2,T12,'CURRENT=',F4.1,T26,'E(INITIAL)=',F5.
     *1,T46,'E(SCAT)=',F5.1,T62,'THETA(S)=',F4.1,//,10X,'Z(ZERO)=',F6.2,
     *T32,'ZERO RADIUS=',D9.2,T58,'THETA(ZERO)=',F5.2)
      IF(IHLF.GE.11.OR.ZEROD(JON).GE.80.0)GO TO 7
```

```
      WRITE(6,6)IHLF
    6 FORMAT(/,10X,'IHLF=',I2,5X,'THIS RUN IS GOOD',////)
      GO TO 8
    7 WRITE(6,9)IHLF
    9 FORMAT(/,10X,'IHLF=',I2,5X,'THIS RUN IS IGNORED',////)
      GO TO 50
    8 JON=JON+1
   50 CONTINUE
      JON=JON-1
      DO 12 K=1,JON
      THET(K)=THESD(K)
   12 ZEE(K)=ZEROD(K)
      CALL DRAW(JON,THET,ZEE,0,0,LABEL,ITITLE,0,C,0,0,1,1,9,15,1,LAST)
      WRITE(6,13)LAST
   13 FORMAT(2X,'GRAPH OF Z VS THETA HAS LAST=',I2)
      ZINT=ZEE(1)
      ZFIN=ZEE(1)
      DO 54 I =1,JON
      IF(ZINT-ZEE(I))54,54,55
   55 ZINT=ZEE(I)
   54 CONTINUE
      DO 56 I =1,JON
      IF(ZFIN-ZEE(I))51,56,56
   51 ZFIN=ZEE(I)
   56 CONTINUE
      CALL SOLID(THESD,ZEROD,THEZD,JON,ZINT,ZFIN)
  400 CONTINUE
      RETURN
      END
```

```
      SUBROUTINE FCT(X,Y,DERY)
      IMPLICIT REAL*8(A-H,O-Z)
      DIMENSION Y(2),DERY(2),B(13),F(6),G(7)
      COMMON B,P,OKAY
      F(1)=B(2)+2.*B(3)*X+3.*B(4)*X**2+4.*B(5)*X**3+5.*B(6)*X**4+6.*B(7)
     1*X**5+7.*B(8)*X**6+8.*B(9)*X**7+9.*B(10)*X**8+10.*B(11)*X**9+11.*B
     2(12)*X**10+12.*B(13)*X**11
      F(2)=6.*B(4)+24.*B(5)*X+60.*B(6)*X**2+120.*B(7)*X**3+210.*B(8)*X**
```

```
14+336.*B(9)*X**5+504.*B(10)*X**6+720.*B(11)*X**7+990.*B(12)*X**8+1
2320.*B(13)*X**9
 F(3)=120.*B(6)+720.*B(7)*X+2520.*B(8)*X**2+6720.*B(9)*X**3+15120.*
1B(10)*X**4+30240.*B(11)*X**5+55440.*B(12)*X**6+95040.*B(13)*X**7
 F(4)=5040.*B(8)+40320.*B(9)*X+181440.*B(10)*X**2+604800.*B(11)*X**
13+1663200.*B(12)*X**4+3991680.*B(13)*X**5
 F(5)=362880.*B(10)+3628800.*B(11)*X+19958400.*B(12)*X**2+79833600.
1*B(13)*X**3
 F(6)=39916800.*B(12)+479001600.*B(13)*X
 VECDZ=Y(1)*F(1)/2.-F(2)*Y(1)**3/16.+F(3)*Y(1)**5/384.-F(4)*Y(1)**7
1/18432.+F(5)*Y(1)**9/1474560.-F(6)*Y(1)**11/176947200.
 G(1)=B(1)+B(2)*X+B(3)*X**2+B(4)*X**3+B(5)*X**4+B(6)*X**5+B(7)*X**6
1+B(8)*X**7+B(9)*X**8+B(10)*X**9+B(11)*X**10+B(12)*X**11+B(13)*X**1
22
 G(2)=2.*B(3)+6.*B(4)*X+12.*B(5)*X**2+20.*B(6)*X**3+30.*B(7)*X**4+4
12.*B(8)*X**5+56.*B(9)*X**6+72.*B(10)*X**7+90.*B(11)*X**8+110.*B(12
2)*X**9+132.*B(13)*X**10
 G(3)=24.*B(5)+120.*B(6)*X+360.*B(7)*X**2+840.*B(8)*X**3+1680.*B(9)
1*X**4+3024.*B(10)*X**5+5040.*B(11)*X**6+7920.*B(12)*X**7+11880.*B(
213)*X**8
 G(4)=720.*B(7)+5040.*B(8)*X+20160.*B(9)*X**2+60480.*B(10)*X**3+151
1200.*B(11)*X**4+332640.*B(12)*X**5+665280.*B(13)*X**6
 G(5)=40320.*B(9)+362880.*B(10)*X+1814400.*B(11)*X**2+6652800.*B(12
1)*X**3+19958400.*B(13)*X**4
 G(6)=3628800.*B(11)+39916800.*B(12)*X+239500800.*B(13)*X**2
 G(7)=479001600.*B(13)
 VECDR=G(1)/2.-3.*G(2)*Y(1)**2/16.+5.*G(3)*Y(1)**4/384.-7.*G(4)*Y(1
1)**6/18432.+9.*G(5)*Y(1)**8/1474560.-11.*G(6)*Y(1)**10/176947200.+
213.*G(7)*Y(1)**12/29727129600.
 VECPT=Y(1)*G(1)/2.-G(2)*Y(1)**3/16.+G(3)*Y(1)**5/384.-G(4)*Y(1)**7
1/18432.+G(5)*Y(1)**9/1474560.-G(6)*Y(1)**11/176947200.+G(7)*Y(1)**
213/29727129600.
 FUNC1=OKAY-VECPT*VECPT*P*P
 FUNC2=VECPT*VECDZ*P*P
 FUNC3=VECPT*VECDR*P*P
 FUNC4=(FUNC2)/(FUNC1)
 FUNC5=(FUNC3)/(FUNC1)
 DERY(2)=Y(2)*(FUNC4)+Y(2)*Y(2)*Y(2)*(FUNC4)-Y(2)*Y(2)*(FUNC5)-(FUN
1C5)
 DERY(1)=Y(2)
 RETURN
 END
```

```
      SUBROUTINE OUTP(X,Y,DERY,IHLF,NDIM,PRMT)
C
      REAL*8 Y,PRMT,X
      DIMENSION Y(2),PRMT(9)
      IF((Y(1).LE.0.0).AND.(X.GE.0.5D-01))GO TO 1
      GO TO 2
    1 PRMT(5)=1.0
      PRMT(9)=X
      RETURN
    2 PRMT(6)=X
      PRMT(7)=Y(1)
      PRMT(8)=Y(2)
      RETURN
      END
```



```
      SUBROUTINE SOLID(X,ZZ,YY,M,ZINT,ZFIN)
C   PROGRAM TO COMPUTE THE COEFFICENTS CZ AND CT OF THE LEAST SQUARES
C   FITTED POLYNOMIALS Z(ZERO) VS THETA(S) AND THETA(0) VS THETA(S)
C   RESPECTIVELY.  X(I) IS THETA(S),ZZ(I) IS  Z(0),YY(I) IS THETA(0)
C   KM IS THE MAXIMUM DEGREE OF FIT  AND M IS THE NUMBER OF DATA POINTS-
C   LIMITED TO 500.   FROM THESE POLYNOMIALS THE SOLID ANGLE DOME IS
C   COMPUTED IN THE SUBROUTINE DOMEGA
      IMPLICIT REAL*8(A-H,O-Z)
      DIMENSION X(100),F(100),W(100),YY(99),DELY(100),B(20),SB(20),T(20)
     1,ST(20),C(20),SC(20),A(30,30),CZ(11),CT(11),ZZ(99),Y(100),CTZ(11)
      READ(5,1)KM
    1 FORMAT(I1)
      IR=KM+1
      JIM=-1
      DO 3 I=1,11
      CZ(I)=0.0
      CTZ(I)=0.0
    3 CT(I)=0.0
   11 IF(JIM)21,22,23
   21 DO 6 I=1,M
    6 F(I)=ZZ(I)
      GO TO 7
   22 DO 8 I=1,M
    8 F(I)=YY(I)
```

```
      GO TO 7
   23 DO 16 I=1,M
      F(I)=X(I)
   16 X(I)=ZZ(I)
    7 CALL LSQPOL(M,KM,0,1,1,SIGMA,X,F,W,Y,DELY,B,SB,T,ST,C,SC,A)
      JIM=JIM+1
      IF(JIM-1)9,12,14
    9 DO 10 I=1,IR
   10 CZ(I)=B(I)
      GO TO 11
   12 DO 13 I=1,IR
   13 CT(I)=B(I)
      GO TO 11
   14 DO 15 I=1,IR
   15 CTZ(I)=B(I)
      CALL DOMEGA(CZ,CT,CTZ,ZINT,ZFIN)
      RETURN
      END
```



```
      SUBROUTINE DOMEGA(CZ,CT,CTZ,ZINT,ZFIN)
C   PROGRAM TO COMPUTE THE SOLID ANGLE DOME                                  1
C   LIMITED TO 900 ITERATIONS BETWEEN THETA INITIAL AND THETA FINAL          2
C   MAX DEGREE OF POLYNOMIALS 10                                             3
C                                                                            4
      IMPLICIT REAL*8(A-H,O-Z)                                               5
      REAL*8 ITITLE(12)/12*8H        /
      REAL*8 LABEL/8H        /                                               7
      REAL*4 X,Y                                                             8
      DIMENSION X(900),Y(900),CZ(20),CT(20),T(900),DOME(900),TR(900),THE
     *T(900),CTZ(20),Z(900)
      IZINT=ZINT
      IZFIN=ZFIN+1.0
      ZINT=IZINT
      ZFIN=IZFIN
      IF(ZFIN-55.0)21,21,22
   22 ZFIN=55.0
   21 CONTINUE
      ZINC=0.5
```

```
      Z(1)=ZINT
      K1=(ZFIN-ZINT)/ZINC +1.0
      DO 3 I =2,K1
      J=I-1
    3 Z(I)=Z(J)+ZINC
      READ(5,5)(ITITLE(J),J=1,6)                                          25
    5 FORMAT(6A8)                                                         26
      WRITE(6,11)(ITITLE(J),J=1,6)
   11 FORMAT(1H1,6A8,//)
C COMPUTE THE SOLID ANGLE FOR VARIOUS VALUES OF Z
      WRITE(6,6)                                                          28
    6 FORMAT(4X,'Z',T11,'THETA',T17,'SOLID ANGLE',T29,'D(THETA)/DZ',T41,
     *'DZ',T45,'THETA(0)',//)
      DO 7 I =1,K1                                                        30
      T(I)=ANG(CTZ,Z(I))
      SLOP=SLOPE(CZ,T(I))                                                 31
      TR (I)=T(I)/57.2957795131D+0C
      D=DELZ(CT,T(I),TR(I))                                               32
      S=DSIN(TR(I))                                                       33
      P=0.08731D+00
      DOME(I)=DABS(P*S*SLOP*D)                                            35
    7 WRITE(6,8)Z(I),T(I),DOME(I),SLOP,D
    8 FORMAT(1H+,2X,F4.1,T10,F7.4,T19,F8.6,T31,F7.4,T41,F3.1,T46,F5.2)
      DO 9 I=1,K1                                                         38
      THET(I)=T(I)
      X(I)=T(I)                                                           39
    9 Y(I)=DOME(I)                                                        40
      CALL DRAW(K1,X,Y,0,0,LABEL,ITITLE,0,0,0,0,1,1,9,15,1,LAST)          41
      WRITE(6,10)LAST                                                     42
   10 FORMAT(//,5X,'LAST=',I5)                                            43
      RETURN                                                              44
      END                                                                 45
```

```
      FUNCTION ANG(CTZ,Z)
      IMPLICIT REAL*8(A-H,O-Z)
      DIMENSION CTZ(11)
      ANG=CTZ(1) +CTZ(2)*Z +CTZ(3)*Z**2 +CTZ(4)*Z**3 +CTZ(5)*Z**4 +CTZ(6
     *)*Z**5 +CTZ(7)*Z**6 +CTZ(8)*Z**7 +CTZ(9)*Z**8 +CTZ(10)*Z**9 +CTZ(1
     *1)*Z**10
      RETURN
      END
```

```
      FUNCTION SLOPE(CZ,F)                                              46
      IMPLICIT REAL*8(A-H,O-Z)                                          47
      DIMENSION CZ(11)
      DZDT=CZ(2)+2.0*CZ(3)*F    +3.0*CZ(4)*F**2    +4.0*CZ(5)*F**3    +5.0*  49
     1CZ(6)*F**4    +6.0*CZ(7)*F**5    +7.0*CZ(8)*F**6    +8.0*CZ(9)*F**7    50
     8 +9.0*CZ(10)*F**8    +10.0*CZ(11)*F**9                              51
      SLOPE=1.0/DZDT                                                    52
    4 RETURN
      END                                                               56
```

```
      FUNCTION DELZ(CT,G,TR)                                            55
      IMPLICIT REAL*8(A-H,O-Z)                                          56
      DIMENSION CT(11),T(900)                                           57
      TZERD= CT(1) +CT(2)*G +CT(3)*G**2 +CT(4)*G**3 +CT(5)*G**4 +CT(6)*G
     1**5 +CT(7)*G**6 +CT(8)*G**7 +CT(9)*G**8 +CT(10)*G**9 +CT(11)*G**10
      TZERR=TZERD/57.2957795131                                         61
      WRITE(6,9)TZERD
    9 FORMAT(46X,F5.2)
      IF(TZERD-1.0)11,12,12
   11 GO TO 7
   12 CONTINUE
      IF(TZERD-17.3)1,1,2                                               62
    1 DELZ=0.635*DCOTAN(TZERR)                                          63
```

```
      GO TO 7                                                           64
    2 IF(TZERD-26.6)3,3,4                                               65
    3 DELZ=1.0318*DCOTAN(TZERR)-1.27                                    66
      GO TO 7                                                           67
    4 IF(TZERD-33.2)5,5,6                                               68
    5 DELZ=1.6668*DCOTAN(TZERR)-2.54                                    69
      GO TO 7                                                           70
    6 WRITE(6,8)                                                        71
    8 FORMAT(1H+,5X,'THETA(ZERO) GREATER THAN 33.2 DEGREES',/)
    7 CONTINUE                                                          73
      RETURN                                                            74
      END
```

```
C     CSVSZ - THIS PROGRAM CALCULATES THE  CROSS SECTION  WHEN THE DATA
CC            WAS TAKEN BY KEEPING THE DETECTOR FIXED AND VARYING THE
CC            MAGNET CURRENT.
CC
C
      REAL*8 ITITLE(12),IBLANK/8H        /,LABEL/8H        /
      DIMENSION F(11),TL(100),SLA(100),CT(9),B(13),TO(9),TCM(100),
     1          SCM(100)
      RHO=3.536E+16
C
CC    THE B(I) COEFFICIENTS ARE THE AXIAL MAGNETIC FIELD STRENGTH VS Z
C     12TH ORDER POLYNOMIAL FIT.
      B( 1)=  8.0498907E-02
      B( 2)=  2.3351831E-02
      B( 3)= -4.8664438E+00
      B( 4)=  4.2887590E+01
      B( 5)= -4.3626183E+02
      B( 6)=  3.9271101E+03
      B( 7)= -2.2648265E+04
      B( 8)=  8.2393030E+04
      B( 9)= -1.9359723E+05
      B(10)=  2.9437706E+05
      B(11)= -2.8025472E+05
      B(12)=  1.5200646E+05
      B(13)= -3.5865075E+04
C
CC    THE F(I) COEFFICIENTS ARE THE LOG10(MULTIPLIER GAIN) VS AXIAL
CC    FIELD STRENGTH  10TH ORDER POLYNOMIAL FIT FOR  VDSI=-2100,
C     VFSI=-1500, VDSO=-100, VFSO=GND.
      F( 1)=  6.6096404E+00
      F( 2)=  8.4788178E-03
      F( 3)=  2.8883953E-04
      F( 4)= -7.9040318E-05
      F( 5)=  2.2180903E-06
      F( 6)= -2.9003866E-08
      F( 7)=  2.1658254E-10
      F( 8)= -9.8154008E-13
      F( 9)=  2.6812272E-15
      F(10)= -4.0704638E-18
      F(11)=  2.6397846E-21
C
CC    TM IS TARGET MASS IN AMU.  PM IS ION MASS IN AMU.
      READ(5,103)TM,PM
  103 FORMAT(2F10.0)
C
```

```
C     THE CT(I) COEFFICIENTS GIVE THETA /S Z.
      READ(5,101)(CT(I),I=1,7)
C
C     THE TO(I) COEFFICIENTS GIVE THETA ZERO VS THETA
      READ (5,101)(TO(I),I=1,7)
  101 FORMAT(3E20.7)
      READ(5,105)NR
  105 FORMAT(I2)
      DO 99 K=1,NR
      READ(5,100) NRPTS,S,PSCG,BMAG,PGC
  100 FORMAT(I5,F5.0,E10.3,2F5.0)
      PSC=PSCG*PGC
      TGTPT =PSCG*RHO*PGC
      WRITE(6,112) TM,PM,S,PSC,BMAG
  112 FORMAT(1H1,///,T10,'TGT  MASS(AMU) =',1PE13.6,/,
     1                T10,'PROJ MASS(AMU) =',1PE13.6,/,
     2                T10,'CELL OPENING   =',1PE13.6,/,
     3                T10,'CELL PRESSURE  =',1PE13.6,/,
     4                T10,'MAGNET CURRENT =',0PF5.1)
      WRITE(6,110)
  110 FORMAT(/////,T2,'Z ',T6,'THETA(L)',T16,'SIGMA(L)',T26,'THETA(CM)',
     1       T36,'SIGMA(CM)',T46,'COLL CUR',T56,'DET CUR',T66,'DOME',
     2       T75,'GAIN',T85,'T',//)
      DO 51 I=1,NRPTS
      READ(5,102)Z,BCI,DI
  102 FORMAT(F5.0,2E10.3)
      Z=Z+15.5
      ZM=Z
      Z=Z/100.
      HO = B(1)+B(2)*Z+B(3)*Z**2+B(4)*Z**3+B(5)*Z**4+B(6)*Z**5+B(7)*Z**6
     1+B(8)*Z**7+B(9)*Z**8+B(10)*Z**9+B(11)*Z**10+B(12)*Z**11+B(13)*Z**1
     22
      HO=HO*BMAG*1000.
      G=F(1)+F(2)*HO+F(3)*HO**2+F(4)*HO**3+F(5)*HO**4+F(6)*HO**5
     1+F(7)*HO**6+F(8)*HO**7+F(9)*HO**8+F(10)*HO**9+F(11)*HO**10
      G = 10.**G
      Z=ZM
      THETA = CT(1)+CT(2)*Z+CT(3)*Z**2+CT(4)*Z**3+CT(5)*Z**4+CT(6)*Z**5
     1       +CT(7)*Z**6
      THL= THETA*3.14159/180.
      IF(THETA-49.)11,11,12
   11 IF(THETA-36.)13,14,14
C
C     T WHEN THETA IS GREATER THAN 49 DEG.
   12 T=S-1.3122+1.5094*COTAN(THL)
```

```
      GO TO 16
C
C     T WHEN THETA IS LESS THAN 36 DEG.
   13 T=S-1.493*COTAN(THL)+2.0548
      GO TO 16
C
C     T WHEN THETA LIES BETWEEN 36 AND 49 DEGREES.
   14 T=S
   16 IF(T-.01)18,17,17
   18 WRITE(6,115)Z,THL
  115 FORMAT(F5.1,T8,F5.2,T15,'..T IS LESS THAN 0.01 CM.',/)
      GO TO 51
   17 DTDZ = CT(2) +2.*CT(3)*Z +3.*CT(4)*Z**2 +4.*CT(5)*Z**3 +5.*CT(6)
     1*Z**4+6.*CT(7)*Z**5
      DTDZ = ABS(DTDZ)
      THO = TO(1)+TO(2)*THETA+TO(3)*THETA**2+TO(4)*THETA**3+TO(5)*THETA*
     1*4+TO(6)*THETA**5+TO(7)*THETA**6
      THOR = THO*3.14159/180.
   30 IF(THO-17.3)31,31,32
   31 DZ = 0.635*COTAN(THOR)
      GO TO 35
   32 IF(THO-26.6)33,33,34
   33 DZ = 1.0318*COTAN(THOR)-1.27
      GO TO 35
   34 DZ = 1.6668*COTAN(THOR)-2.54
   35 DOME = 0.08731281*SIN(THL)*DTDZ*DZ
      SL=DI/(G*BCI*TGTPT*T*DOME)
      SQ = SQRT(TM*TM/(PM*PM)-1.+COS(THL)**2)
      C = 1.-COS(THL)**2-COS(THL)*SQ
      C = C*PM/TM
      THC = ARCOS(C)
      THC = 3.14159- THC
   21 A=1.+(PM/TM)*COS(THC)
      A = ABS(A)
      BA= PM*PM/(TM*TM)+2.*(PM/TM)*COS(THC)+1.
      BA = SQRT(BA)
      BA = BA*BA*BA
      SC = SL*A/BA
      THL=THL*180./3.14159
      THC=THC*180./3.14159
      TCM(I)=THC
      SCM(I)=ALOG10(SC)
   50 WRITE(6,111)Z,THL,SL,THC,SC,BCI,DI,DOME,G,T
  111 FORMAT(F5.1,T8,F5.2,T15,1PE10.3,T27,0PF6.2,T35,1P3E10.3,
     1       T66,0PF6.4,1PE10.3,0PF8.5,/)
```

```
 51 CONTINUE
    READ(5,104)(ITITLE(J),J=1,12)
104 FORMAT(6A8)
 52 IF(ITITLE(1)-IBLANK)60,61,60
 60 CALL DRAW(NRPTS,TCM,SCM,0,2,LABEL,ITITLE,0,0,0,0,1,1,9,15,1,LAST)
    WRITE(6,113)LAST
113 FORMAT(T10,'LAST = ',I1)
    GO TO 99
 61 WRITE(6,114)
114 FORMAT(///,T5,'... NO GRAPH REQUESTED.')
 99 CONTINUE
    RETURN
    END
```

```
C     CSVSI - THIS PROGRAM CALCULATES THE CROSS SECTION WHEN THE DATA
C             WAS TAKEN BY KEEPING THE MAGNET CURRENT FIXED AND MOVING
C             THE DETECTOR.
C
      REAL*8 ITITLE(12),IBLANK/8H         /,LABEL/8H         /
      DIMENSION F(11),TL(100),SLA(100),CT(9),B(13),TO(9),TCM(100),
     1          SCM(100)
      RHO=3.536E+16
C
C     THE B(I) COEFFICIENTS ARE THE AXIAL MAGNETIC FIELD STRENGTH VS Z
C     12TH ORDER POLYNOMIAL FIT.
      B( 1)=  8.0498907E-02
      B( 2)=  2.3351831E-02
      B( 3)= -4.8664438E+00
      B( 4)=  4.2887590E+01
      B( 5)= -4.3626183E+02
      B( 6)=  3.9271101E+03
      B( 7)= -2.2648265E+04
      B( 8)=  8.2393030E+04
      B( 9)= -1.9359723E+05
      B(10)=  2.9437706E+05
      B(11)= -2.8025472E+05
      B(12)=  1.5200646E+05
      B(13)= -3.5865075E+04
C
C     THE F(I) COEFFICIENTS ARE THE LOG10(MULTIPLIER GAIN) VS AXIAL
C     FIELD STRENGTH  10TH ORDER POLYNOMIAL FIT FOR  VDSI=-2100,
C     VFSI=-1500, VDSO=-100, VFSO=GND.
      F( 1)=  6.6096404E+00
      F( 2)=  8.4788178E-03
      F( 3)=  2.8883953E-04
      F( 4)= -7.9040318E-05
      F( 5)=  2.2180903E-06
      F( 6)= -2.9003866E-08
      F( 7)=  2.1658254E-10
      F( 8)= -9.8154008E-13
      F( 9)=  2.6812272E-15
      F(10)= -4.0704638E-18
      F(11)=  2.6397846E-21
C
C     TM IS TARGET MASS IN AMU.  PM IS ION MASS IN AMU.
      READ(5,103)TM,PM
  103 FORMAT(2F10.0)
C
```

```
C     THE CT(I) COEFFICIENTS GIVE THETA VS MAGNET CURRENT
      READ(8,101)(CT(I),I=1,7)
C
C     THE TO(I) COEFFICIENTS GIVE SOLID ANGLE VS MAGNET CURRENT
      READ (5,101)(TO(I),I=1,7)
  101 FORMAT(3E20.7)
      READ(5,105)NR
  105 FORMAT(I2)
      DO 99 K=1,NR
      READ(5,100)NRPTS,S,PSCG,Z,PGC
  100 FORMAT(I5,F5.0,E10.3,2F5.0)
      Z=Z+15.5
      PSC=PSCG*PGC
      TGTPT =PSCG*RHO*PGC
      WRITE(6,112)TM,PM,S,PSC,Z
  112 FORMAT(1H1,///,T10,'TGT  MASS(AMU) =',1PE13.6,/,
     1               T10,'PROJ MASS(AMU) =',1PE13.6,/,
     2               T10,'CELL OPENING   =',1PE13.6,/,
     3               T10,'CELL PRESSURE  =',1PE13.6,/,
     4               T10,'DETECTOR DIST. =',0PF5.2)
      WRITE(6,110)
  110 FORMAT(/////,T2,'IB',T6,'THETA(L)',T16,'SIGMA(L)',T26,'THETA(CM)',
     1       T36,'SIGMA(CM)',T46,'COLL CUR',T56,'DET CUR',T66,'DOME',
     2       T75,'GAIN',T85,'T',//)
      Z=Z/100.
      DO 51 I=1,NRPTS
      READ(5,102)BMAG,BCI,DI
  102 FORMAT(F5.0,2E10.3)
      HO = B(1)+B(2)*Z+B(3)*Z**2+B(4)*Z**3+B(5)*Z**4+B(6)*Z**5+B(7)*Z**6
     1+B(8)*Z**7+B(9)*Z**8+B(10)*Z**9+B(11)*Z**10+B(12)*Z**11+B(13)*Z**1
     22
      HO=HO*BMAG*1000.
      G=F(1)+F(2)*HO+F(3)*HO**2+F(4)*HO**3+F(5)*HO**4+F(6)*HO**5
     1+F(7)*HO**6+F(8)*HO**7+F(9)*HO**8+F(10)*HO**9+F(11)*HO**10
      G = 10.**G
      THETA=CT(1)+CT(2)*BMAG+CT(3)*BMAG**2+CT(4)*BMAG**3+CT(5)*BMAG**4
     1+CT(6)*BMAG**5
      THL= THETA*3.14159/180.
      IF(THETA-49.)11,11,12
   11 IF(THETA-36.)13,14,14
C
C     T WHEN THETA IS GREATER THAN 49 DEG.
   12 T=S-1.3122+1.5094*COTAN(THL)
      GO TO 16
C
```

```
C       T WHEN THETA IS LESS THAN 36 DEG.
   13   T=S-1.493*COTAN(THL)+2.0548
        GO TO 16
C
C       T WHEN THETA LIES BETWEEN 36 AND 49 DEGREES.
   14   T=S
   16   IF(T-.01)18,17,17
   18   WRITE(6,115)Z,THL
  115   FORMAT(F5.1,T8,F5.2,T15,'..T IS LESS THAN 0.01 CM.')
        GO TO 51
   17   CONTINUE
C
        DOME= TO(1)+TO(2)*BMAG+TO(3)*BMAG**2+TO(4)*BMAG**3+TO(5)*BMAG**4+
       1TO(6)*BMAG**5
        SL=DI/(G*BCI*TGTPT*T*DOME)
        SQ = SQRT(TM*TM/(PM*PM)-1.+COS(THL)**2)
        C = 1.-COS(THL)**2-COS(THL)*SQ
        C = C*PM/TM
        THC = ARCOS(C)
        THC = 3.14159- THC
   21   A=1.+(PM/TM)*COS(THC)
        A = ABS(A)
        BA= PM*PM/(TM*TM)+2.*(PM/TM)*COS(THC)+1.
        BA = SQRT(BA)
        BA = BA*BA*BA
        SC = SL*A/BA
        THL=THL*180./3.14159
        THC=THC*180./3.14159
        TL(I) = THL
        SLA(I) = ALOG10(SL)
   50   WRITE(6,111)BMAG,THL,SL,THC,SC,BCI,DI,DOME,G,T
  111   FORMAT(F5.1,T8,F5.2,T15,1PE10.3,T27,0PF6.2,T35,1P3E10.3,
       1         T66,0PF6.4,1PE10.3,0PF8.5,/)
   51   CONTINUE
        READ(5,104)(ITITLE(J),J=1,12)
  104   FORMAT(6A8)
   52   IF(ITITLE(1)-IBLANK)60,61,60
   60   CALL DRAW(NRPTS,TL,SLA,0,1,LABEL,ITITLE,2,.3,0,0,0,0,8,10,1,LAST)
        WRITE(6,113)LAST
  113   FORMAT(T10,'LAST = ',I1)
        GO TO 99
   61   WRITE(6,114)
  114   FORMAT(///,T5,'... NO GRAPH REQUESTED.')
   99   CONTINUE
        RETURN
```

```
C     PSIGMA - THIS PROGRAM CALCULATES THE CROSS SECTION FOR SYSTEMS
C              WHERE THE ION IS HEAVIER THAN THE TARGET. THE SCATTERING
C              ANGLE AND THE SOLID ANGLE MUST BE READ IN.
C
C
      REAL*8 ITITLE(12),IBLANK/8H        /,LABEL/8H        /
      DIMENSION F(11),TL(100),SLA(100),CT(9),B(13),TD(9),TCM(100),
     1          SCM(100)
C
C     THE B(I) COEFFICIENTS ARE THE AXIAL MAGNETIC FIELD STRENGTH VS Z
C     12TH ORDER POLYNOMIAL FIT.
      B( 1)=  8.0498907E-02
      B( 2)=  2.3351831E-02
      B( 3)= -4.8664438E+00
      B( 4)=  4.2887590E+01
      B( 5)= -4.3626183E+02
      B( 6)=  3.9271101E+03
      B( 7)= -2.2648265E+04
      B( 8)=  8.2393030E+04
      B( 9)= -1.9359723E+05
      B(10)=  2.9437706E+05
      B(11)= -2.8025472E+05
      B(12)=  1.5200646E+05
      B(13)= -3.5865075E+04
C
C     THE F(I) COEFFICIENTS ARE THE LOG10(MULTIPLIER GAIN) VS AXIAL
C     FIELD STRENGTH  10TH ORDER POLYNOMIAL FIT FOR  VDSI=-2100,
C     VFSI=-1500, VDSO=-100,  VFSO=GND.
      F( 1)=  6.6096404E+00
      F( 2)=  8.4788178E-03
      F( 3)=  2.8883953E-04
      F( 4)= -7.9040318E-05
      F( 5)=  2.2180903E-06
      F( 6)= -2.9003866E-08
      F( 7)=  2.1658254E-10
      F( 8)= -9.8154008E-13
      F( 9)=  2.6812272E-15
      F(10)= -4.0704638E-18
      F(11)=  2.6397846E-21
      RHO=3.536E+16
C
C     TM IS TARGET MASS IN AMU.  PM IS ION MASS IN AMU.
      READ(5,103)TM,PM
  103 FORMAT(2F10.0)
      READ(5,105) NR
```

```
  105 FORMAT(I2)
      DO 99 K=1,NR
 2001 READ(5,100)NRPTS,S,PSCG,PGC
  100 FORMAT(I5,F5.0,E10.0,F10.0)
      PSC=PSCG*PGC
      WRITE(6,112) TM,PM,S,PSC
  112 FORMAT(1H1,///,T10,'TGT  MASS(AMU) =',1PE13.6,/,
     1                T10,'PROJ MASS(AMU) =',1PE13.6,/,
     2                T10,'CELL OPENING   =',1PE13.6,/,
     3                T10,'CELL PRESSURE  =',1PE13.6)
      WRITE(6,110)
  110 FORMAT(////,T3,'IB',T7,'Z',T14,'THL',T21,'SIGMAL',T32,'THC',T39,
     1        'SIGMA',T48,'COLL CUR',T58,'DET CUR',T68,'DOME',
     2        T78,'GAIN',T90,'T',//)
      TGTPT =PSCG*RHO*PGC
      DO 51 I=1,NRPTS
      READ(5,102)M,BMAG,Z,THETA,DOME,BCI,DI
  102 FORMAT(I2,F5.0,F5.0,F8.0,F10.0,2E10.3)
      Z=Z+15.5
      ZM = Z
      Z = Z/100.
      HO = B(1)+B(2)*Z+B(3)*Z**2+B(4)*Z**3+B(5)*Z**4+B(6)*Z**5+B(7)*Z**6
     1+B(8)*Z**7+B(9)*Z**8+B(10)*Z**9+B(11)*Z**10+B(12)*Z**11+B(13)*Z**1
     22
      HO=HO*BMAG*1000.
      G=F(1)+F(2)*HO+F(3)*HO**2+F(4)*HO**3+F(5)*HO**4+F(6)*HO**5
     1+F(7)*HO**6+F(8)*HO**7+F(9)*HO**8+F(10)*HO**9+F(11)*HO**10
      G = 10.**G
      THL= THETA*3.14159/180.
      IF(THETA-49.)11,11,12
   11 IF(THETA-36.)13,14,14
C
C     T WHEN THETA IS GREATER THAN 49 DEG.
   12 T=S-1.3122+1.5094*COTAN(THL)
      GO TO 16
C
C     T WHEN THETA IS LESS THAN 36 DEG.
   13 T=S-1.493*COTAN(THL)+2.0548
      GO TO 16
C
C     T WHEN THETA LIES BETWEEN 36 AND 49 DEGREES.
   14 T=S
      GO TO 16
   16 IF(T-.01)18,17,17
   18 WRITE(6,115)Z,THL
```

```
  115 FORMAT(F5.1,T8,F5.2,T15,'..T IS LESS THAN 0.01 CM.',/)
      GO TO 51
   17 CONTINUE
      SL=DI/(G*BCI*TGTPT*T*DOME)
      SQ = SQRT(TM*TM/(PM*PM)-1.+COS(THL)**2)
      C = 1.-COS(THL)**2-COS(THL)*SQ
      C = C*PM/TM
      THC = ARCOS(C)
      THC = 3.14159- THC
C
C     NOW TO CHECK AND SEE IF PAST LAB CUTOFF ANGLE.  M=-1 MEANS IT IS
C     AND M=+1 MEANS IT IS NOT.
      IF(M-0)20,20,21
   20 THC=3.14159-THC+2.*THL
   21 A=1.+(PM/TM)*COS(THC)
      A = ABS(A)
      BA= PM*PM/(TM*TM)+2.*(PM/TM)*COS(THC)+1.
      BA = SQRT(BA)
      BA = BA*BA*BA
      SC = SL*A/BA
      THL=THL*180./3.14159
      THC=THC*180./3.14159
      SLA(I) = ALOG10(SL)
      TL(I) = THL
      Z = ZM
   50 WRITE(6,111)BMAG,Z,THL,SL,THC,SC,BCI,DI,DOME,G,T
  111 FORMAT(2F5.1,F7.2,1PE9.2,0PF8.2,1PE10.2,1P2E10.2,0PF9.6,
     1       1PE10.3,0PF8.5,/)
   51 CONTINUE
      READ(5,104)(ITITLE(J),J=1,12)
  104 FORMAT(6A8)
   52 IF(ITITLE(1)-IBLANK)60,61,60
   60 CALL DRAW(NRPTS,TL,SLA,0,1,LABEL,ITITLE,0,0,0,0,0,0,8,10,1,LAST)
      WRITE(6,113)LAST
  113 FORMAT(T10,'LAST = ',I1)
      GO TO 99
   61 WRITE(6,114)
  114 FORMAT(///,T5,'... NO GRAPH REQUESTED.')
   99 CONTINUE
      RETURN
      END
```

APPENDIX V

ION BEAM OPTICS

Many good references[22] on the design and use of electrostatic and magnetic lenses to focus ion beam already exist and are well known by workers in the field. Therefore, only the space charge effect and the focusing properties of an einzel lens will be discussed.

Space Charge

The coulomb interaction among the charged particles in an ion beam causes the beam to spread as it moves away from the source. This spreading due to the space charge sets an upper limit on the amount of beam that can be transported between two apertures. The addition of converging lenses along the path of the ion beam will help reduce the space charge spreading and help deliver more beam to the target area.

The maximum current that can be transported a distance x starting with a radius y_c and ending with a radius y_a can be calculated from the following assumptions:

(1) The radial current density is constant across any beam cross section.

(2) The current density is zero outside the outer ray.

(3) The total current is constant.

(4) The axial velocity of the beam is constant.

The field E at the surface of the beam can be calculated from Gauss' Theorem. Thus

$$\int \rho dv = \int \epsilon \, E_y \, da$$

where ρ = space charge density

da = surface element

dv = volume element.

Now integrating at y_c gives

$$\rho \pi y_c^2 \Delta x = \epsilon E_y 2\pi y \Delta x$$

since all the flux goes out through a cylindrical surface at radius y. Thus

$$E_y = \rho y_c^2 / 2y\epsilon$$

The current I through a cross section πy_c^2 can be found from the linear velocity of the ions, u_x. Therefore

$$I/\pi y_c^2 = \rho u_x$$

or

$$\rho = I/\pi u_x y_c^2$$

Now

$$qE_y = m \frac{d^2y}{dt^2} = q(\rho y_c^2 / 2y\epsilon)$$

and substituting for ρ and solving gives

$$\frac{d^2y}{dt^2} = \frac{q}{2mu_x} \left(\frac{I}{\pi \epsilon y}\right) = b^2/2y$$

where

$$b^2 = qI/mu_x \pi\epsilon = \text{constant.}$$

Now

$$\int \left(\frac{d^2y}{dt^2}\right) \left(2\frac{dy}{dt}\right) dt = \int \frac{b^2}{2y} \left(2 \frac{dy}{dt}\right) dt,$$

integrating

$$\left(\frac{dy}{dt}\right)^2 = b^2 \log y + c. \qquad (1)$$

The initial radius was y_c and at that time all ions were traveling parallel to the x axis, thus

$$\frac{dy_c}{dt} = 0 \text{ giving } c = -b^2 \log y_c.$$

Substituting into equation (1) gives

$$\frac{dy}{dt} = b(\log y/y_c)^{\frac{1}{2}} \text{ which is the differential equation}$$

for ions in the outer ray. To solve this equation let

$$s = (\log y/y_c)^{\frac{1}{2}}$$

or

$$y = y_c e^{s^2} .$$

Then

$$\frac{dy}{dt} = (\frac{dy}{ds})(\frac{ds}{dt}) = bs = y_c\ 2s\ e^{s^2}\ \frac{ds}{dt}$$

giving

$$b = 2y_c\ e^{s^2}\ \frac{ds}{dt} .$$

Now

$$\int_{t_c}^{t} \frac{b}{2y_c}\, dt = \int_{o}^{s} e^{s^2}\, \frac{ds}{dt}$$

or

$$\frac{b}{2y_c}\,(t-t_c) = \int_{o}^{s} e^{s^2}\, \frac{ds}{dt} = D(s)-D(s_c)$$

where D(s) is the Dawson function, which has been tabulated[23]. But

$$t-t_c = (x-x_c)/u_x, \text{ which}$$

gives

$$(\frac{x-x_c}{2y_c u_x})\ b = D(s).$$

Thus $$(x-x_c)/y_c = \frac{2u_x}{b} D(s).$$

Now using $u_x = (\frac{2qV}{m})^{\frac{1}{2}}$ and also substituting for b gives

$$(x-x_c)/y_c = \frac{4(\pi\epsilon)^{\frac{1}{2}} (\frac{q}{2m})^{\frac{1}{2}}}{(I/V^{3/2})^{\frac{1}{2}}} D(s).$$

Therefore the maximum ion beam current that can travel a distance starting at a radius y_c and ending with a radius y, whose energy is qV, for ions having a charge q and mass m is

$$I = 16\pi\epsilon (q/2m)^{\frac{1}{2}} V^{3/2} (\frac{y_c}{x-x_c})^2 (D(s))^2. \qquad (2)$$

For our experimental apparatus

$$x-x_c = 75.0 \text{ cm}$$

$$y_c = 0.25 \text{ cm}$$

$$y = 0.25 \text{ cm}$$

$s^2 = \log y_c/y = 1$ and $D(s) = 1.2463$, giving

$$I = 5.38 \times 10^{-9} \frac{V^{3/2}}{m^{\frac{1}{2}}}$$

where I is in amps, V is in volts and m is in amu.

A plot of I vs V is shown in Figure A5-1 for several different ions.

Einzel Lens

In order to reduce the space charge spreading electrostatic lenses were placed at the source and also about half way between the mass analyser and the scattering cell. The three diaphram einzel lens shown in Figure A5-2 was chosen for both lenses.

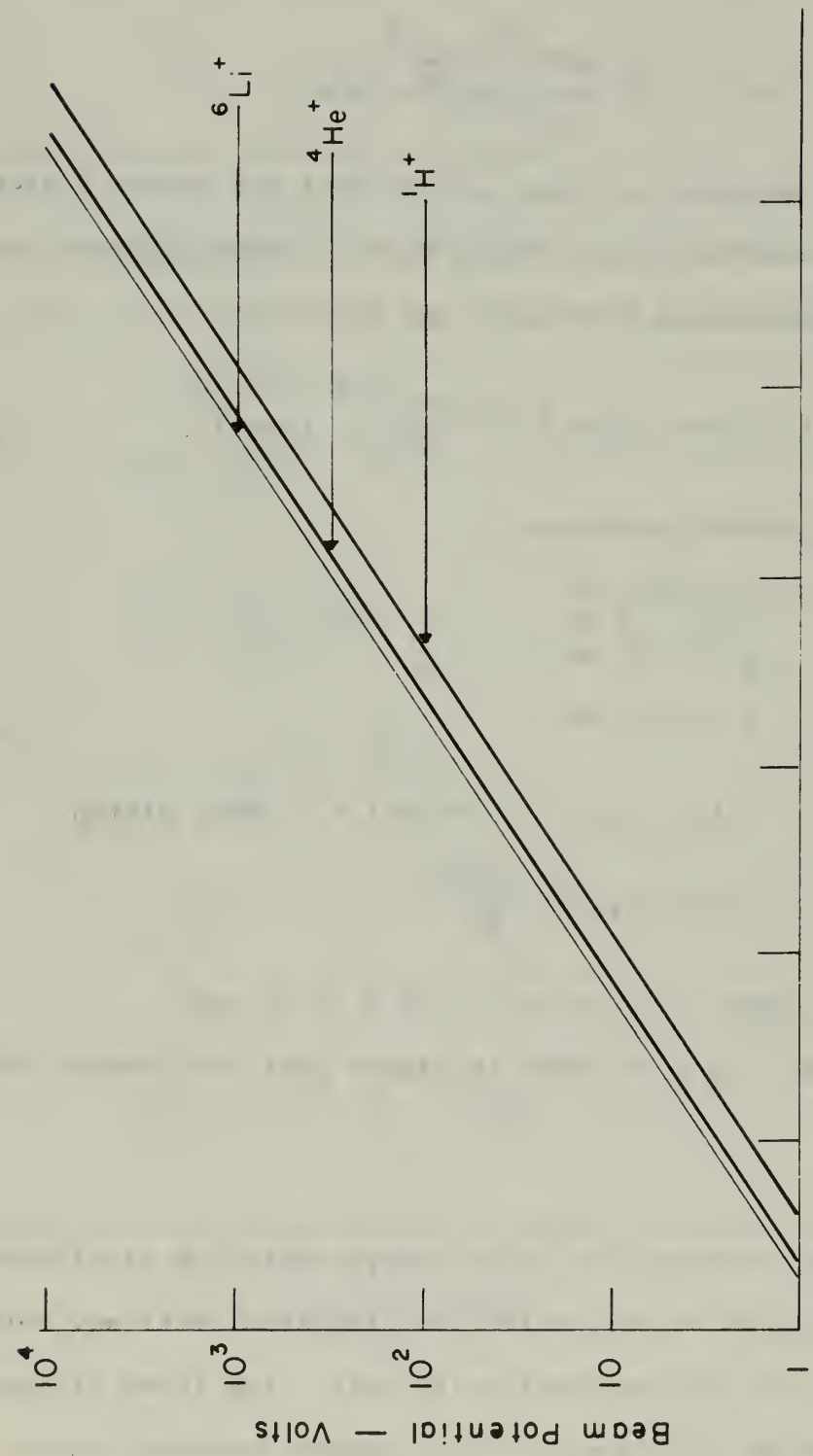


Figure A5-1. Beam Potential vs Beam Current.

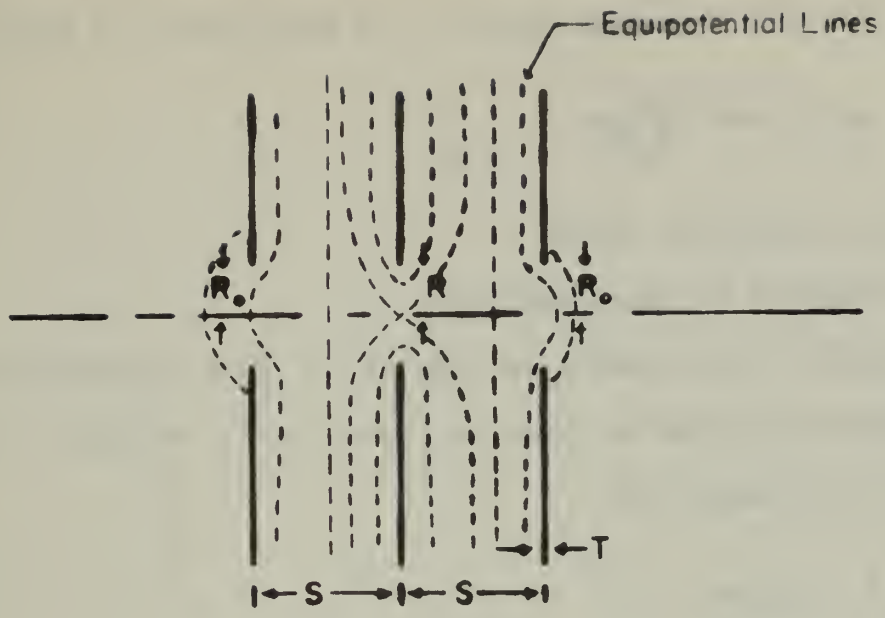


Figure A5-2. Einzel Lens Equipotential Lines.

In this lens the two outer diaphrams are set at ground potential and the potential on the inner diaphram is varied to give the maximum current at the scattering cell. Since the voltages on both sides of the lens are the same the refractive indices are equal on both sides and the three diaphrams act as a single lens with one focal length. In fact the focal length was found to be independent of the applied potential. Chancon[24] investigated this lens by ray tracing and found the following empirical formula for the focal length

$$\frac{f}{s} = 6.5 \left(\frac{\frac{s}{R} \tan^{-1}\left(\frac{s}{R}\right)}{1 + \frac{s}{R} \tan^{-1}\left(\frac{s}{R}\right)} \right)$$

where s = lens separation

R = center aperture radius

The distance between principal point P and mid-plane M is given by

$$MP = 0.06 \frac{Rs}{R_o + T}$$

where R_o = outer aperture radius

T = thickness of the diaphrams.

The focal length relation holds as long as $T < \frac{1}{10} S$. A plot of the focal length relation is shown in Figure A5-2. For the lenses used in our apparatus

$$S = 1.4 \text{ cm}$$

$$R = 0.7 \text{ cm}$$

which gives $f = 6.3$ cm

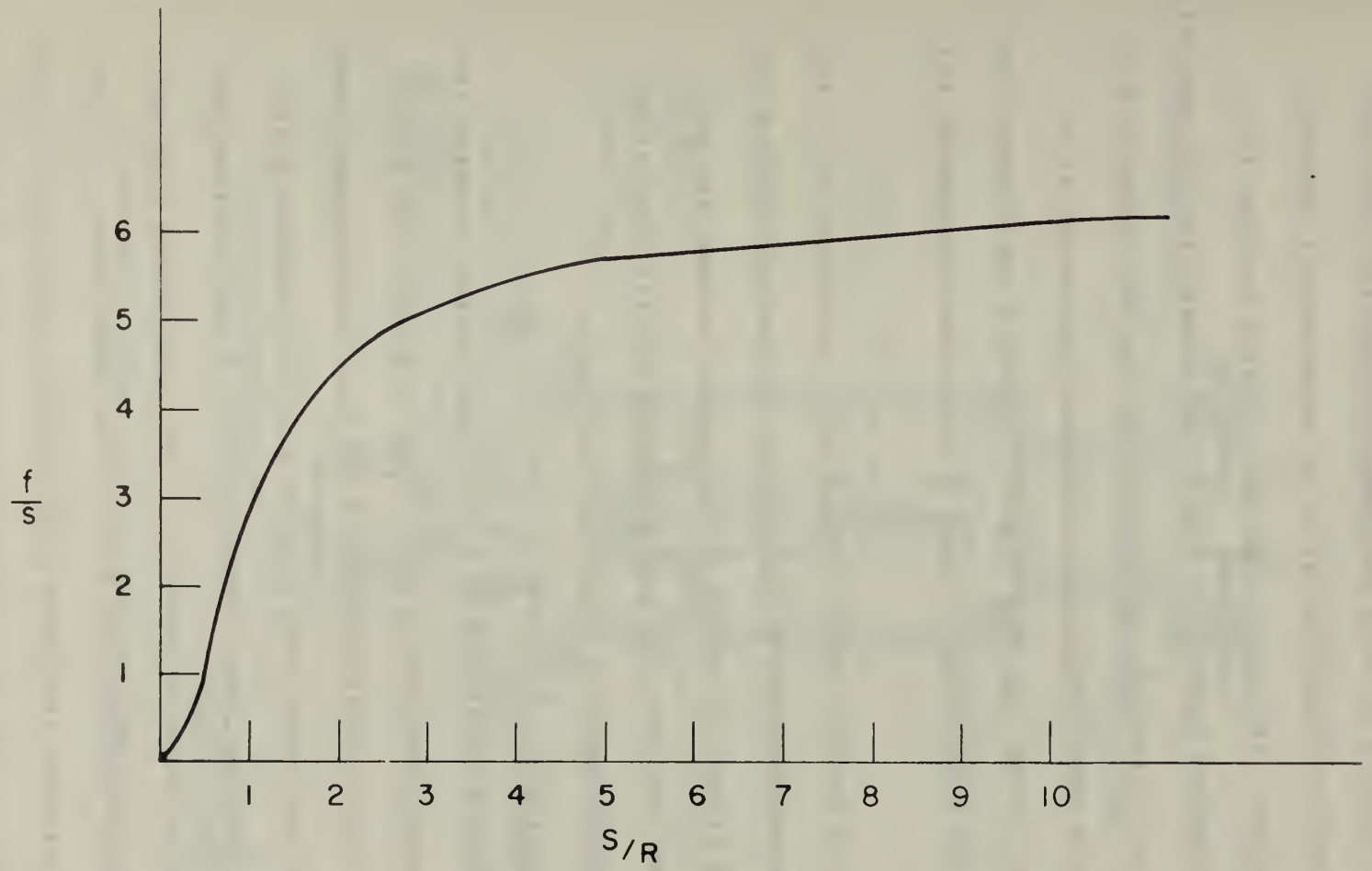


Figure A5-3. Einzel Lens Focal Length Relation.

APPENDIX VI

ELECTRON IMPACT ION SOURCE

At the beginning of this experiment it was realized that several ion sources compatible with the experimental apparatus would be required. Therefore some extra effort was put into building an electron impact ion source and determining its operating characteristics. Although the majority of the data presented in this thesis were obtained using a different ion source it is planned to use plasma type ion sources in future measurements and a summary of our developmental work is therefore included in this appendix.

In this ion source, shown schematically in Figure A6-1, the ions are produced by electron bombardment of the gas filling the source can. A plasma is formed in the region between the grid and the filament and the ions are extracted axially from it by the application of external electrostatic fields.

Physical Description

The ion source consisted of a 5.715 centimeter diameter inverted glass press (see Figure A6-1) made of number 3320 glass, with four, in line, equally spaced, 1/16 inch diameter pure tungsten rods. The two outer rods support a 15 mil tungsten wire helical grid. The two inner rods support a 15 mil tungsten wire filament. Both grid and filament are 4.81 centimeters long and 4.81 centimeters above the flat side of the glass press. In the original configuration the glass press became coated with a layer of tungsten after a very short period of operation. In order to

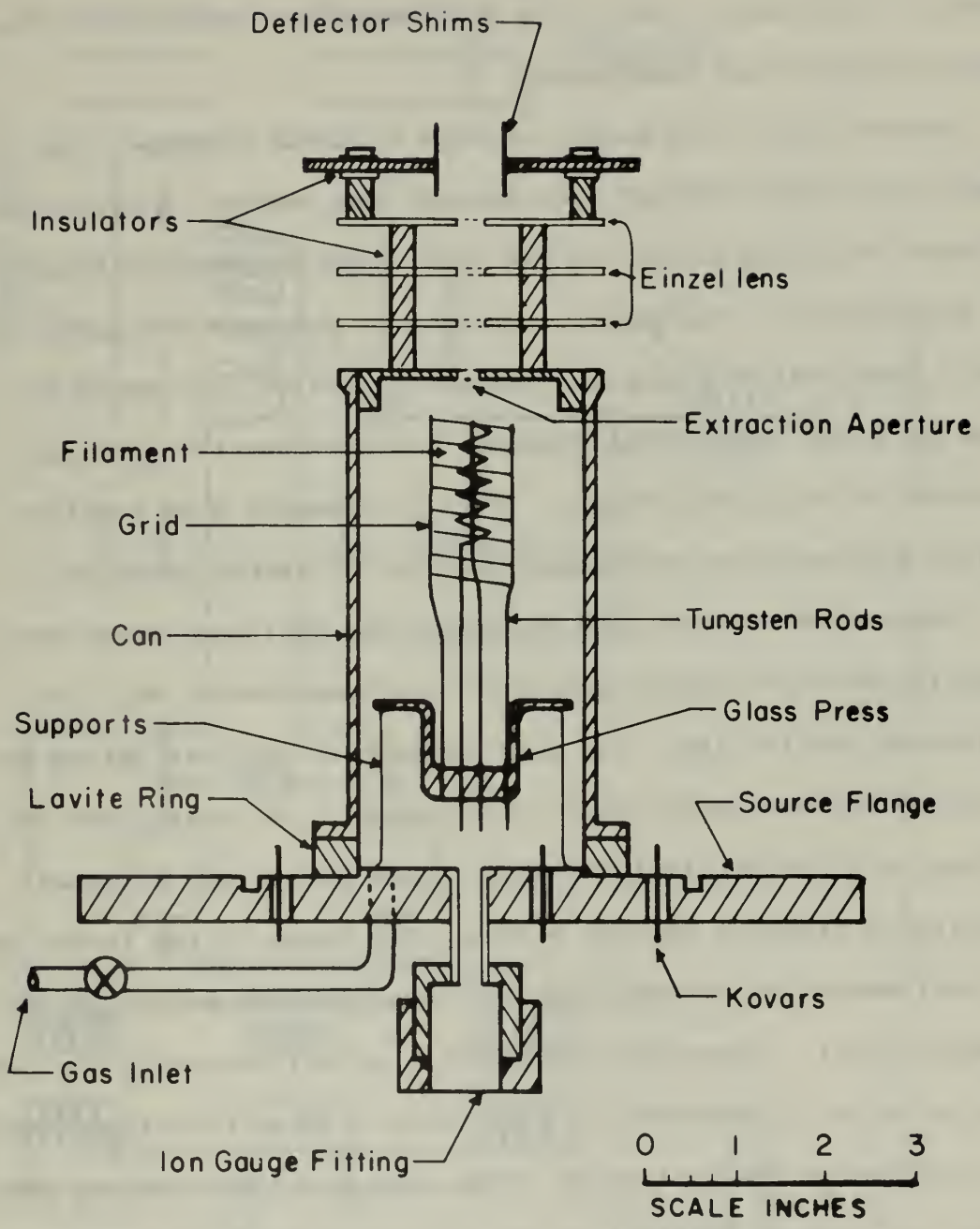


Figure A6-1. Schematic of Electron Impact Source.

prevent the filament and grid from shorting, the glass press was inverted, letting the tungsten support rods sit in the well as shown in the figure. With this arrangement no shorting of the source elements was experienced.

Source gases were passed through a liquid nitrogen trap to remove water vapor before they entered the source. A precision gas metering valve placed in the inlet pipe was used to regulate the gas flow into the source. The source pressure was measured with a Bayard-Alpert type ion gauge attached to the source by means of a 3/4 inch inside diameter "quick-connect" coupling attached to the source flange. This arrangement gave positive control and accurate measurement of the ion source pressure.

The source can was made of number 304 stainless steel and insulated from its base plate with a 1.27 centimeter by 1.27 centimeter lavite ring. The beam extraction hole was varied in size from 0.5 centimeter to 0.1 centimeter. An einzel lens consisting of three parallel stainless steel plates was attached directly in front of the ion source. The holes in the lenses were 1.4 centimeters in diameter and the lens elements were 1.27 centimeters apart. These lens dimensions, calculated using the lens formulas given in Appendix V, were found to give the highest beam currents inside the scattering cell. Two pairs of steering electrodes are mounted external to the outermost focusing lens to assist in beam alignment.

The ion source is wired as shown in Figure A6-2. The filament power is supplied through an isolation transformer which allowed the filament and the grid to float on top of the extraction

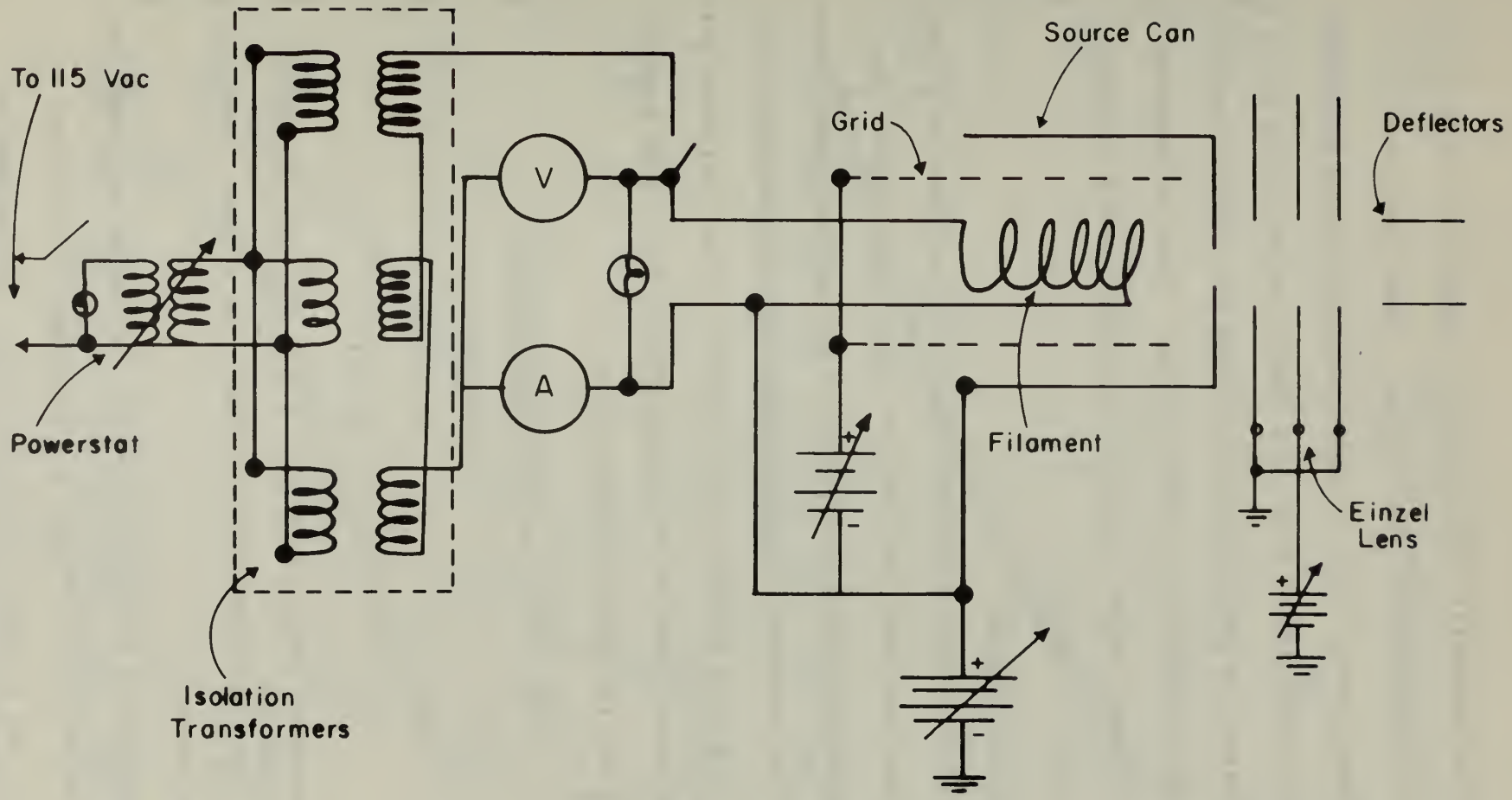


Figure A6-2. Electron Impact Ion Source Wiring Diagram.

electrode (can) potential. The highest potential is that of the grid and is the approximate beam energy. Energy analysis has shown the energy spread to be $\pm$ 4.0 eV about the grid potential, however other workers have found the energy spread to be $\pm$ 0.5 eV. A filament current of approximately 11 amps was found to produce adequate electron emission of about 100 ma. This corresponds to a measured filament temperature of about 3800^{o}K and a filament lifetime of over 100 hours.

Operating Characteristics

The grid-current/grid-voltage relationship, shown in Figure A6-3 for H_2 gas, are characteristic of these of all gases used. The source operating area corresponds to the grid voltages above the grid current plateau. Although there is some measurable ion beam with a zero grid voltage, there appears to be a minimum grid voltage below which there is no actual discharge. These minima were found to be, for the different gases,

GAS	MIN. GRID VOLTAGE
H_2	70 Volts
He	90 Volts
N_2	36 Volts

at a source pressure gauge reading of 3.0 x 10^{-3} Torr. Any increase above these voltages caused a small, 1% at most, decrease in total beam intensity.

The dependence of ion beam intensity on source gas pressure is shown in Figures A6-4 and A6-5 for hydrogen and nitrogen respectively. As can be seen from the figures, the maximum ion

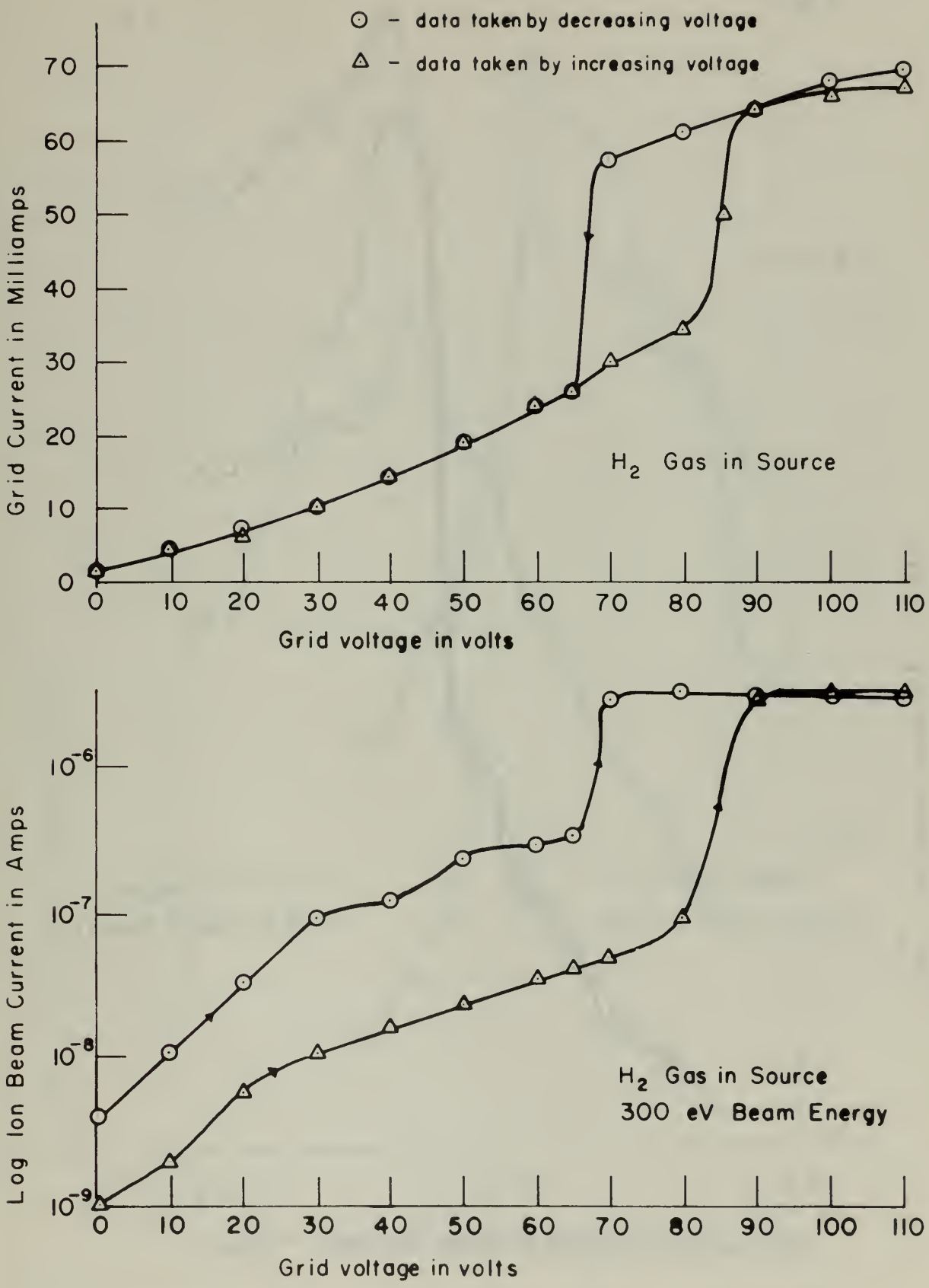


Figure A6-3. Electron Impact Source Characteristics.

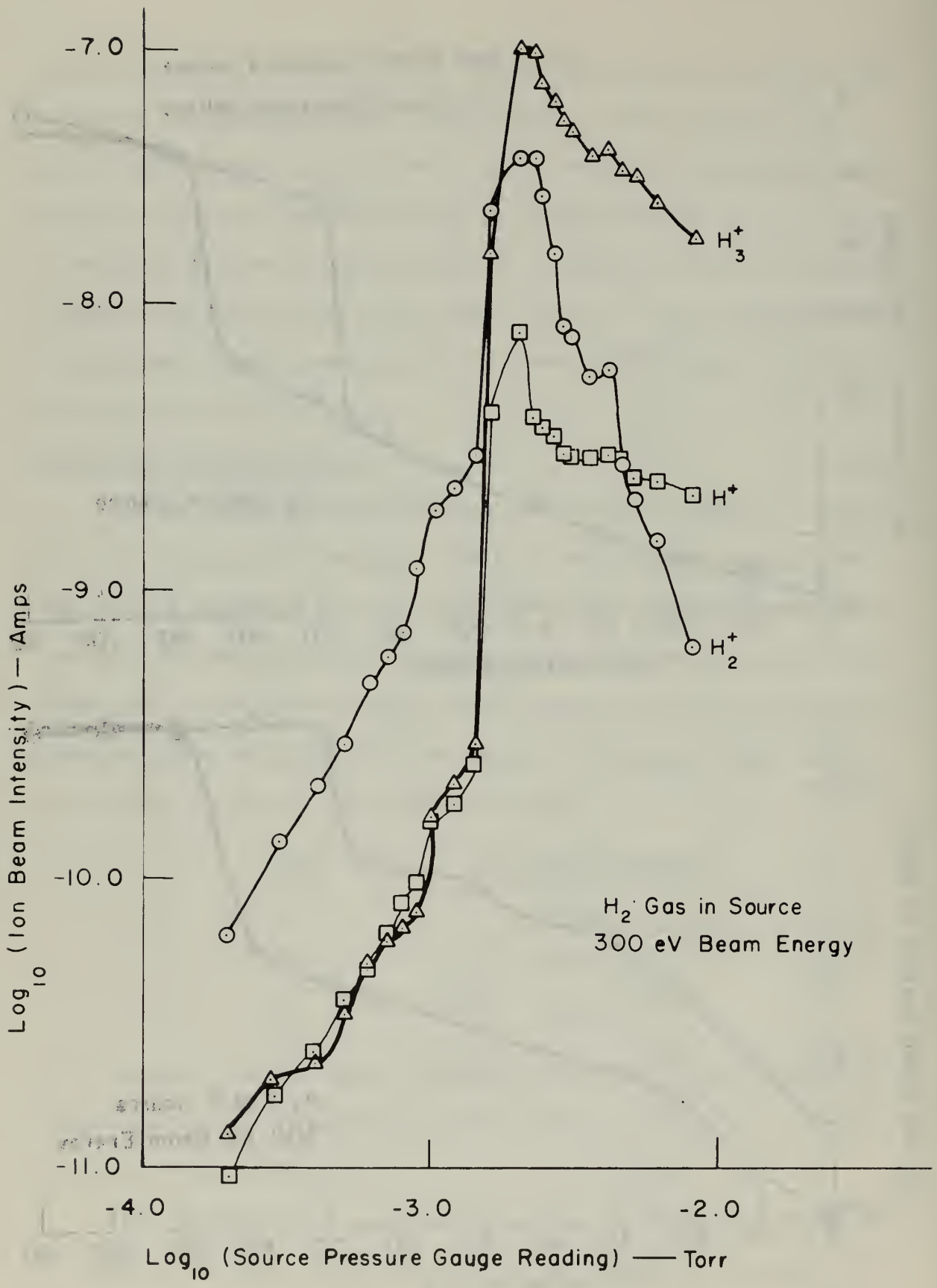


Figure A6-4. Ion Output vs Source Pressure for H_2 Source Gas.

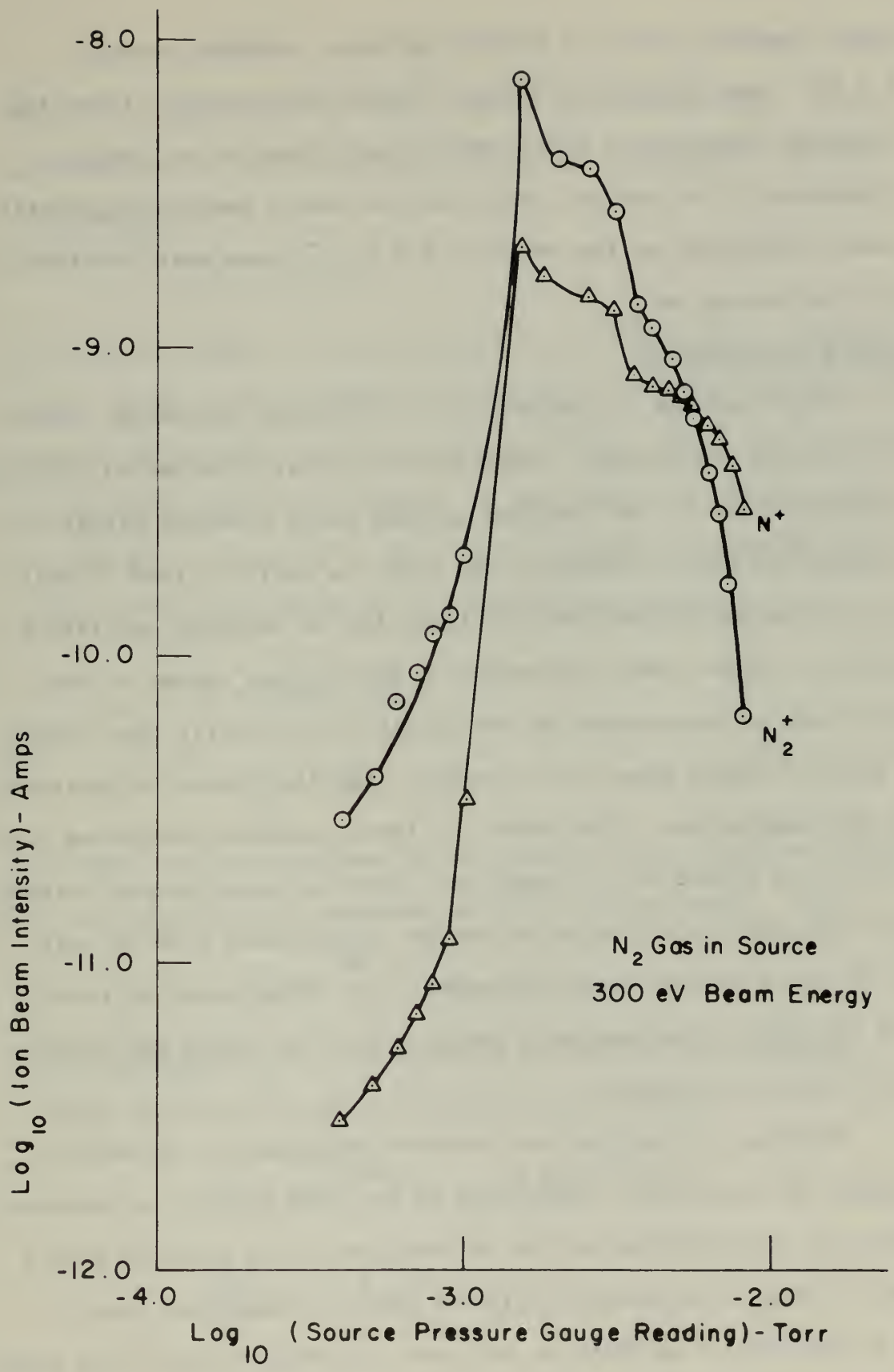


Figure A6-5. Ion Output vs Source Pressure for N_2 Source Gas.

beam intensity occurs at source ion gauge readings between 2×10^{-3} Torr and 3×10^{-3} Torr. Below this pressure range the ion beam intensity is quite small since there was no longer a discharge in the source. With the ion source operating properly, beam intensities on the order of 3.0×10^{-8} amps were obtained in the scattering cell.

Theory of Operation

The discharge in the source is a Townsend discharge, which is non-self-sustaining. There are two primary sources of ionizing electrons: one is the tungsten cathode which produces electrons through thermionic emission, the other is neutral atoms or molecules from which electrons are liberated in ionizing collisions. However, before these "secondary" electrons can ionize in turn they must be accelerated by the electric field until they obtain a kinetic energy equal to or greater than the ionization potential of the neutral gas. The effect of these secondary electrons can be seen in Figure A6-3. There the large increase in grid current and beam current as the grid voltage is increased from 60 volts to 90 volts is explained by the fact that above about 60 volts the secondary electrons have enough energy to ionize the neutral gas through collisions.

The beam current is also pressure dependent as is seen in Figures A6-4 and A6-5. This peak in the beam current vs pressure curve can be explained in the following way. An electron with a small energy in an electric field $\vec{E}$ begins a mean free path, L. To be capable of ionizing at its next collision it must gain energy from the electric field after traveling a distance d such that

$$qdE \geq q \quad \text{or} \quad d \geq \frac{V}{E}$$

where V is the ionization potential of the neutral gas. The probability that the electron will travel a distance d without a collision is

$$P(d) = e^{-d/L} .$$

This is the number of ions produced by an electron in a mean free path. Since 1 cm of actual path contains 1/L mean free "ionizing" paths, the probability of a free path longer than L per cm of path in the field direction is equal to the number of ionizing collisions per cm of path in the field direction. Therefore the number of ions produced by an electron per centimeter is

$$\alpha = P(d)/L = \frac{1}{L} e^{-d/L}$$

or

$$\alpha = \frac{1}{L} e^{-\frac{V}{EL}} .$$

The mean free path depends on the pressure and can be written as $\frac{1}{L} = Ap$, where A is a constant and p is the pressure. Then

$$\alpha = p^{Ae^{-\frac{B}{Ep}}} , \text{ where } B = AV.$$

From this expression, the pressure at which α is a maximum, making the beam current a maximum, can be found.

$$d\alpha = A\, e^{-B/Ep}\, dp - p\, A \frac{B}{E} e^{-B/Ep}\, dp$$

$$\frac{d\alpha}{dp} = \left(1 - \frac{B}{E} p\right) .$$

At maximum $\frac{d\alpha}{dp} = 0$ making $(1 - B/E\ p_m) = 0$.

Thus $p_m = E/B$

is the pressure at which maximum beam current (ion formation) occurs. Notice that this depends on the gas, its ionizing potential, and the electric field the electron is in. This demonstrates that there should be a maximum in the pressure vs beam current data. However, our approach has been too simplified to allow us to calculate p_m from tabulated values of B. For example ionization by photons emitted from the tungsten filament has been ignored. However, from the simple model it is seen that in order to obtain the most intense beams, the source should be operated at or a little above p_m and with a grid voltage at or above that required to produce ionizing secondary ions.

Proton Production

Since a high intensity proton beam is desirable for the study of some of the proposed reactions an attempt was made to enhance the proton output of the electron impact ion source by introducing water vapor into the discharge as was suggested by Dawson and Tickner[25]. The set of reactions

$$H_3^+ + H_2O \longrightarrow H_3O^+ + H_2$$

$$H_3O^+ + e^- \longrightarrow H_2O + H$$

if actually occuring, would enhance the amount of atomic hydrogen and hence the proton output while reducing the H_3^+ output. It was found that the proton output was increased with a corresponding reduction in the H_2^+ and H_3^+ outputs as water vapor was added to the discharge. However the total H^+ beam intensity itself decreased by a factor of 100. It was also found that significant changes in the ratio of H^+ to H_2^+ and H_3^+ yields occured only after the discharge was 20% to 40% water vapor. It was felt that this was an unacceptable load on the vacuum pumps and this approach was therefore not pursued further.

Initial Distribution List

		No. Copies
1.	Defense Documentation Center Cameron Station Alexandria, Virginia 22314	20
2.	Library Naval Postgraduate School Monterey, California 93940	2
3.	Defense Atomic Support Agency Department of Defense Washington, D.C. 20305	1
4.	Dr. Otto Heinz Department of Physics Naval Postgraduate School Monterey, California 93940	5
5.	LT Thomas O. Bush, USN 1017 Laguna Livermore, California 94550	3
6.	Dr. Charles J. Cook Stanford Research Institute (A220) Menlo Park, California 94025	1
7.	Dr. Charles A. Blank DASA Headquarters Washington, D.C. 20305	1

DOCUMENT CONTROL DATA - R & D

(Security classification of title, body of abstract and indexing annotation must be entered when the overall report is classified)

1. ORIGINATING ACTIVITY *(Corporate author)*
Naval Postgraduate School
Monterey, California 93940

2a. REPORT SECURITY CLASSIFICATION
UNCLASSIFIED

2b. GROUP

3. REPORT TITLE
Large Angle Scattering of Lithium Ions by Helium Atoms

4. DESCRIPTIVE NOTES *(Type of report and inclusive dates)*
Thesis, Ph.D., September 1968

5. AUTHOR(S) *(First name, middle initial, last name)*
Bush, Thomas O., LT, USN

6. REPORT DATE	7a. TOTAL NO. OF PAGES	7b. NO. OF REFS
September 1968	152	25

8a. CONTRACT OR GRANT NO.
NA

b. PROJECT NO.

c.

d.

9a. ORIGINATOR'S REPORT NUMBER(S)
NA

9b. OTHER REPORT NO(S) *(Any other numbers that may be assigned this report)*
NA

This document has been approved for public release and sale; its distribution is unlimited.

10. DISTRIBUTION STATEMENT
This document is subject to special export controls and each transmittal to foreign nations may be made only with prior approval of the Superintendent, Naval Postgraduate School, Monterey, California 93940.
Nov 9/14/71

11. SUPPLEMENTARY NOTES
NA

12. SPONSORING MILITARY ACTIVITY
Naval Postgraduate School

13. ABSTRACT

An experiment using the focusing properties of a nonuniform axially symmetric magnetic field to study large angle ($\theta > 32^{o}$) scattering of ions from atoms and molecules is described. The scattering cell is placed on the magnetic field axis and all ions in the momentum interval $|\Delta p|$ at $|p|$ scattered into a conical shell $\Delta\theta$ at θ are counted by a detector placed further down the axis. The solid angle is increased by a factor of several hundred over conventional scattering techniques of comparable angular resolution. The magnetic vector potential and the trajectory equation for a charged particle in the field are derived. The computer program which solves the trajectory equation is given along with a detailed description of the apparatus. Our measurements of the absolute differential scattering cross sections for Li^{+} on He from 36^{o} to 41.7^{o} at 200 eV and 300 eV and for He^{+} on He from 40^{o} to 54^{o} at 300 eV and 400 eV demonstrate the feasibility of the technique. Using the measured cross sections for Li^{+} on He and the computational method of Firsov we have calculated the interatomic potential function for nuclear separations of 0.15Å to 1.1Å.

DD FORM 1 NOV 65 1473 (PAGE 1)
S/N 0101-807-6811

UNCLASSIFIED
Security Classification

A-31408

14 KEY WORDS	LINK A		LINK B		LINK C	
	ROLE	WT	ROLE	WT	ROLE	WT
Differential Scattering Cross Section Measurement						
Lithium Ions on Helium Atoms						
Helium Ions on Helium Atoms						
Interatomic Potential Calculation						
Nonuniform Magnetic Field						
Ion Trajectories						
Magnetic Potential						
Magnetic Electron Multiplier						

Gaylord
PAMPHLET BINDER
Syracuse, N. Y.
Stockton, Calif.

thesB922
Large angle scattering of lithium ions b
3 2768 002 08832 0
DUDLEY KNOX LIBRARY